工學博士學位論文

Morphological and chemical modification of polyacrylonitrile-derived porous carbon nanoweb layers for gas sensor applications

폴리아크릴로니트릴 기반 다공성 탄소 나노그물막의

형태적/화학적 개질 및 가스 센서로의 응용

2020年 2月

서울大學校 大學院

化學生物工學部

羅 元 柱

Morphological and chemical modification of polyacrylonitrile-derived porous carbon nanoweb layers for gas sensor applications

폴리아크릴로니트릴 기반 다공성 탄소 나노그물막의 형태적/화학적 개질 및 가스 센서로의 응용

指導教授 張 正 植

이 論文을 工學博士 學位論文으로 提出함

2019 年 11 月

서울大學校 大學院

化學生物工學部

羅 元 柱

羅元柱의 工學博士 學位論文을 認准함

2019 年 11 月

委 員 長 _____ (印)

副委員長 _____ (印)

委　　員 _____ (印)

委　　員 _____ (印)

委　　員 _____ (印)

Morphological and chemical modification of polyacrylonitrile-derived porous carbon nanoweb layers for gas sensor applications

by

Wonjoo Na

Submitted to the Graduate School of Seoul National University
in Partial Fulfillment of the Requirements
for the Degree of Doctor of Philosophy

February, 2020

Thesis Adviser: Jyongsik Jang

Abstract

Sensors are becoming very important in internet of things (IoT) era because they are closely related to real life. Among them, high-performance gas sensors are demanded for medical diagnosis, health care system, environmental monitoring, grocery quality management, and industrial safety from combustible, explosive, harmful, and toxic gases. The performance of gas sensors depends on the sensing ability of transducers. The transducer is one of the sensor device components of detecting analyte and converting detection to electrical signal. To improve the sensing ability of transducers, nanomaterials are widely studied for enhancing specific surface area. Among the nanomaterials, carbon based nanomaterials, especially derived from polyacrylonitrile (PAN), are the most generally and widely used for sensor transducer due to their outstanding chemical, electrical, and mechanical properties, such as biocompatibility, easy to handling, environmental stability, and high electrical conductivity. Although downsizing the carbon nanomaterials is representative way to increase the specific surface area, surface modification is also one of the efficient methods to enhancing the sensing ability of active material.

This doctoral dissertation discusses the effective strategies for morphological and chemical modification of PAN-derived carbon nanolayers and suggests them as sensor transducer for gas detection. Firstly, surface morphology control of porous carbon nanoweb layers (PCNWLs) proceeded by adjusting the PAN and polystyrene (PS) mixing ratio, following sequential heat treatment. The resulting PCNWLs exhibited high specific surface area compared with bare PAN-derived carbon layer, demonstrating highly sensitive gas sensor for ethanol detection. Secondly, fluorination, heteroatom doping of fluorine, progressed on the PCNWLs *via* vacuum plasma treatment with different plasma treating time. The resulting fluorinated PCNWLs (FPCNWLs) were applied to highly sensitive ammonia gas sensor. Finally, noble metal introduction was advanced with electrochemical deposition of platinum, constructing Pt villus structure on the PCNWLs varying biased voltage and concentration of Pt precursor. The following Pt villus overlaid PCNWLs (PtPCNWLs) were demonstrated as hydrogen gas sensor with high performance.

Consequently, this study provides the facile morphological and chemical modification methods of PAN-derived carbon layer for increasing specific surface area, for enhancing chemical, mechanical,

and electrical properties, and for sensing ability. Furthermore, highly sensitive gas sensor application approaches are provided with the adduced PCNWLs, FPCNWLs, and PtPCNWLs as sensor transducers. This dissertation suggests innovative methodological insights of modifying carbon nanomaterials and constructing gas sensor system.

Keywords: morphological modification; chemical modification; shape morphology control; heteroatom doping; fluorination; metal introduction; noble metal; platinum; electrochemical deposition; carbon nanoweb layer; gas sensor; ethanol; ammonia; hydrogen

Student Number: 2015-21017

List of Abbreviations

2D: two-dimensional

A: ampere

AFM: atomic force microscope

Ag: silver

AgCl: silver chloride

ATR: attenuated total reflection

Au: gold

B: boron

BET: Brunauer–Emmett–Teller

C: carbon

C_2F_6: hexafluoroethane

C_4F_8: octafluorocyclobutane

$C_6H_5CF_3$: trifluorotoluene

ca.: circa (about)

CF_4: tetrafluoromethane

CF_x: fluoromethane

cm: centimeter

CNT: carbon nanotube

CO: carbon monoxide

DI: deionized

dI: derivatives of current

DMF: N,N-dimethylformamide

DMSO: dimethyl sulfoxide

dV: derivatives of voltage

EDS: energy dispersive X-ray spectroscopy

eV: electron volt

F: Fluorine

fcc: face-centered-cubic

FE-SEM: field emission scanning electron microscope

FPCNWL: fluorinated porous carbon nanoweb layer

FT-IR: Fourier transform infrared spectroscopy

g: gram

h: hour

H: hydrogen

H_2: hydrogen gas

H_2O: water

H_2O_2: hydrogen peroxide

H_2SO_4: sulfuric acid

HF: hydrofluoric acid

$I{-}V$: current–voltage

i.e.: Id Est (for example)

I_D: intensity of defects

I_G: intensity of graphitics

IoT: internet of things

k: kilo

L mol^{-1} cm^{-1}: liters per mole centimeter

LED: light-emitting diode

M: mole per liter

m^2 g^{-1} : square meters per gram

MB: methylene blue

MDL: minimum detection level

MeCN: acrylonitrile

mg L^{-1}: milligrams per liter

min: minute

MIP: mercury injection porosimetry

ml: milliliter

mM: millimole per liter

M_w: molecular weight

n-type: negative type

N: nitrogen

N_2: nitrogen gas

NH_3: ammonia gas

nm: nanometer

NO_x: nitrogen oxide

O: oxygen

OFET: organic field effect transistor

OM: optical microscope

OSC: organic solar cell

PAN: polyacrylonitrile

PCNWL: porous carbon nanoweb layer

Pd: palladium

ppb: parts per billion

ppm: parts per million

PS: polystyrene

Pt: platinum

$PtCl_4$: platinum (IV) chloride

PtH_x: platinum hydride

PtPCNWL: platinum villus overlaid porous carbon nanoweb layer

RF: radio frequency

RMS: root-mean-square

rpm: revolution per minute

$S\ cm^{-1}$: siemens per centimeter

s: second

S: sulfur

sccm: standard cubic centimeters per minute

SF_6: sulfur hexafluoride

Si: silicon

SiO_2: silicon dioxide

TGA: thermogravimetric analysis

UV-vis: ultraviolet-visible

V: voltage

VOC: volatile organic compound

W: watt

XPS: X-ray photoelectron spectroscopy

XRD: X-ray diffraction

℃: celsius degree

$℃\ cm^{-1}$: Celsius degrees per centimeter

−: minus

%: percentage

θ: theta

μm: micrometer

List of Figures

min (FPCNWL20).

List of Tables

Table of Contents

1. Introduction

1.1. Background

1.1.1. Carbon nanomaterials

Carbon atoms have curious covalent bonds, both σ and π, with adjacent other carbon atoms forming sp, sp^2, and sp^3 bonds [1–3]. This aspect provides various carbon allotropic structures in nanoscale, called carbon nanomaterials (**Figure 1**). Nowadays, the carbon nanomaterials have been studied interestly due to their diverse and excellent properties. They have biocompatibility, large specific surface area, and outstanding thermal, optical, physical, chemical, electrical, and mechanical properties in electrochemical environments [4–9]. For this reason, the carbon nanomaterials have been used numerous applications in semi-conductor, energy storage, display, biomedical technologies, automobile, aerospace, and sensor electrodes because they are easily tunable their various properties [10–19].
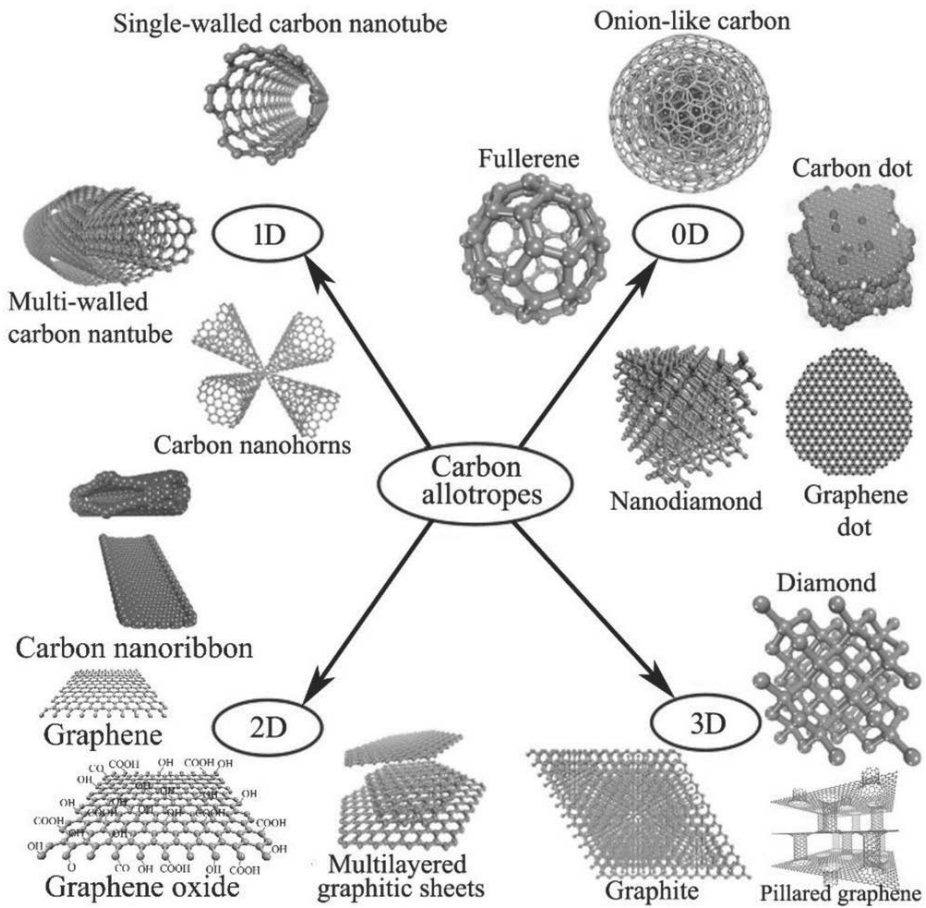
Figure 1. Various carbon nanostructures in different dimensions [20].

1.1.1.1. Carbon thin layer

Carbon thin layer, also called carbon thin film, is widely researched in several decades for substitution of metal electrode. Compared to conducting polymers, due to their flexible and superb stability, carbon thin layer is used at flexible organic electrode. Representatively, carbon nanotube (CNT) and graphene have been reported for the flexible organic electrode, such as organic field effect transistors (OFETs), light-emitting diodes (LEDs), organic solar cells (OSCs), and chemical sensors (**Figure 2**). However, they have several disadvantages including irregular dispersibility, complicated and expensive fabrication processes to popularize the methods in real industry [21–26].

As an alternative, fabrication of carbon thin films from the pyrolyzation and carbonization of polymers is in the spotlight again. One of the advantages of this manufacturing method is that it is a solution process. Coating the polymer solution on the substrate, the properties are easily modified several treatments.

1.1.1.1.1. Spin coating method

Spin coating is a typical procedure used for application of uniform thin film on flat substrates. The process involves depositing a small drop of polymeric solution, ionic solution, or resin onto the center of a substrate and spinning the substrate at high speed forming thin film. The final film thickness and several film properties are depended on the viscosity, drying rate, surface tension, and spin-coating parameters.

The spin coating process is divided into four steps as follows: dispense stage, acceleration stage, fluid thinning stage, and solvent evaporation stage. Among those steps, especially at the dispense stage, there are two common methods of dispense that are static and dynamic dispense. Static dispense is simply depositing a small amount of solution or resin on the center of the substrate. The amount of them depends on their viscosity to cover the entire substrate during the high-speed spin step. On the other hand, dynamic dispense is the process of dispensing the solution or resin onto the substrate when it is spinning at low speed. The dynamic dispense method requires less amount of fluid materials and advantages in using poor wettability substrate [27–30].
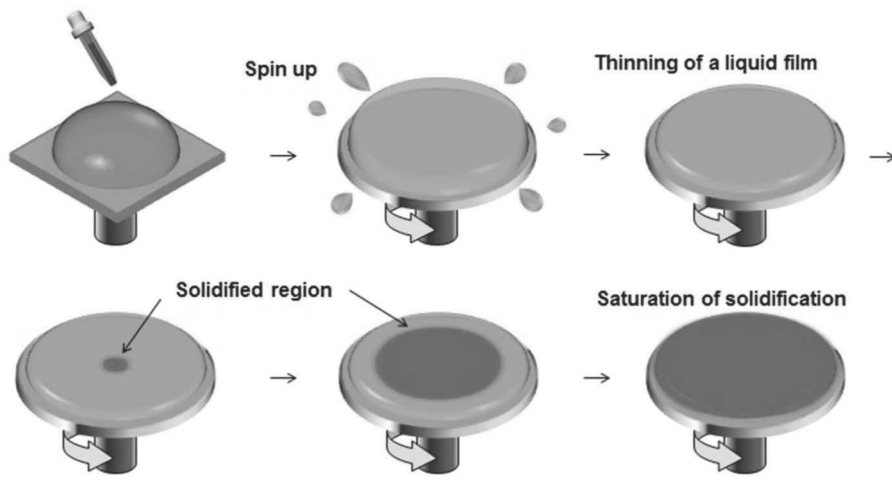
Figure 2. Schematic diagram of organic thin film deposition mechanism
by spin-coating methods [30].

1.1.1.2. Polyacrylonitrile (PAN)

Polyacrylonitrile (PAN) is semi-crystalline thermoplastic polymer with remarkable properties, such as it rigidity, chemical stability, carbon-rich, low cost, and deformability to multidimensional structure, therefore, generally used as carbon source precursor for carbon nanomaterials (**Figure 3**). The crystallinity of PAN is driven by the high dipole moment of nitrile groups. These interactions induce helical chain conformation and hexagonal chain arrangement for PAN. Moreover, PAN is only soluble in polar organic solvents, such as dimethyl sulfoxide (DMSO), *N,N*-dimethylformamide (DMF), and acrylonitrile (MeCN), due to their strong interactions between nitrile groups [31–34].

In order to convert PAN structure to carbon structure, two steps of thermal treatments, which are oxidative stabilization and carbonization should proceed because PAN has low melting point at 300 ℃ causing low carbon yields (**Figure 4**). At the stabilization step, especially, there are several reactions, containing cyclization, crosslinking, dehydrogenation, oxidation, and aromatization. Generally, stabilization process of PAN progresses at the temperature between 200 and 300 ℃ in air to forming a ladder structure. During the procedure, the free radicals are produced by extraction of hydrogen from carbon structure

near the nitrile group. These carbon radicals are in equilibrium with a structure with the odd electron in the nitrile group of the same chain, following formation of the crosslinked ladder structure with multiplication of the cycling containing C=N bond. Whereas, oxygen is not directly implicated in the cyclization but encourages the dehydrogenation of carbon chains, crosslinking, and aromatization. At the carbonization step, compressed aromatic rings are formed through the condensation of ladder structures, then nitrogen doped carbon structure is constructed [35–38].
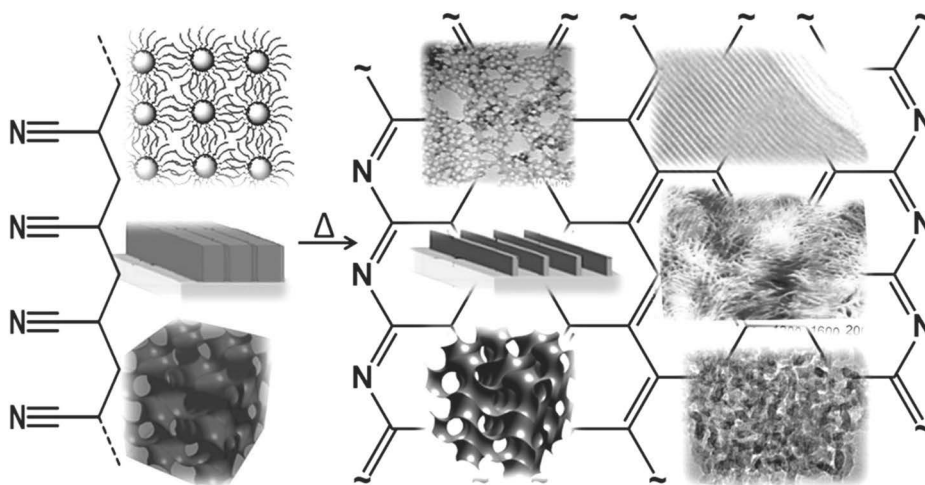
Figure 3. An overview on PAN-derived carbon nanomaterials [32].
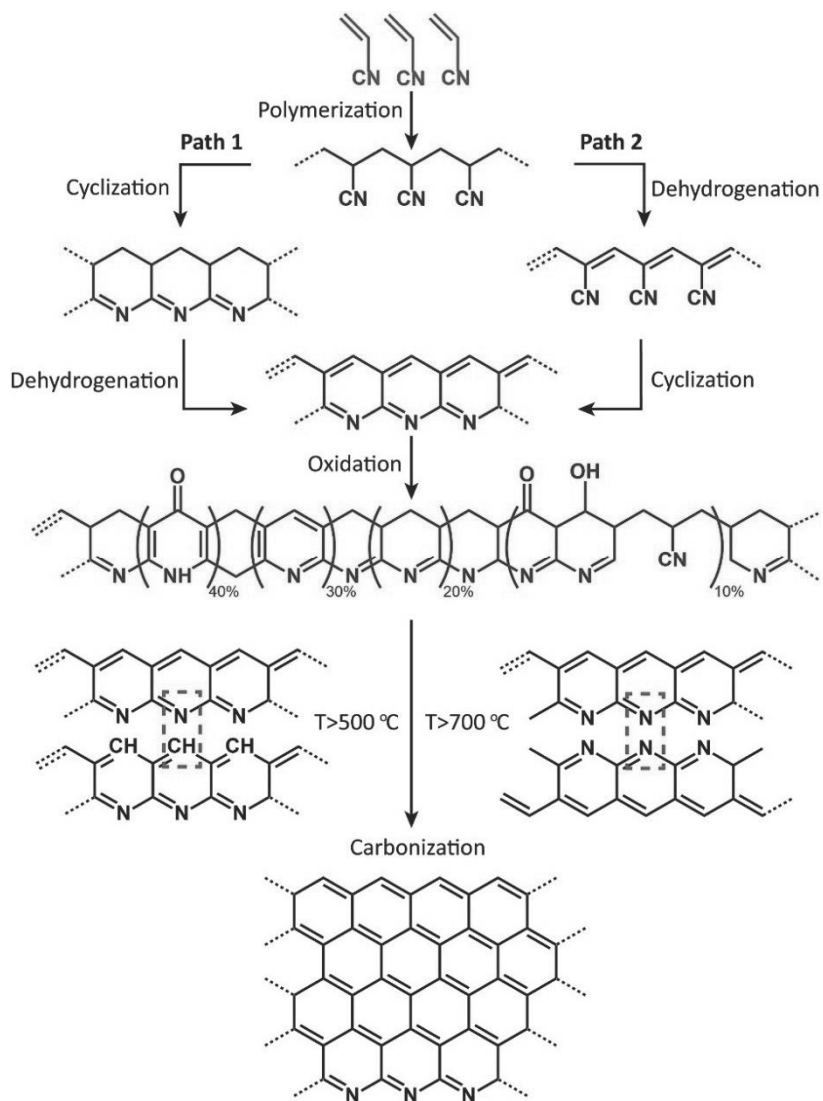
Figure 4. Various reactions during the oxidative stabilization and carbonization of PAN. Free radicals occurring at low temperature initiate the oxidative reactions for the cyclization of the nitrile chains in PAN, and intermolecular condensation of the ladder-like structures results in the graphitic structures [37].

1.1.2. Surface modification

1.1.2.1. Shape morphology control

The most representative way to modify the surface of carbon materials is controlling shape morphology. Typically, in nanomaterial research, shape morphology modification refers to constructing unique structure to increase specific surface area and diminishing the size distribution [39–40].

To improve the specific surface area, building porosity is one of the most effective method. Depending on the size of the pores formed, the pores are classified into micropore, mesopore, and macropore, as the pore diameter is less than 2 nm, between 2 and 50 nm, and greater than 50 nm, respectively [41–44]. There are several porosity measuring methods, such as direct measurement, imbibition method, mercury injection porosimetry (MIP), N_2 gas adsorption method with Brunauer–Emmett–Teller (BET) calculation, dye adsorption method, petrographic methods, and liquid displacement method (**Figure 5**).
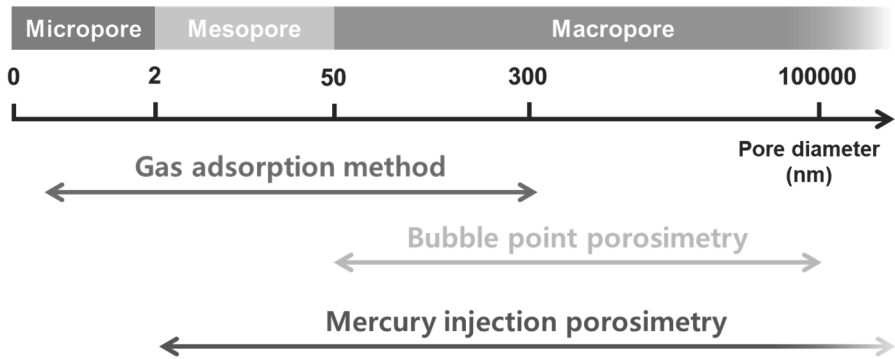
Figure 5. IUPAC classifications of pores based on the pore width and various porosity measurements depending on the pore sizes.

1.1.2.2. Heteroatom doping

Heteroatom doping is the method of exchanging carbon atoms with heteroatoms (like B, N, O, F, P, and S) to tuning electronic structure of carbon nanomaterials. There are various method of heteroatom doping process containing plasma treatment, hydrothermal treatment, pyrolysis with elemental precursors, and chemical vapor deposition [45–47].

The doping process redistributes the charge and spin density of carbon atoms due to different dipole moment depending on different electronegativity and atomic size of carbon and heteroatoms (**Figure 6**). Moreover, heteroatoms act as electron donors and acceptors in the carbon lattice optimizing valence orbital energy for carbon structure and increasing intrinsic activity. This effect causes adjusting the work function and improving the adsorptivity of analytes of transducer [20, 48–52].
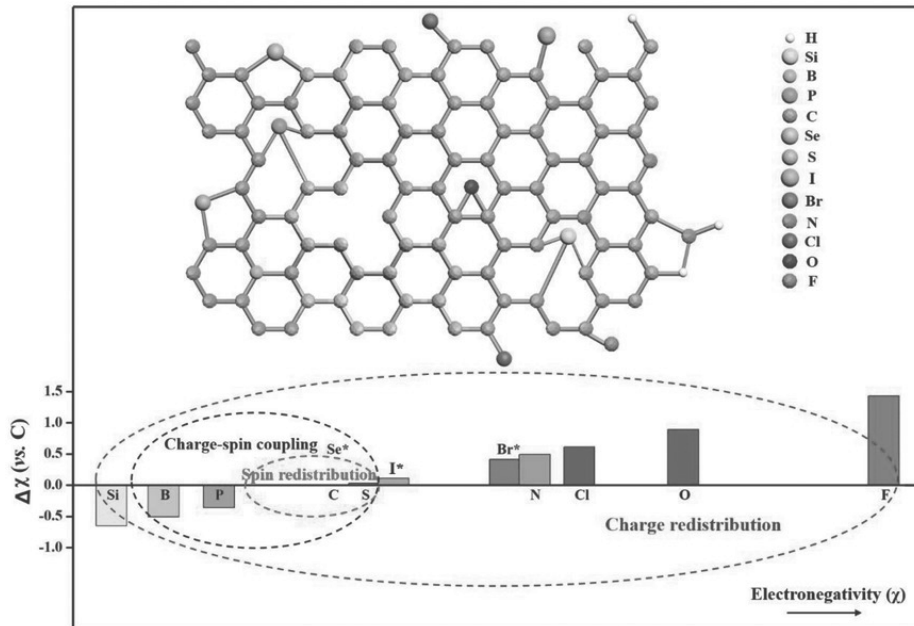
Figure 6. Schematic illustrations on heteroatom doped carbon materials. Upper part: structural diagram of carbon lattice doped with different heteroatoms. Lower part: classification on the origin of doping effects as charge redistribution, spin redistribution, and charge–spin coupling based on the relative electronegativity of heteroatom dopants [49].

1.1.2.2.1. Fluorine doping

Fluorine is the lightest halogen element that is extremely reactive due to its high electronegativity. Fluorine doping, fluorination, induces p-type doping because fluorine atom is strong p-type dopant that extracting electrons from the valence band of the carbon electrode as well as increasing holes in transducer due to their high electronegativity. Additionaly, the fluorine doping causes reduced surface energy and internal stress, enhanced biocompatibility and hydrophobic propertiy, and superior diminished friction coefficient [53–56].

To dope fluorine to carbon lattice, various fluorine precursors are used depending on the doping operation. For chemical doping, hydrofluoric acid (HF) and trifluorotoluene ($C_6H_5CF_3$) are used, whereas, sulfur hexafluoride (SF_6), octafluorocyclobutane (C_4F_8), tetrafluoromethane (CF_4), and hexafluoroethane (C_2F_6) gases are used for plasma doping or deposition as fluoric sources. Each chemicals is broken into F^+ or CF_x ions or C–CF_x molecules, then, replaced or attached on the defects in carbon lattice of active materials [57–59].

1.1.2.2.2. Vacuum plasma treatment

Heterogeneous elements are readily doped into carbon lattice using plasma treatment (**Figure 7**). During plasma doping, the accelerated ions are extracted from the plasma by applying power supply and targeting them into active materials. The plasma equipments are classified into its treating condition as vacuum plasma and atmospheric plasma. The atmospheric plasma can easily modify the functional groups on the material without complicated procedure. However, air can be act as pollutant and interference, therefore, exquisite work is impossible and oxygen is the primary source of plasma. On the other hand, in vacuum chamber, the plasma source can be high ion density and low contamination level, which can be able to handle more elaborate modification and use various doping sources than atmospheric condition. Vacuum plasma treatment can also operate with high dose rate of dopant and with large target area [60–63].
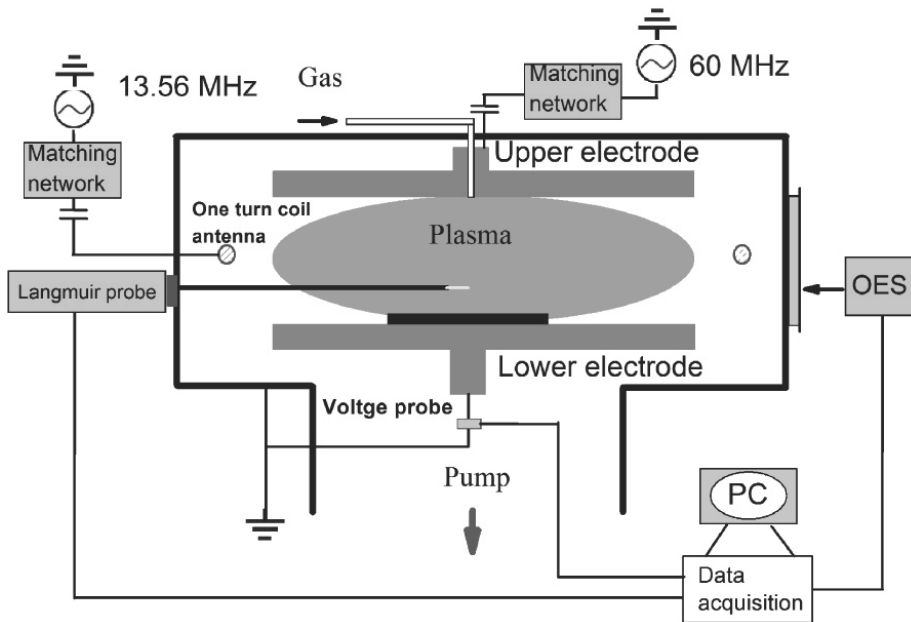
Figure 7. Schematic diagram of the RF vacuum plasma apparatus [64].

1.1.2.3. Metal introduction

1.1.2.3.1. Noble metal

Noble metals such as gold (Au), silver (Ag), palladium (Pd), and platinum (Pt) have been attracted tremendous attention for their outstanding properties of catalytic, electrical, physical, chemical, and optical characteristic in diverse applications. Among the noble metals, Pt is invaluable role in many research and industrial sites, such as CO/NO_x oxidation converter, hydrogen oxidation and oxyhen reduction in fuel cells, petroleum cracking, and catalyst in organic reactions. Moreover, Pt has also well-kown for detection ability of hydrogen gas [65–66].

Generally, there are two representative strategies to prepare the noble metal nanomaterials: top-down and bottom-up method. The bottom-up approach is based on reduction of metal ions and constructing structures, including chemical, electrochemical, photochemical, and thermal reduction. Meanwhile, top-down approach is based on lithography accompanied with etching materials from the bult substrate, including photolithography and E-beam lithography [67–69].

1.1.2.3.2. Noble metal/Carbon hybrid nanomaterials

Metal introduction to carbon nanomaterials is fabrication of composite nanomaterials investing metallic properties to carbon nanomaterials. Normally, carbon nanomaterials have excellent biocompatibility, durability, chemical, and optical properties, whereas, they have relatively poor electrical and mechanical properties compared to metals. Therefore, hybridization of metallic materials with carbon materials provides complementary properties breaking through improving entire qualities and solving technical problems of transducer materials [70–75].

Noble metal/carbon nanocomposites are mainly designed for offering catalytic properties to carbon nanomaterials and increasing specific surface area. Commonly, there are two synthetic approaches for introducing noble metals to carbon nanomaterials: *in-situ* and *ex-situ* methods. The *ex-situ* method is that preformed noble metal nanomaterials are dispersed and attached onto the carbon nanomaterials. The *in-situ* method, on the other hand, is that noble metal nanostructures are constructed on the carbon nanomaterials by reduction of noble metal precursor which is dissolved in the solution [76–77].

1.1.2.3.3. Electrochemical deposition

Electrochemical deposition is a typical technology of introducing materials or polymerization by applying a voltage through electrochemical cell. This technique is superior to other synthesis methods due to low energy consuming, few additives requirement, and absence of interference or byproducts during the process. In addition, the procedure can be operated at room temperature with aqueous/organic-based electrolytes for diverse scales [78].

General experimental settings for the electrochemical deposition incorporate a counter electrode, reference electrode, working electrode (where desired nanomaterials are deposited onto), electrolyte, and power supply. Moreover, various electrochemical techniques are used comprising potentiostatic (constant potential), galvanostatic (constant current), and potentiodynamic (potential scanning) methods [79].

For electrochemical deposition of metal nanomaterials, there are two kinds of processes, typically: electrophoretic deposition and electrolytic deposition. In the electrophoretic deposition, metal nanoparticles preformed with stabilizers are suspended in the solvent. Then, the charged nanoparticles are deposited onto the electrode under electric field. On the other hand, electrolytic deposition begins from metal ions

in the solution and the metal ions are reduced as the process progresses. Most of the electrochemical deposition of metal nanomaterials occurs at the cathode surface as the adsorbed metal ions are reduced (**Figure 8**). The metallic deposition kinetics and compositions are affected by potential, current density, solvents, additives, and temperature [80–83].
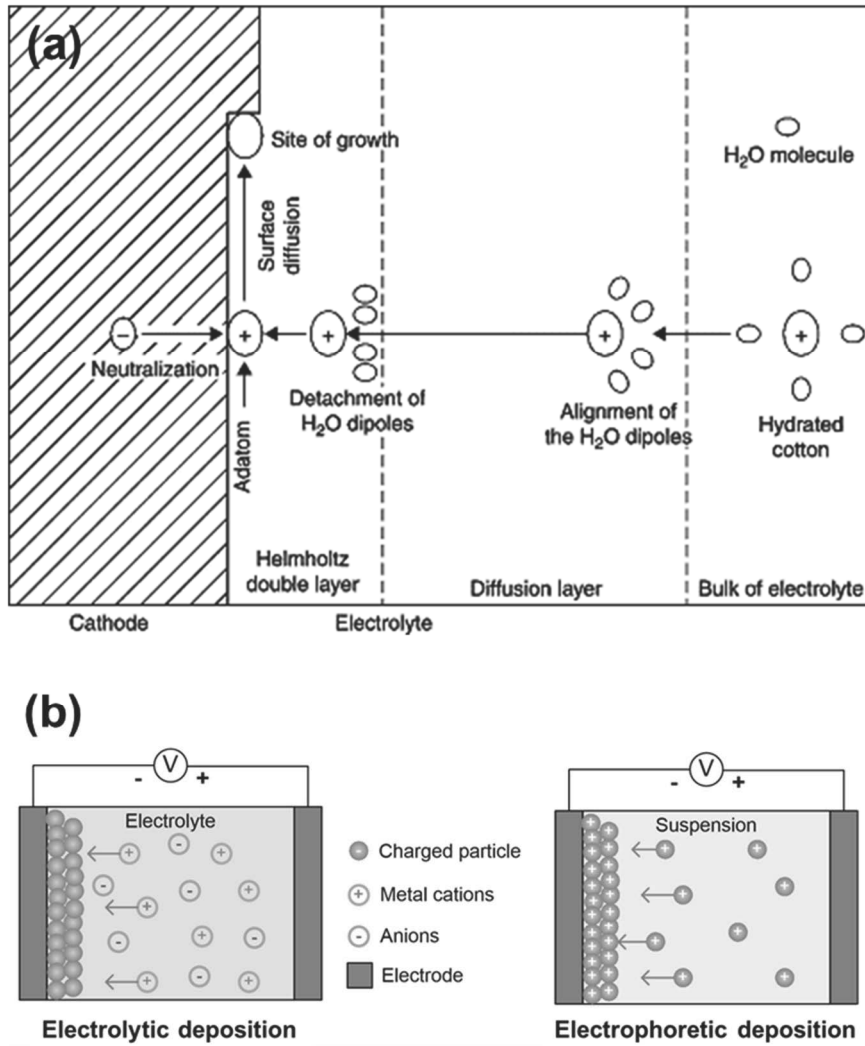
Figure 8. (a) Schematic representation of the electrochemical deposition of metals in cathode [83]. (b) Schematic representation of the two types of cathodic electrodeposition processes: electrolytic and electrophoretic deposition [81].

1.1.3. Sensor application

Sensors are a kind of electronic devices that are designed to detect the changes or stimuli in the environment, convert the detection into electrical signals, and display the signals easily for humans. As modern civilization technology develops rapidly, and a lot of electronic machines are automated, sensor devices are expected to become more compact and be applied in our all over real life, such as internet-of-things (IoT), medical treatment, smart phone, automobile, aerospace, robotics, and artificial intelligence [84–88].

The high performance sensors have several important factors requied: high sensitivity, high selectivity to target analyte, rapid response and recovery time, low operating temperature, and durability in ambient condition. In order to meet these conditions, the transducers of sensor device, the active sensing materials contacting with target, have to be modified demonstrating high surface area, electrical conductivity, and activity to target analyte [89].

The sensors can be classified into chemical sensor, biosensor, optical sensor, pressure sensor, and so on, according to target analytes [90–103]. Among these sensors, chemical sensors are designed to detect trace amount of hamful chemical compounds with liquid or gas phase used in

actual industry. The chemical sensors are specially focused on industrial environment because it is directly connected to safety. Ongoing research and development on chemical sensors can reduce and prevent industrial accidents and underpin better development.

1.1.3.1. Resistive chemical sensor

Chemical sensors, especially gas sensors, play an important role in areas such as industrial safety, environmental pollution monitoring, and military science. Within the chemical sensors, resistive chemical sensors (i.e., chemiresistive sensors) are preferred system due to their simple operation mechanism, low cost, compactness, and high sensitivity [104–108]. The underlying principle of chemiresistive sensors is to observe the resistive changes of active layer upon exposure to target gas through donating or withdrawing electrons between transducer and analytes (**Figure 9**). Because of this electronical mechanism, the sensitivity of chemiresistive sensor depend on the transducer materials with relating properties. Thus, like other sensors, enhancing specific surface area, electrical conductivity, and affinity to target analyte are crutial factors for increasing sensing performance.
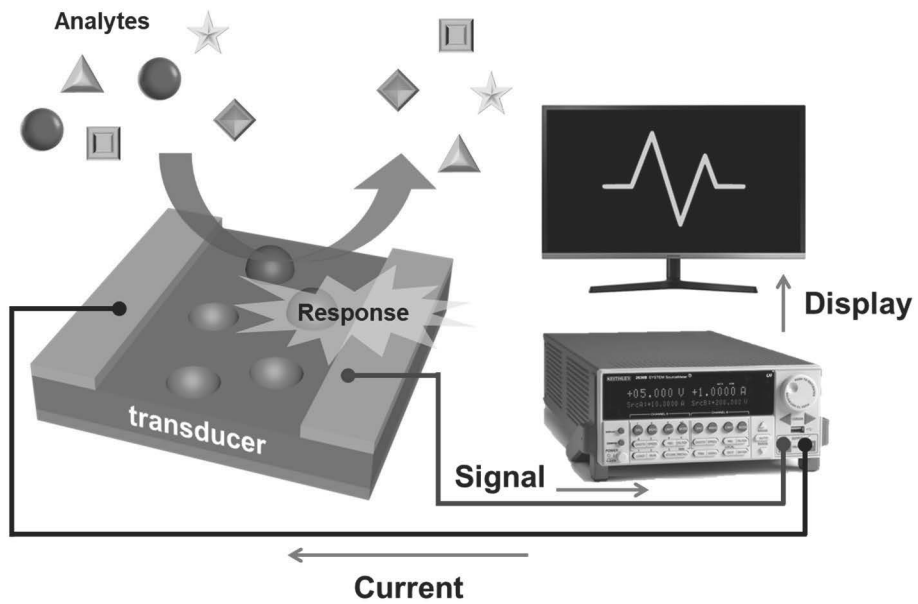
Figure 9. Simplified sensing mechanism of the chemiresistive gas sensor device.

1.1.3.1.1. Ethanol gas sensor

Ethanol is one of the aliphatic alcohols, known as volatile organic compound (VOC), naturally produced by the fermentation of sugars or *via* petrochemical processes. Ethanol is a flammable, colorless liquid with a slight characteristic odor, and volatile because of low molecular weight and high vapor pressure. Ethanol is used in medical application, recreational drug, fuel, feedstock, and conventional chemical solvent. However, even low concentration, ethanol vapor can cause nausea and fatigue in human body. At higher concentration, it becomes toxic and causes heath problems in human body, like visual disorders, black out, and respiratory failure [109–112]. Thereby, the establishment of an organized ethanol gas sensor system for human health management is demanded.

1.1.3.1.2. Ammonia gas sensor

Ammonia is a nitrogeneous compound that is used in fertilizers, building blocks for pharmaceutical products, antimicrobial food agent, and the source of silicon nitride existing gasous phase in nature, both terrestrially and in the outer planets of the Solar system. However, ammonia gas is classified as an extremely hazardous substance because

it is caustic, hazardous in its concentrated form. Furthermore, ammonia gas is exceedingly toxic and dangerous to human respiratory system even with short exposures [113–115]. Therefore, constructing prompt and sensitive ammonia gas sensor system is necessary for the safety of the industrial working environment.

In general, metal oxide semiconductors, such as tin oxide, zinc oxide, titanium oxide, and indium oxide, have been considered representative sensing materials for hazardous gas detection. However, these metal oxide based gas sensors have fatal drawbacks that requiring high operating temperature and relative low sensitivity. To overcome these shortcomings, carbon based organic nanomaterials are studied as alternative transducer of hazardous gas sensor recently due to their applicability at room temperature, high sensitivity with rapid response and recovery time, and chemical stability [116–118].

1.1.3.1.3. Hydrogen gas sensor

Hydrogen gas is the lightest molecule widely used in various industries, such as semiconductor, petrochemical refinery, coolant, chemical compounds synthesis, fuel-cell, automobile, aerospace, and energy carrier in nuclear fusion power plant. Recently, hydrogen energy

is drawing attention for an alternative to fossil fuels as a clean energy source because hydrogen gas only emits water, no pollutant, when combusted. In spite of many benefits and utilities, hydrogen gas is difficult to handle and store because even a little gas leak leads to a massive explosion [119–123]. Hence, establishing systematic high performing gas sensor is required to monitoring and prevising for leakage of colorless and odorless hydrogen gas.

In Pt based chemiresistive hydrogen gas sensor, the hydrogen gas is adsorbed and dissolved into the noble metal transducer, then, the resistance of the transducer changes as the phase of active materials changes from platinum (Pt) to platinum hydride (PtH_x). In order to increase price competitiveness by minimizing the amount of Pt, it is important to increase the sensitivity with increasing the specific surface area of the transducer [124–128].

1.2. Objectives and Outlines

1.2.1. Objectives

In the preceding section, the importances of morphological and chemical modification of PCNWLs were introduced from the viewpoint of academic research and practical applications. The aim of this doctoral dissertation is to describe the methods for morphological and chemical modification of PCNWLs by shape morphology control, fluorine doping, and platinum structure introduction, besides, their gas sensor application toward ethanol, ammonia, and hydrogen gas, respectively. Concretely, PCNWLs are fabricated for enhanced specific surface area and used as active materials into the PCNWLs-based ethanol gas sensor electrodes. The PCNWLs-based gas sensor devices are evaluated outstanding real-time sensing performance toward ethanol gas. Subsequently, the PCNWLs are modified by fluorine doping (FPCNWLs) and platinum villus structure deposition (PtPCNWLs) using vacuum plasma treatment and electrochemical deposition method to improve sensing abilities toward ammonia and hydrogen gas, respectively. The physicochemical and electrical properties of the prepared active transducer materials and

sensing performance of gas sensor devices are investigated systematically and thoroughly.

This study provides distinctive approaches from the morphological and chemical modification of sensor transducer materials to improve the sensing performance of gas sensor electrode, which are pivotal factors for the application in real life.

1.2.2. Outlines

This doctoral dissertation focused on the morphological and chemical modification of PCNWLs and evaluation of their real-time gas sensing performances. This doctoral dissertation involves the following subtopics:

I. Shape control of PAN-derived porous carbon nanoweb layer for ethanol gas sensor: Shape morphology control

II. Fluorination of porous carbon nanoweb layer for ammonia gas sensor: Heteroatom doping

III. Platinum villus overlaid porous carbon nanoweb layer for hydrogen gas sensor: Metal introduction

Each subtopics contains experimental details, characterizations of fabricated materials, and real-time gas sensing performances.

2. Experimental Details

2.1. Shape control of PAN-derived porous carbon nanoweb layer for ethanol gas sensor: Shape morphology control

2.1.1. Materials

Polyacrylonitrile (PAN, M_w 150,000), polystyrene (PS, M_w 35,000), N,N-dimethylformamide (DMF, 99.5%), sulfuric acid (98%), hydrogen peroxide (34.5%), and methylene blue (MB, 99.5%) were purchased from Sigma-Aldrich Co., Ltd. Silicon wafers with a 300 nm SiO_2 (SiO_2/Si) were acquired from Inter-University Semiconductor Research Center (ISRC) at Seoul National University and prepared by dicing into smaller squares (2×2 cm^2). All chemicals were used as received without further purification. Deionized (DI) water was used in all experiment.

2.1.2. Fabrication of polymer mixture solution

Each PAN and PS polymer solution was prepared by dissolving 1.0 g of polymer in 10 ml of DMF at 60 ℃ for 6 h with vigorous stirring. Then, the PAN and PS solutions were mixed in various ratios from 3:1 to 1:3 for 6 h resulting in a polymer mixture solution.

2.1.3. Fabrication of porous carbon nanoweb layers (PCNWLs)

First of all, clearly diced SiO_2/Si wafer substrates were soaked in piranha solution (sulfuric acid:hydrogen peroxide = 3:1) for 30 min and rinsed three times with DI water and ethanol, respectively. Then, these substrates were dried at vacuum oven at room temperature overnight.

After these preconditioning processes, prepared various ratio of polymer mixture solutions were spin-coated onto the SiO_2/Si substrate at 3000 rpm for 60 s. Then, the PCNWLs were fabricated by two steps of thermal treatments under air condition at 300 ℃ with heating rate of 1 ℃ min^{-1} for 10 h and under nitrogen condition (70 sccm) at 800 ℃ with heating rate of 2 ℃ min^{-1} for 1 h. The first step was stabilization step of PAN as well as etching step of PS and the second step was carbonization step of stabilized PAN layer.

2.1.4. Determination of specific surface area of PCNWLs

Specific surface areas of each condition of PCNWLs were measured through dye absorption process. The methylene blue (MB) dye aqueous solutions were prepared with various concentration (from 0.5 to 10 mg L^{-1}). Each PCNWLs was immersed in 10 ml of dye solution and kept at

room temperature for 24 h. The amount of absorbed MB was determined *via* ultraviolet-visible (UV-vis) light spectrophotometer at 664 nm and calculated by following equation [129–133]:

$$q_e = \frac{(C_0 - C_e)V}{m}$$

Beer-Lambert law

$$C = \frac{A}{\varepsilon l}$$

Langmuir isotherm

$$\frac{C_e}{q_e} = \frac{1}{K_L q_m} + \frac{C_e}{q_m}$$

ε : dye absorptivity (molar absorption coefficient) [L mol^{-1} cm^{-1}]

l : beam path length [cm]

C : concentration of dye [mol L^{-1}]

q_e : dye absorption capacity (the amounts of absorbed dye per gram of adsorbent at equilibrium) [mg g^{-1}]

C_0 and C_e : initial and equilibrium concentration of dye [mol L^{-1}]

V : volume of the dye solution [L]

m : the mass of the adsorbent used [g]

q_m : maximum dye adsorption capacity [mg g^{-1}]

K_L : Langmuir isotherm constant

The absorptivity of MB is 95,000 L mol^{-1} cm^{-1} at 664 nm in literature [134–135]. Then, the specific surface area of adsorbent (PCNWLs in my work) is readily calculated through following equation [129–130]:

$$S_{MB} = \frac{N_A A_{MB} q_m}{M_{MB}}$$

S_{MB} : specific surface area [m^2 g^{-1}]

N_A : Avogadro's number, 6.02×10^{23}

A_{MB} : the occupied surface area of one MB molecule, 197.2×10^{-20} m^2

M_{MB} : the molecular weight of MB

2.1.5. Characterization of PCNWLs

Field emission scanning electron microscope (FE-SEM) analysis were carried out using a JSM-6701F (JEOL) to compare the shape morphology differences. Optical microscope (OM) images were obtained using a Nikon LV100 microscope (Nikon, Japan). Thermogravimetric analysis (TGA) curves were measured under atmospheric conditions using a Pyris 6 thermogravimetric analyzer (PerkinElmer) with a heating rate of 1 ℃ min^{-1}. Fourier transform infrared (FT-IR) spectra were collected with a Frontier spectro photometer (PerkinElmer) in attenuated total reflection mode. Raman spectroscopy and X-ray photoelectron spectroscopy (XPS) analyses

were measured using a DXR2xi (Thermo) and a Sigma Probe (ThermoFisher Scientific), respectively, at the National Center for Inter-University Research Facilities (NCIRF) at Seoul National University. UV-vis spectra were obtained using a Lambda 35 (PerkinElmer) to compare the specific surface area. Atomic force microscope (AFM) analysis was carried out using Innova (Bruker) at the Chemical and Biological Engineering Research Facilities (CBRF) at Seoul National University. Electrical conductivity was measured using 4-point-probe method at ambient temperature with a source meter of Keithly 2400 (Keithly).

2.1.6. Electrical sensing measurement of PCNWLs for ethanol gas sensor

PCNWL gas sensor devices were constructed with patterning gold electrode deposition by thermal evaporator. To measure the resistance change of PCNWL electrode upon ethanol gas exposure, the PCNWL sensor electrode was placed inside the gas chamber and connected with a source meter to monitor the change of resistance. Various gas concentrations of ethanol (20 ppb – 200 ppm) were controlled by a bubbler (to vaporize organic compounds) and a mass flow controller

(MFC, KNH Instruments) mixing organic vapors with nitrogen gas.

The real-time sensing proceeded with monitoring the resistance changes by applying a constant current of 10^{-6} A to the PCNWL sensor electrode and the sensitivity was defined as calculating the normalized electrical resistance changes:

$$S = \frac{\Delta R}{R_0} = \frac{(R - R_0)}{R_0} \; (\%)$$

S : sensitivity [%]

R : real-time measured resistance

R_0 : initial measured resistance

Moreover, the response time and the recovery time was defined as the time required for a sensor to reach 90% of maximum sensitivity value after the gas exposure and 10% of the preceding sensitivity value after purging with nitrogen gas.

2.2. Fluorination of porous carbon nanoweb layer for ammonia gas sensor: Heteroatom doping

2.2.1. Materials

Polyacrylonitrile (PAN, M_w 150,000), N,N-dimethylformamide (DMF, 99.5%), polystyrene (PS, M_w 35,000), hydrogen peroxide (34.5%), sulfuric acid (98%) were purchased from Sigma-Aldrich Co., Ltd. Silicon wafers with a 300 nm SiO_2 (SiO_2/Si) were obtained from Inter-University Semiconductor Research Center (ISRC) at Seoul National University and prepared by cutting into smaller pieces (2×2 cm^2). All chemicals were used as received without further purification and deionized (DI) water was used in all experiment.

2.2.2. Fabrication of fluorinated porous carbon nanoweb layers (FPCNWLs)

PCNWLs, which is the template for fluorination to fabricate FPCNWLs, follows the same synthetic procedure as my previous work. First, SiO_2/Si wafer substrates were immersed in piranha solution (H_2SO_4: H_2O_2 = 3:1) for 30 min and rinsed three times with DI water and ethanol, respectively. Then, these cleared substrates were dried at

vacuum oven at room temperature overnight. Each PAN and PS polymer solution was prepared by dissolving 1.0 g of each polymer in 10 ml of DMF at 60 ℃ for 6 h with vigorous stirring. Then, the prepared PAN and PS solutions were mixed in ratio of 1:1 for 6 h resulting in a polymer mixture solution. The prepared polymer mixture solutions were spin-coated onto the SiO_2/Si substrate at 3000 rpm for 60 s. Then, two steps of thermal treatments under air condition at 300 ℃ with heating rate of 1 ℃ min^{-1} for 10 h and under nitrogen condition (70 sccm) at 800 ℃ with heating rate of 2 ℃ min^{-1} for 1 h proceeded to fabricate the PCNWL.

Fluorination of PCNWLs were demonstrated *via* vacuum plasma treatment (Korea Vacuum Co.). The F plasma curtain was produced by RF controller (100 W) with octafluorocyclobutane (C_4F_8) gas flow at a flow rate of 15 sccm. The FPCNWLs were fabricated with differential plasma treating time from 2 to 80 min.

2.2.3. Characterization of FPCNWLs

Field emission scanning electron microscope (FE-SEM) and energy dispersive X-ray spectroscopy (EDS) analyses were carried out using a JSM-6701F (JEOL) equipped with an EDS spectrometer (Inca). FT-IR spectra were collected with a Frontier spectrophotometer (PerkinElmer)

in attenuated total reflection (ATR) mode. Raman spectroscopy and X-ray photoelectron spectroscopy (XPS) spectra were obtained using a DXR2xi (Thermo) and a Sigma Probe (ThermoFisher Scientific), respectively, at the National Center for Inter-University Research Facilities (NCIRF) at Seoul National University. Electrical conductivity was measured using 4-point-probe method at room temperature with a source meter of Keithly 2400 (Keithly).

2.2.4. Electrical sensing measurement of FPCNWLs for ammonia gas sensor

FPCNWL gas sensor devices were fabricated with patterning gold electrode deposition by thermal evaporator. To measure the resistance change of FPCNWL electrode upon ammonia gas exposure, the FPCNWL sensor electrode was placed inside the gas chamber and connected with a source meter (Keithly 2400, Keithly) to monitor the change of resistance. Various gas concentrations of ethanol (9 ppb – 90 ppm) were controlled by a bubbler (to vaporize organic compounds) and a mass flow controller (MFC, KNH Instruments) mixing organic vapors with nitrogen gas.

The real-time sensing was demonstrated with monitoring the

resistance changes by applying a constant current of 10^{-6} A to the FPCNWL sensor electrode and the sensitivity was defined by following equation:

$$S = \frac{\Delta R}{R_0} = \frac{(R - R_0)}{R_0} \ (\%)$$

S: sensitivity

R: real-time measured resistance

R_0: initial measured resistance

Moreover, the response time and the recovery time was defined as the time required for a sensor to reach 90% of maximum sensitivity value after the gas exposure and 10% of the preceding sensitivity value after purging with nitrogen gas.

2.3. Platinum villus overlaid porous carbon nanoweb layer for hydrogen gas sensor: Metal introduction

2.3.1. Materials

Polyacrylonitrile (PAN, M_w 150,000), polystyrene (PS, M_w 35,000), *N,N*-dimethylformamide (DMF, 99.5%), sulfuric acid (98%), hydrogen peroxide (34.5%) were purchased from Sigma-Aldrich Co., Ltd. Platinum (IV) chloride ($PtCl_4$) was purchased from Kojima Chemical. Si wafers with a 300 nm SiO_2 (SiO_2/Si) were acquired from Inter-University Semiconductor Research Center (ISRC) at Seoul National University and prepared by dicing into smaller squares (2×2 cm^2). All chemicals were used as received without further purification and deionized (DI) water was used in all experiment.

2.3.2. Fabrication of platinum villus overlaid porous carbon nanoweb layers (PtPCNWLs)

Platinum nanostructure on the PCNWLs was fabricated *via* electrochemical deposition. PCNWLs, which is the template for platinum villus structure, follows the same synthetic protocol as my previous work. First, clearly diced SiO_2/Si wafer substrates were

immersed in piranha solution (H_2SO_4: H_2O_2 = 3:1) for 30 min and rinsed three times with DI water and ethanol, respectively. Then, these cleared substrates were dried at vacuum oven at room temperature overnight. Moreover, each PAN and PS polymer solution was prepared by dissolving 1.0 g of each polymer in 10 ml of DMF at 60 ℃ for 6 h with vigorous stirring. Then, the prepared each polymer solutions were mixed in ratio of 1:1 for 6 h resulting in a polymer mixture solution. The prepared polymer mixture solutions were spin-coated onto the SiO_2/Si substrate at 3000 rpm for 60 s. Then, two steps of thermal treatments under air condition at 300 ℃ with heating rate of 1 ℃ min^{-1} for 10 h and under nitrogen condition (70 sccm) at 800 ℃ with heating rate of 2 ℃ min^{-1} for 1 h proceeded to fabricate the PCNWL.

To construct Pt villus structure, electrochemical deposition was carried out at various working voltages from –0.5 V to –2.0 V for 10 min at room temperature in an electrolyte consisiting of various concentration of $PtCl_4$ from 0.1 mM to 5 mM in 0.5 M H_2SO_4 aqueous solution. All electrochemical experiment performed with the Pt counter electrode and Ag/AgCl reference electrode. Prepared PCNWL was used as working electrode.

2.3.3. Characterization of PtPCNWLs

Electrochemical deposition was carried out with an electrochemical workstation (ZIVE SP2, Zahner Elektrik IM6 analyzer). Field emission scanning electron microscope (FE-SEM) and energy dispersive X-ray spectroscopy (EDS) analyses were conducted using a JSM-6701F (JEOL) equipped with an EDS spectrometer (Inca). Raman spectroscopy and X-ray photoelectron spectroscopy (XPS) analyses were demonstrated using a DXR2xi (Thermo) and a Sigma Probe (ThermoFisher Scientific), respectively, at the National Center for Inter-University Research Facilities (NCIRF) at Seoul National University. X-ray diffraction (XRD) patterns were obtained using a Smart Lab (Cu tube, Rigaku) at the Chemical and Biological Engineering Research Facilities (CBRF) at Seoul National University. Electrical conductivity was measured using 4-point-probe method at ambient temperature with a source meter of Keithly 2400 (Keithly).

2.3.4. Electrical sensing measurement of PtPCNWLs for hydrogen gas sensor

PtPCNWL gas sensor devices were fabricated with patterning gold electrode deposition by thermal evaporator. To measure the resistance

change of PtPCNWL electrode upon hydrogen gas exposure, the PtPCNWL sensor electrode was placed inside the gas chamber and connected with a source meter (Keithly 2400, Keithly) to monitor the change of resistance. Various gas concentrations of H_2 gas (10 ppm – 200 ppm) were controlled by a mass flow controller system (MFC, KNH Instruments).

The real-time sensing was demonstrated with monitoring the resistance changes by applying a constant current of 10^{-4} A to the PtPCNWL sensor electrode and the sensitivity was defined by following equation:

$$S = \frac{\Delta R}{R_0} = \frac{(R - R_0)}{R_0} \ (\%)$$

S: sensitivity

R: real-time measured resistance

R_0: initial measured resistance

The evaluation of sensing performance of H_2 gas proceeded in ambient condition at relative humidity of *ca.* 20%.

3. Results and Discussion

3.1. Shape control of PAN-derived porous carbon nanoweb layer for ethanol gas sensor: Shape morphology control

3.1.1. Construction of porous carbon nanoweb layer (PCNWL)

Polyacrylonitrile-derived porous carbon nanoweb layers (PCNWLs) were constructed *via* spin-coating of PAN and PS polymer mixture solution, followed by two step of thermal treatment, as illustrated in **Figure 10**. Among the polymer mixture solution, the PAN is the carbon source, which is a framework, and the PS is a role of making pores into the carbon layer. Adjusting PS amount in the polymer mixture solution can control pore size and porosity. During the first thermal treating step, PS was pyrolyzed forming various pore sizes on and into the layer. Furthermore, the linear chain of the PAN converted to carbon hexagonal chain rings with nitrogen [136]. After proceeding up to second carbonization step, the nitrogen doped PCNWLs were manufactured readily.

As mentioned earlier, the shape morphology of PCNWLs can easily alter adjusting the mixing ratio of the PAN and PS. The FE-SEM images

of PCNWLs fabricated with only PAN (PCNWL00) and varying PAN/PS mixing ratio of 3:1, 2:1, 1:1, 1:2, 1:3 (PCNWL31, PCNWL21, PCNWL11, PCNWL12, PCNWL13) were demonstrated in **Figure 11**. As the PS ratio increased, both pore size and porosity increased gradually. However, excessive amount of PS as against that of PAN, the carbon structure showed angular shape because the PAN is the framework and the PS is the vanishing part. Moreover, the difference of molecular weight between PAN and PS also affected the shape of the PCNWLs. As the molecular weight of PAN is higher than that of PS (150k and 35k, respectively), a viscosity of the polymer mixture decreases where the amount of PS increased, as displayed in **Figure 12**. The viscosity of polymer mixture solution influenced the thickness of the PCNWLs. The thickness was estimated through cross-sectional SEM image in the inset of **Figure 11** and the measured value of each PCNWLs were organized in **Figure 13**. The layer thickness of PCNWLs was measured *ca.* 684 nm (PCNWL00), 441 nm (PCNWL31), 358 nm (PCNWL21), 302 nm (PCNWL11), 215 nm (PCNWL12), and 161 nm (PCNWL13), respectively. As the amount of PS increased (the viscosity decreased), the thickness of PCNWL decreased due to properties of spin coating [137–139]. Furthermore, lower viscosity suppresses the aggregation of

the adjacent polymer, especially PAN, during spin-coating process. This loose interaction between PAN molecules can affect different pore size and furtherly conductivity after carbonization. For understanding a definite tendency, OM images were exhibited in **Figure 14**. In digital image of each condition of polymer mixture solution (**Figure 14a**), the color changed from yellowish to opaque white as the content of PS increased because the colors of PAN and PS solution are yellow and colorless, respectively. The PAN and PS solution were immiscible, forming microemulsion due to their different surface tension, polarity, and molecular weight. **Figure 14b–f** shows the different size of polymer islands as varying mixing ratio of PAN and PS from 3:1 to 1:3. In mixture solution, PAN solution composed discontinuous phase constituting polymer islands in the continuous phase of PS solution due to higher molecular weight and polarity [140–143]. With PAN amount decreased (PS amount increased), the size and amount of PAN islands decreased. Since the PAN is the carbon source constructing the carbon framework of PCNWLs, PAN islands were assembled when the spin-coating process. Concurrently, partial amount of PS also assembled inside of PAN framework, which generate mesopores of carbon structure. Besides, most of PS were coated outside of frame forming various macropores.
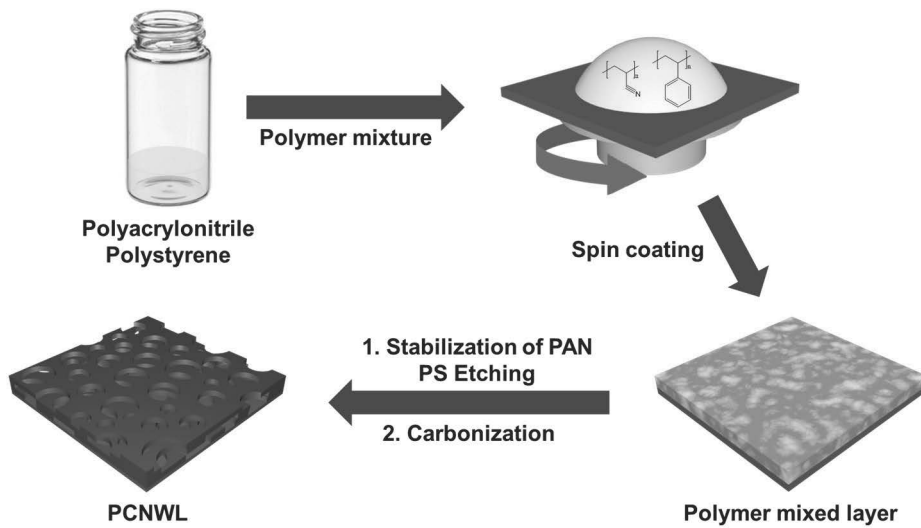
Figure 10. Schematic representation of sequential fabricating process of PCNWLs.
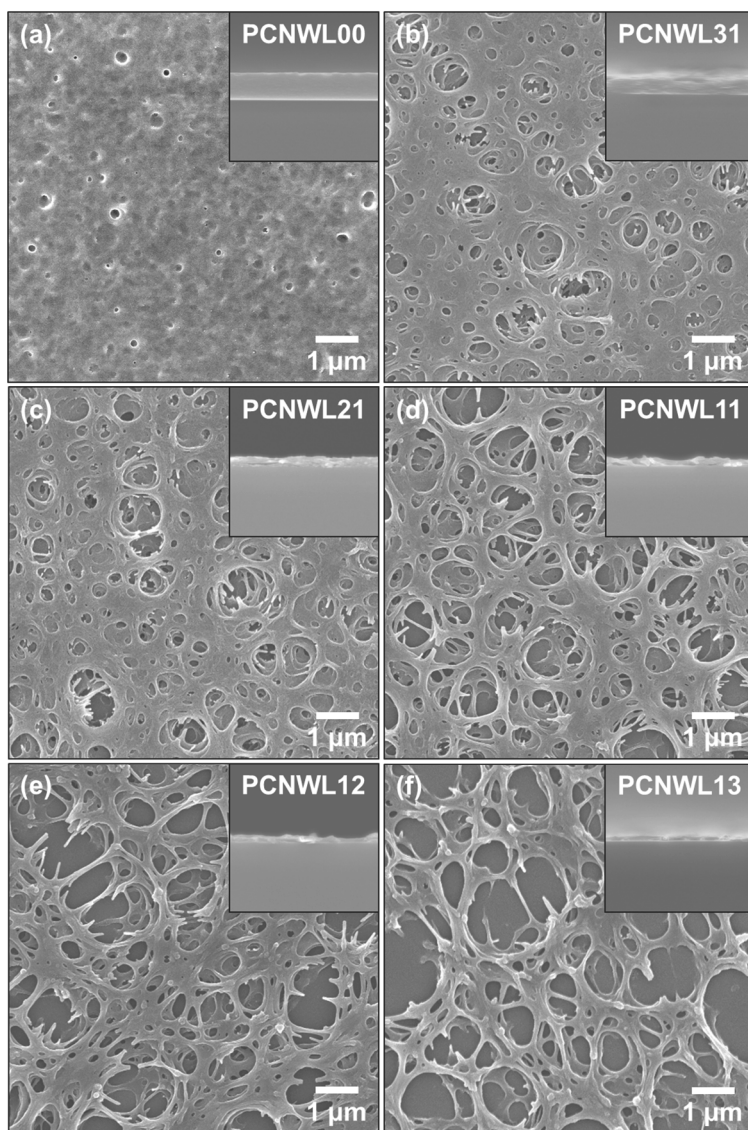
Figure 11. FE-SEM images of (a) PCNWL00, (b) PCNWL31, (c) PCNWL21, (d) PCNWL11, (e) PCNWL12, and (f) PCNWL13, respectively. (insert: cross-sectional FE-SEM image of each PCNWLs, respectively)
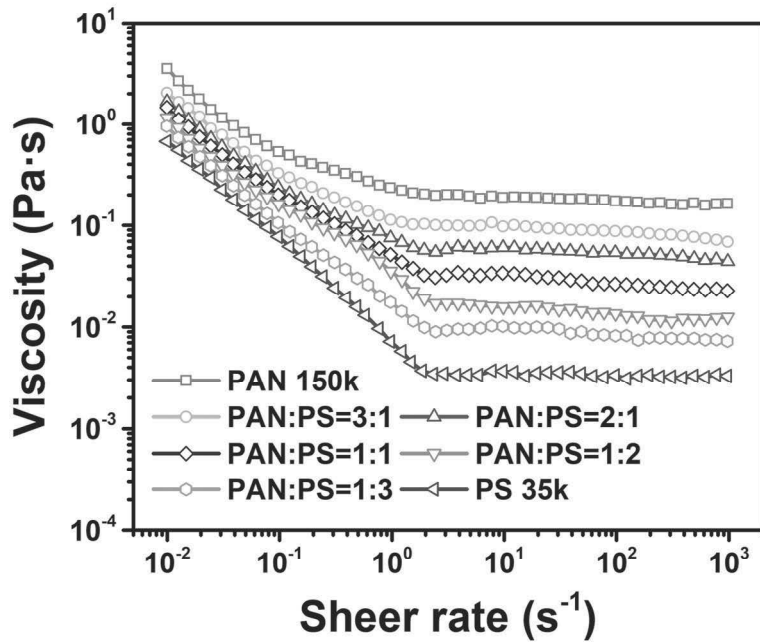
Figure 12. The viscosity of PAN, PS, and different condition of PAN/PS polymer mixtures.
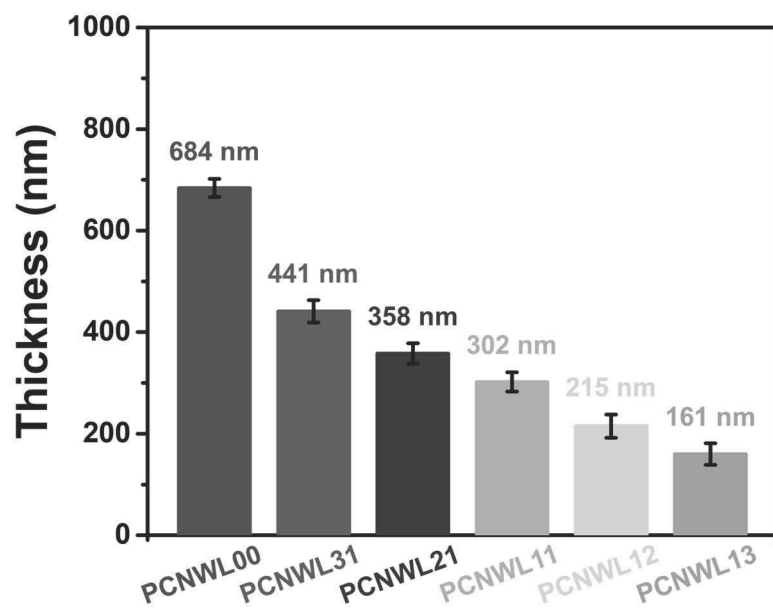
Figure 13. The measured layer thickness of each PCNWLs.
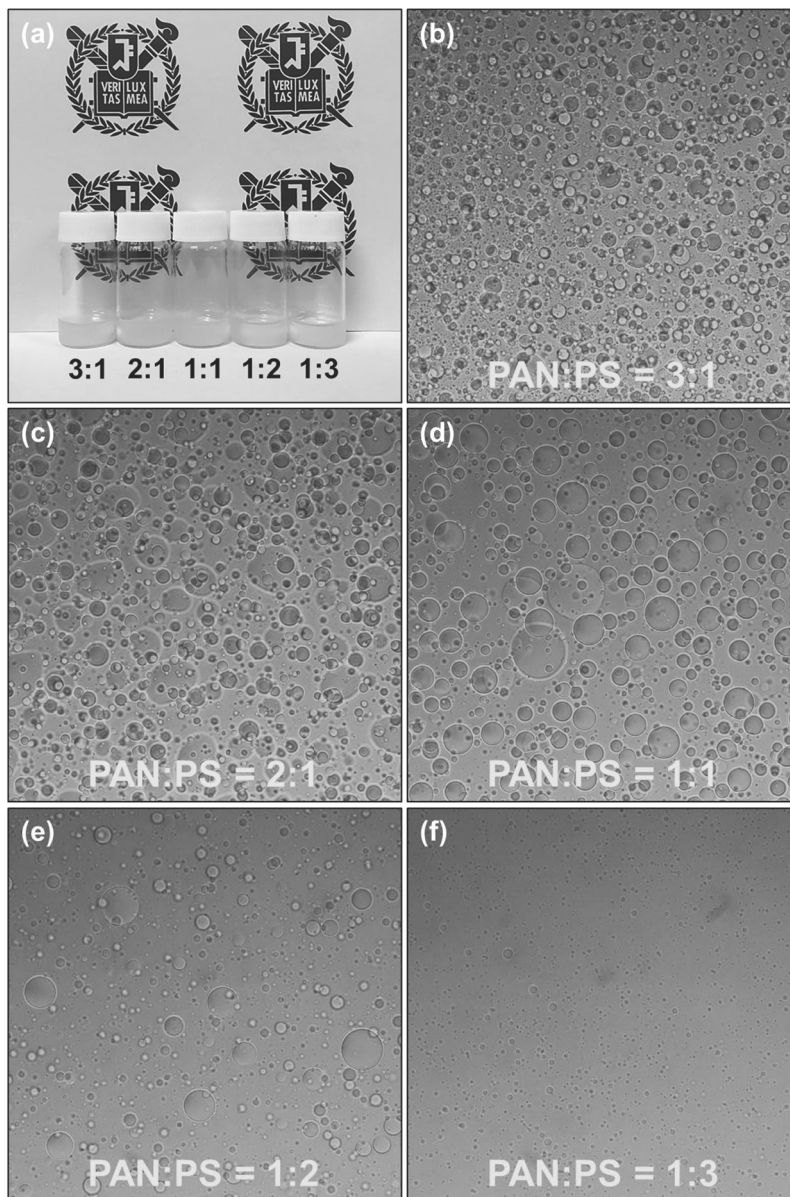
Figure 14. (a) Digital image of each condition of PAN/PS polymer mixture solution. OM images of PAN/PS polymer mixture solutions of (b) 3:1, (c) 2:1, (d) 1:1, (e) 1:2, and (f) 1:3, respectively.

3.1.2. Characterization of PCNWLs

For the detailed study of the first thermal treatment, TGA curves were achieved under atmospheric condition. As shown in **Figure 15**, PS portion at each condition of PCNWLs started to be decomposed at 290 ℃. After the all PS molecules etched, the rest weight of PAN polymer was about 70, 62, 48, 31, and 23% for 3:1, 2:1, 1:1, 1:2, and 1:3 ratio of PAN/PS polymer mixture, respectively. The difference between the original ratio of mixed polymers and measured value was related on the degradation of PAN during the stabilization. There were slight weight drop around 250 ℃ at the TGA curves due to PAN degradation.

To provide any further structural changes during the thermal treatment, FT-IR investigation was accomplished, as displayed in **Figure 16**. The spin-coated polymer mixture layer, before any thermal treatment, showed aromatic C–H bending peaks at 700 and 750 cm^{-1}, aromatic C=C stretching peaks at 1450 and 1500 cm^{-1}, nitrile C≡N stretching peak at 2260 cm^{-1}, and C–H stretching peak around 2950 cm^{-1}, which were characteristic peaks of PS and PAN, respectively [140]. The stabilized PAN layer, which PS was etched after the first thermal treatment, represented some different aspects including disappearance of the distinctive peaks of PS and PAN. It portrayed C=C bendings around 800

cm^{-1}, broad amine C–N stretching between 1000 and 1250 cm^{-1}, aromatic amine C–N stretching around 1250 and 1340 cm^{-1}, and cyclic alkene C=C stretching around 1590 cm^{-1}, which were peculiar peaks of hexagonal carbon chain ring with nitrogen (stabilized PAN) [31,35–36, 38].

Raman spectra were obtained to examine the changes of carbon hexagonal structure introducing pores after carbonization, as depicted in **Figure 17**. The I_D/I_G ratio, 1.34 for PCNWL00 and 1.39 for PCNWL11, increased as the various size of pores were generated during heat treatment. The boundaries between PAN and PS were not transformed impeccably to carbon hexagonal structure while the stabilization process of PAN as well as etching PS.

The elemental and chemical combinations of the PCNWLs were surveyed in detail using XPS analysis. The entire spectrum of PCNWLs had C, N, and O components for concentrations of 84.0%, 11.3%, and 4.7%, respectively. **Figure 18a** revealed the high-resolution spectra of C 1s of PCNWLs. According to deconvoluted C 1s spectra, the peaks at 284.6, 285.4, and 288.2 eV are attributed to C=C, C–N, and C=O bonds, respectively. Additionally, the high-resolution spectra of N 1s of PCNWLs were manifested in **Figure 18b**. The N 1s spectrum was

deconvoluted into four different peaks at 398.1, 400.5, 402.6, and 408.1 eV. They correspond to pyridinic N, pyrrolic N, graphitic N, and oxidized N, respectively. The peak intensity of pyridinic and pyrrolic N were higher than graphitic N, which means the defects in pentagonal and hexagonal structure are superior to typical carbon materials. When PAN and PS were mixed, the functional group of cyanide in PAN and the hydrogen atom in PS are partially combined with partial charge-charge interaction. Therefore, during the thermal treatment of stabilizing PAN, etching PS, and carbonization, carbon and nitrogen atoms can not easily construct the hexagonal structure. Besides, the presence of oxygen was related with the adsorption and oxidation during storage of samples.

The surface roughness of PCNWLs was evaluated by two dimensional (2D) AFM images, as exhibited in **Figure 19**. The measured root-mean-square (RMS) roughness was 13.9 nm for PCNWL00, 28.1 nm for PCNWL31, 38.6 nm for PCNWL21, 39.5 nm for PCNWL11, 76.2 nm for PCNWL12, and 53.2 nm for PCNWL13, respectively (**Table 1**). As the PS ratio increased in polymer mixture solution, the roughness was enhanced although the viscosity of solution, the key point of roughness determinant during spin-coating, was reduced. Meanwhile, the RMS roughness was slightly decreased again at PCNWL13 because the

SiO$_2$/Si wafer surface was exposed due to excessive etching. In principle, the porosity of PCNWLs was more crucial factor of surface roughness than the viscosity of spin-coating solution.

To calculate the specific surface area of PCNWLs, dye absorption method proceeded. Among the many kinds of dye, methylene blue (MB) was used because of its affinity toward carbon materials. Adsorption isotherm experiments were carried out by agitating MB solutions of different concentrations from 0.5 to 10 mg L^{-1} with each condition of one SiO$_2$/Si wafer piece that PCNWL was constructed on. The amount of absorbed MB was measured through UV-vis light spectrophotometer. As described in **Figure 20a and b**, MB showed maximum absorbance at a wavelength of 664 nm. The specific surface areas of PCNWLs calculated with several equations were 286.26 m^2 g^{-1} for PCNWL00, 1148.21 m^2 g^{-1} for PCNWL31, 1172.42 m^2 g^{-1} for PCNWL21, 1256.80 m^2 g^{-1} for PCNWL11, 489.95 m^2 g^{-1} for PCNWL12, and 333.28 m^2 g^{-1} for PCNWL13, respectively (**Table 2**). Through this analysis, PCNWL11 which is adjusting PAN/PS mixing ratio of 1:1 had a highest specific surface area that affects the critical value for sensitivity.
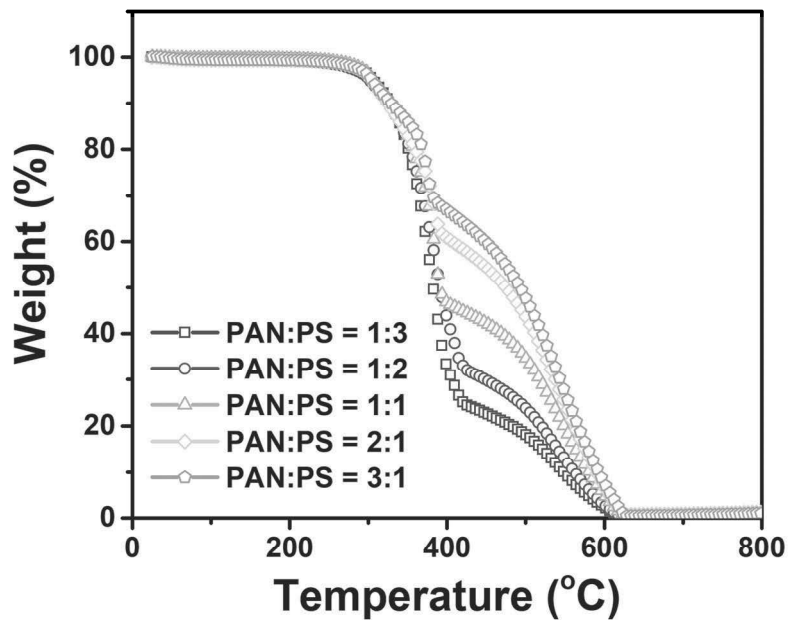
Figure 15. TGA curves of each conditions of PAN/PS polymer mixture solutions.
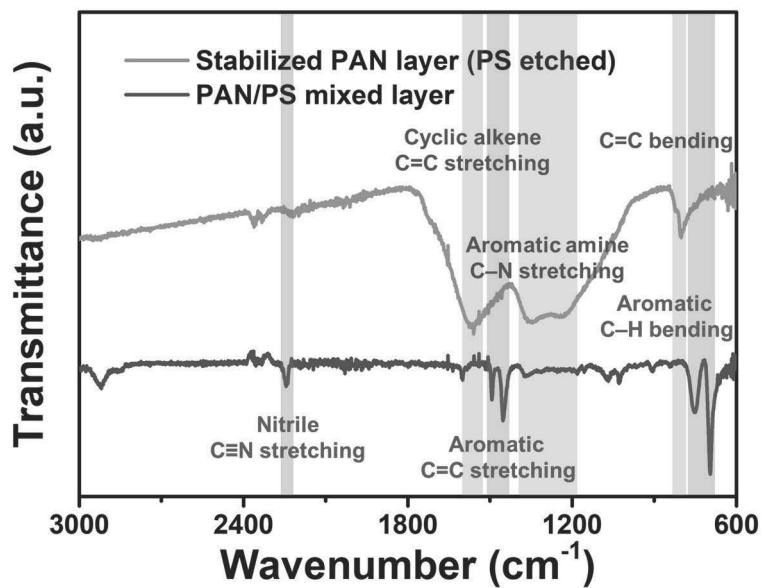
Figure 16. FT-IR spectra of PAN/PS polymer mixed layer and stabilized

PAN layer.
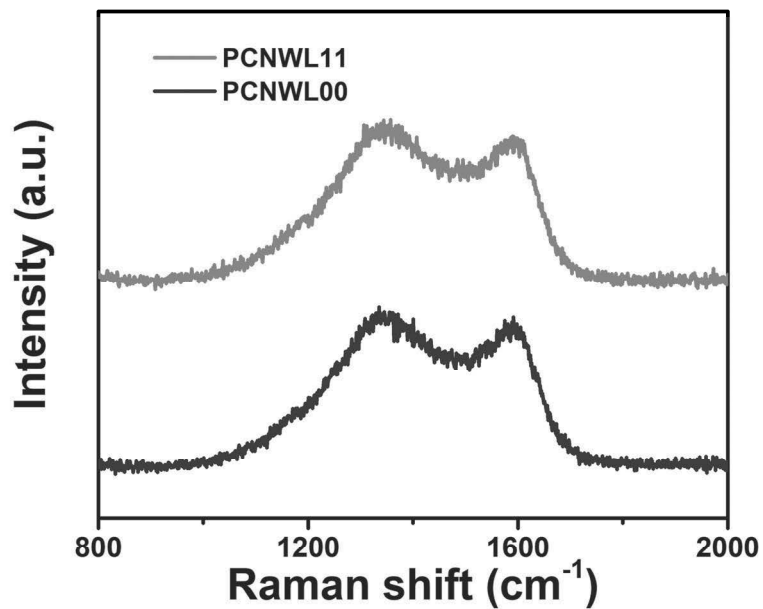
Figure 17. Raman spectra of PCNWL00 and PCWNL11.
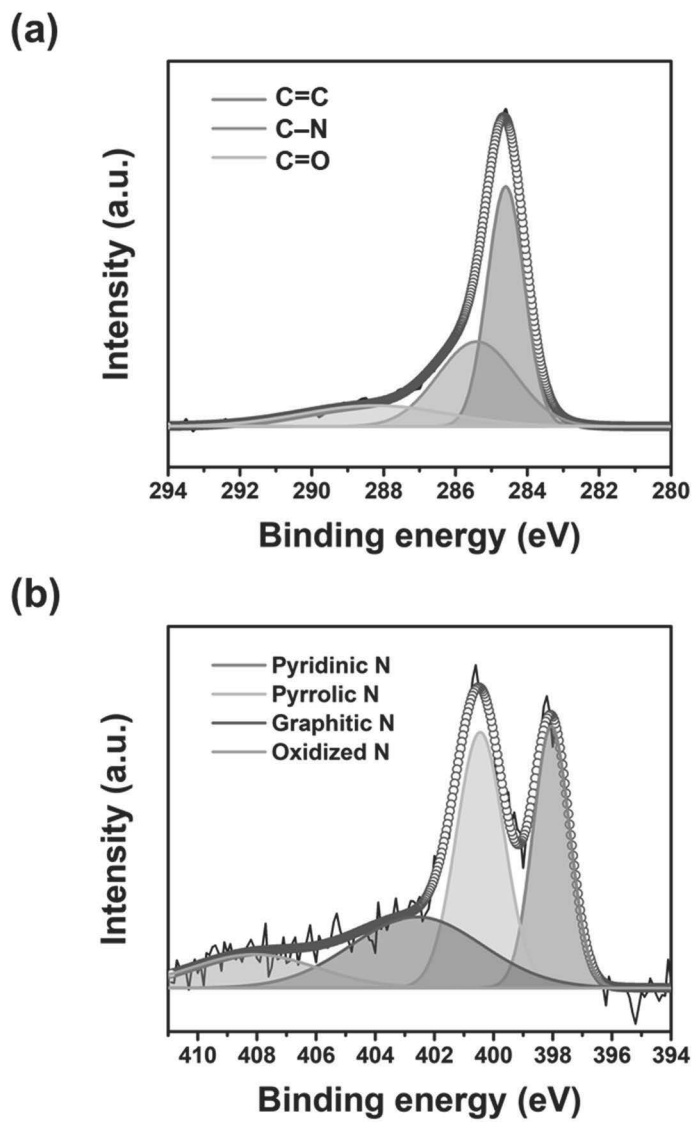
Figure 18. High-resolution of (a) C 1s and (b) N 1s XPS spectra of PCNWLs.
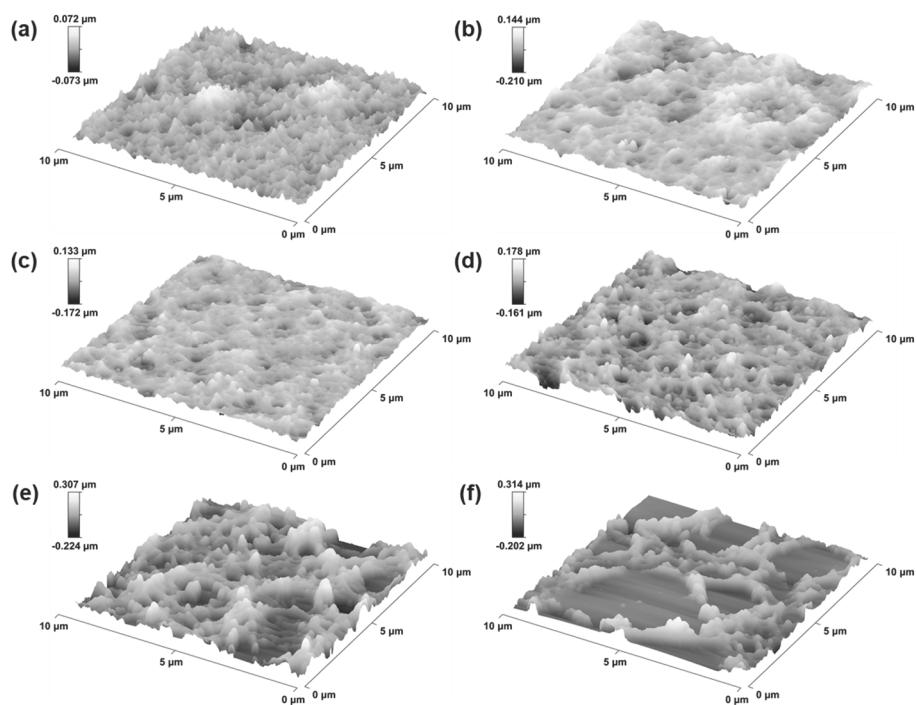
Figure 19. Two dimensional (2D) AFM images of (a) PCNWL00, (b) PCNWL31, (c) PCNWL21, (d) PCNWL11, (e) PCNWL12, and (f) PCNWL13, respectively.

Table 1. The surface roughness of PCNWLs was evaluated by two dimensional (2D) AFM images.

Sample	Surface roughness (nm)
PCNWL00	13.9
PCNWL31	28.1
PCNWL21	38.6
PCNWL11	39.5
PCNWL12	76.2
PCNWL13	53.2
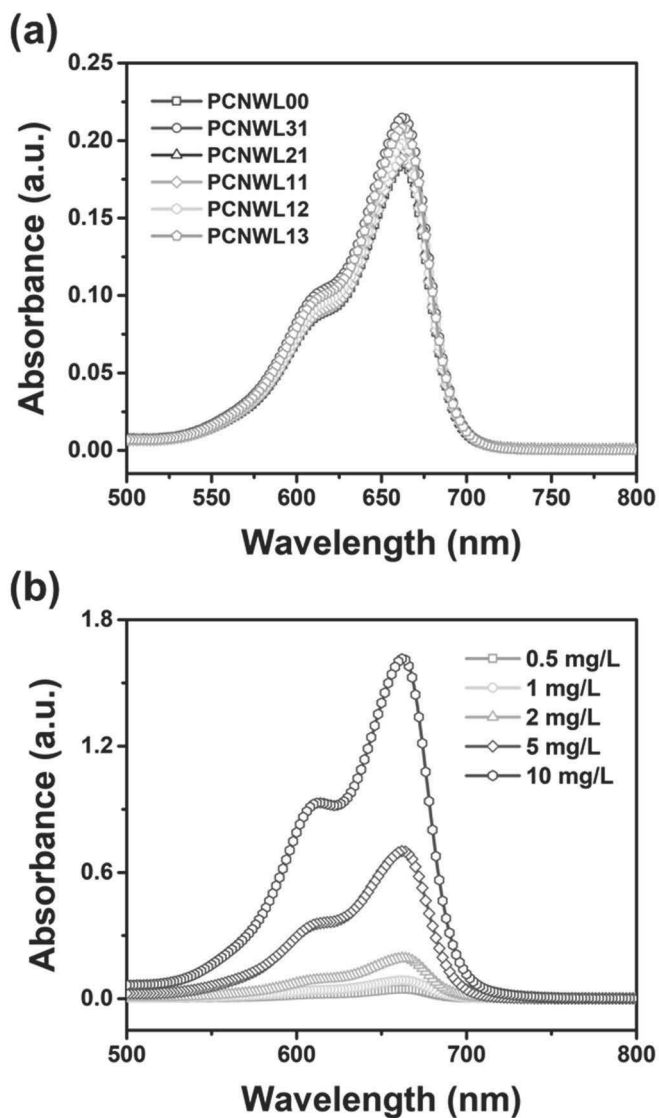
Figure 20. UV-vis light adsorption spectra of (a) each conditions of PCNWLs with the adsorbed MB dyes using 2 mg L^{-1} MB dye aqueous solution. (b) PCNWL11 with the adsorbed MB dyes varying the concentrations of MB dye aqueous solutions from 0.5 to 10 mg L^{-1}.

Table 2. The specific surface areas of PCNWLs measured with MB dye adsorption and calculated with several equations.

Sample	Specific surface area ($m^2\ g^{-1}$)
PCNWL00	286.26
PCNWL31	1148.21
PCNWL21	1172.42
PCNWL11	1256.80
PCNWL12	489.95
PCNWL13	333.28

3.1.3. Electrical properties of ethanol gas sensor electrode based on PCNWLs

The electrical conductivity of PCNWLs was estimated using 4-point probe method. As shown in **Figure 21**, the electrical conductivity was evaluated of 47.18 S cm^{-1} for PCNWL00, 14.36 S cm^{-1} for PCNWL31, 9.84 S cm^{-1} for PCNWL21, 6.91 S cm^{-1} for PCNWL11, 0.25 S cm^{-1} for PCNWL12, and 0.12 S cm^{-1} for PCNWL13, respectively. The conductivity was reduced drastically where the macropores were generated and decreased steadily as the porosity increased. Moreover, the electrical conductivity was dropped immensely once again where the PS portion is over than 50% (between PCNWL11 and PCNWL12).

The PCNWL-based ethanol gas sensor electrodes were constructed with thermal deposition of gold pattern array. A digital image of the PCNWL-based gas sensor electrode is presented in **Figure 22a**. The gold pattern array was obiously deposited on the center of PCNWL. **Figure 22b** demonstrates current–voltage (*I*–*V*) curves proceeded to appraise the electrical contact of the PCNWLs and the gold electrode array. The curves presented linear form for the voltage range from −1.0 V to 1.0 V, indicating that the PCNWLs have an Ohmic contact with the gold array. The contact resistance (*dV/dI*, a reciprocal of the slope) between

PCNWLs and the gold pattern array increased with the pore size and the

surface roughness increased.
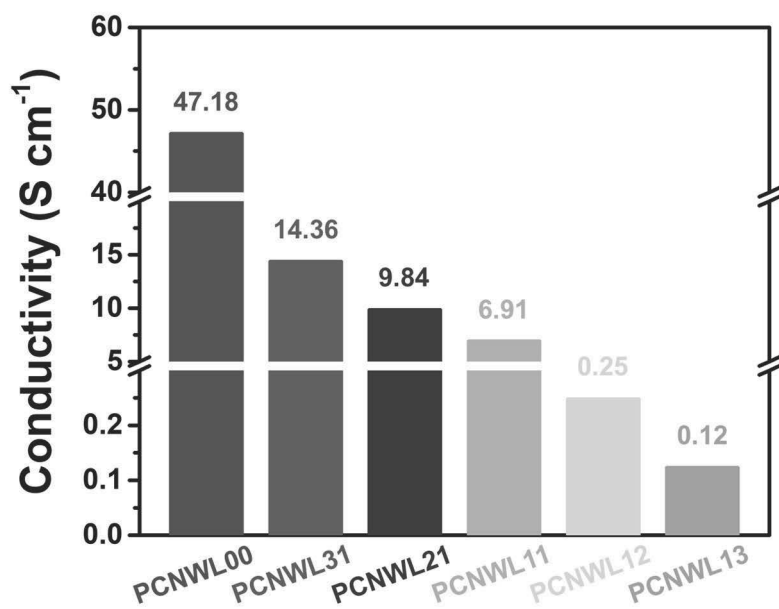
Figure 21. Electrical conductivities of each condition of PCNWLs.
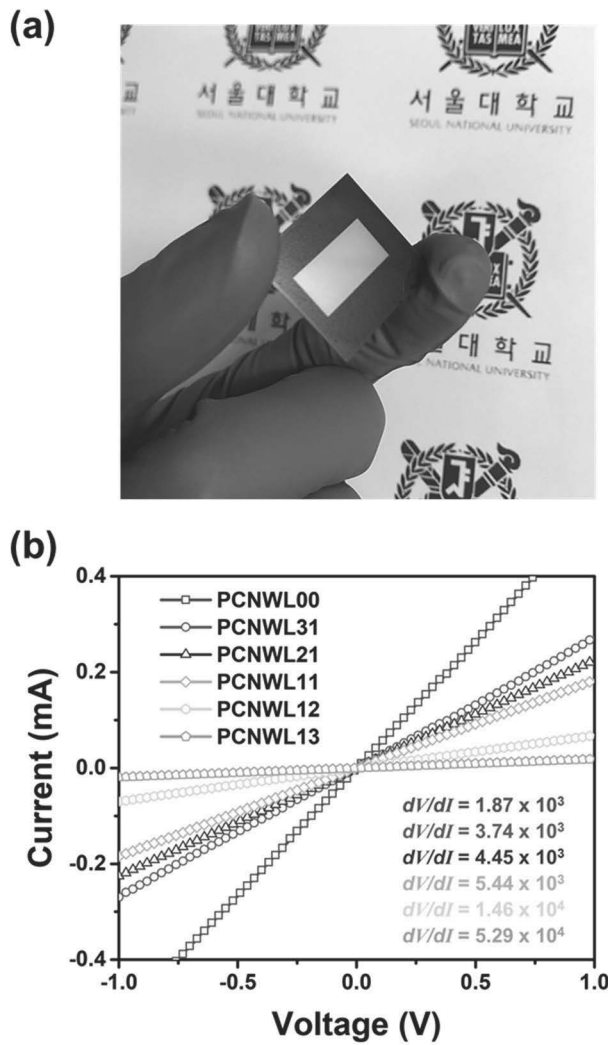
Figure 22. (a) Digital image of the PCNWL-based gas sensor electrode.
(b) *I–V* curves of each conditions of PCNWLs at the voltage range from
–1.0 V to 1.0 V.

3.1.4. Real-time sensing performance of ethanol gas sensor device based on PCNWLs

The sensing mechanism of ethanol vapor is delineated in **Figure 23**. The basic gas sensing mechanism is surface conduction transition by adsorbed gas molecules. Commonly, many volatile organic compounds (VOCs) can be adsorbed with carbon materials at defects of hexagonal structure, end of functional groups, and heteroatoms that are doped. In this PCNWL sensor system, ethanol vapors are physically adsorbed at the defects generated during etching PS and stabilizing PAN, at the epoxy groups that are remained despite carbonization, and at the doped nitrogen atoms forming pyridinic, pyrrolic, and graphitic N oriented from nitrile group of PAN. The main principle of physisorption is van der Waals interaction and hydrogen bond. When the ethanol molecules are exposed to sensing material and physically adsorbed on the defects, they induce charge carrier transfer of sensor electrode and then the conductivity of active material changes. The ethanol molecules donate the electrons to the conduction band decreasing hole charge carriers, which lead to the resistance increase. Meanwhile, residual epoxy groups and the dopant of nitrogen atoms that are generated during thermal treatment act as electron-acceptors to combine with hydrogen atoms of

ethanol molecules establishing hydrogen bond. The hydrogen bonding promote the depletion of electrons at the active material and cause the resistance of PCNWL increased [144].

Real-time sensing of PCNWL-based gas sensor device was investigated with different concentration of ethanol vapor at ambient condition, as demonstrated in **Figure 24a**. PCNWL-based gas sensor electrode of four different conditions (PCNWL00, PCNWL31, PCNWL11, and PCNWL13) showed an increase of resistance immediately and reached to a saturated value by being exposed the ethanol vapor, the PCNWL-based sensor electrode As the flow of ethanol gas stopped, the resistance of electrodes return to primary value before exposure. **Figure 24b** displays the changes of sensitivity, which is the normalized resistance change, as the varying ethanol gas concentration for different condition of PCNWL-based sensor electrode. The sensitivity value is determined of the point when the normalized resistance change reached to saturation after 20 s. The PCNWL-based sensor device showed the linear behavior over a wide range of ethanol concentration, which means that ethanol sensing is reversible and reproducible. The sensitivity of PCNWL-based ethanol gas sensor mainly depended on the specific surface area of materials not the

conductivity. Because of the basic sensing mechanism, gas adsorption, the difference in sensing performance by specific surface area is greater than the effect of conductivity. In real-time sensing result, PCNWL11 and PCNWL31 showed more sensitive detection toward ethanol vapor than PCNWL00 because they have large surface area despite slightly lower conductivity. The PCNWL11 performed the highest sensitivity that the minimum detection level (MDL) of PCNWL11-based ethanol gas sensor is 20 ppb. Meanwhile, PCNWL13 showed lower sensitivity than PCNWL00 because of remarkably low conductivity due to excessive morphological modification.

For precise investigation of sensing performance, response and recovery time was measured, as manifested in **Figure 25a and b**. Generally, response time is evaluated as the time spent attaining 90% of saturated value and recovery time is estimated as the time spent achieving 10% of existing value before gas exposure. The response time of PCNWL-based sensor devices at 2 ppm of ethanol gas was calculated with 9, 9, 11, 13 s for PCNWL11, PCNWL31, PCNWL00, and PCNWL13, respectively. The measurement showed that the tendency of response time of PCNWLs followed the tendency of specific surface area. The response time became minutely shorter as the specific surface

increased. The enhanced surface area of the PCNWLs enabled more rapid adsorption time of gas and diffusion time of charge carriers to the layer. The result of recovery time evinced similar tendency with the response time. The recovery time of PCNWL-based sensor devices at 2 ppm of ethanol gas was computed with 62, 65, 67, 69 s for PCNWL11, PCNWL31, PCNWL00, and PCNWL13, respectively. Compared to response time, recovery time took longer time to come back before the exposure of ethanol molecules because detaching molecules needs external energy to break chemical bonding, mainly hydrogen bonding.

Outstanding cycle stability as well as reversible and reproducible ability is required to apply for sensor electrode material. The resistive changes of different condition of PCNWLs against periodic exposure to 2 ppm of ethanol gas were exhibited in **Figure 26a**. The sensitivity of all condition of sensor electrodes was maintained for equivalent value with progressing 4 times repetitively at ambient condition. In addition, PCNWL-based ethanol gas sensor electrode preserved their sensing ability toward 2 ppm of ethanol vapor during a month (>96%), as portrayed in **Figure 26b**. The PCNWLs were structurally stable during adsorption and desorption of ethanol gas, therefore the PCNWL-based ethanol gas sensor devices shows superior stability for repetitive sensing.

The selectivity test was also advanced to proof the applicability to actual industry. **Figure 27** reveals the sensitivity changes of PCNWL11 toward diverse VOCs (DMF, benzene, hexane, toluene, and acetone) at the concentration of 100 ppm and 2 ppm of ethanol. Even though lower concentration than other gases, ethanol performed about 8 times higher sensitivity. Therefore, PCNWL-based ethanol gas sensor devices has excellent selectivity among the various gases in nature.
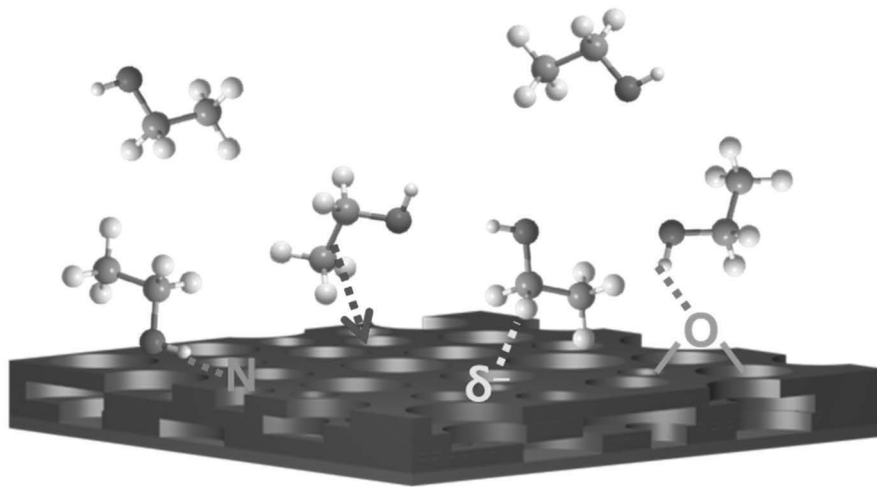
Figure 23. Schematic diagram of sensing mechanism of ethanol vapor. (red dotted line: hydrogen bond, yellow dotted line: van der Waals interaction, blue dotted line: adsorption)
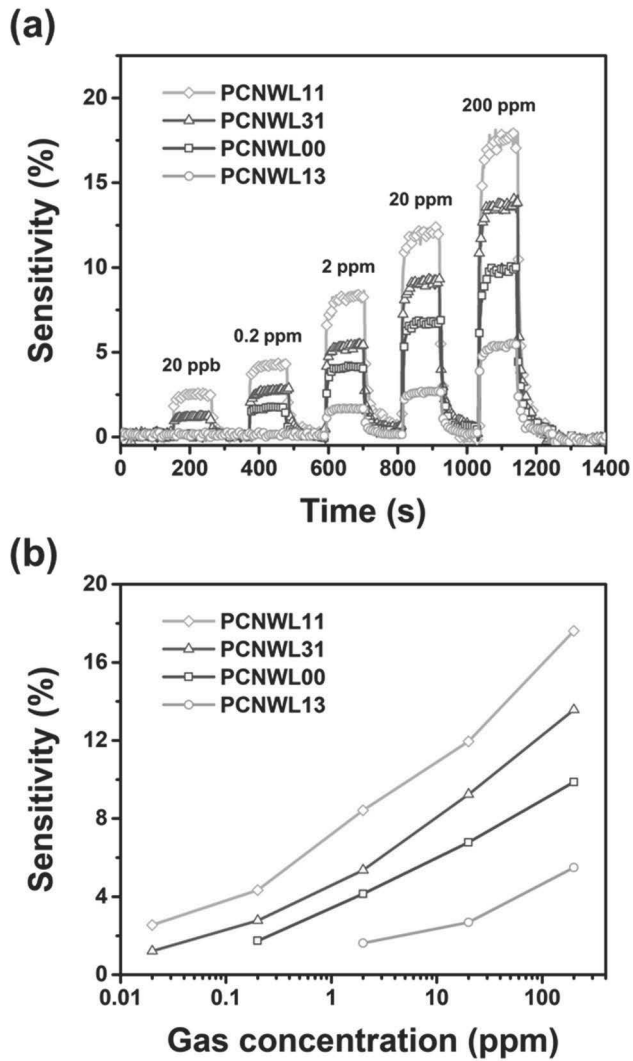
Figure 24. (a) Normalized resistance changes of ethanol gas sensors based on PCNWLs (PCNWL13, PCNWL00, PCNWL31, and PCNWL11) with sequential exposure to various concentrations of ethanol vapor. (b) Calibration curves as function of ethanol gas concentrations.
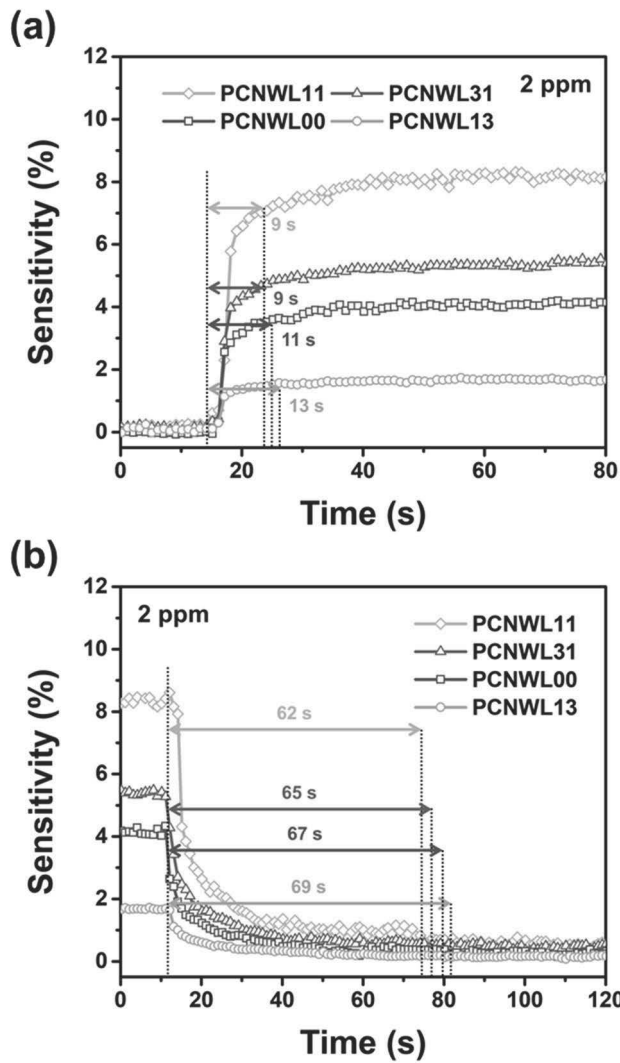
Figure 25. (a) Response and (b) recovery times of PCNWL-based ethanol gas sensors (using PCNWL13, PCNWL00, PCNWL31, and PCNWL11) toward 2 ppm of ethanol gas.
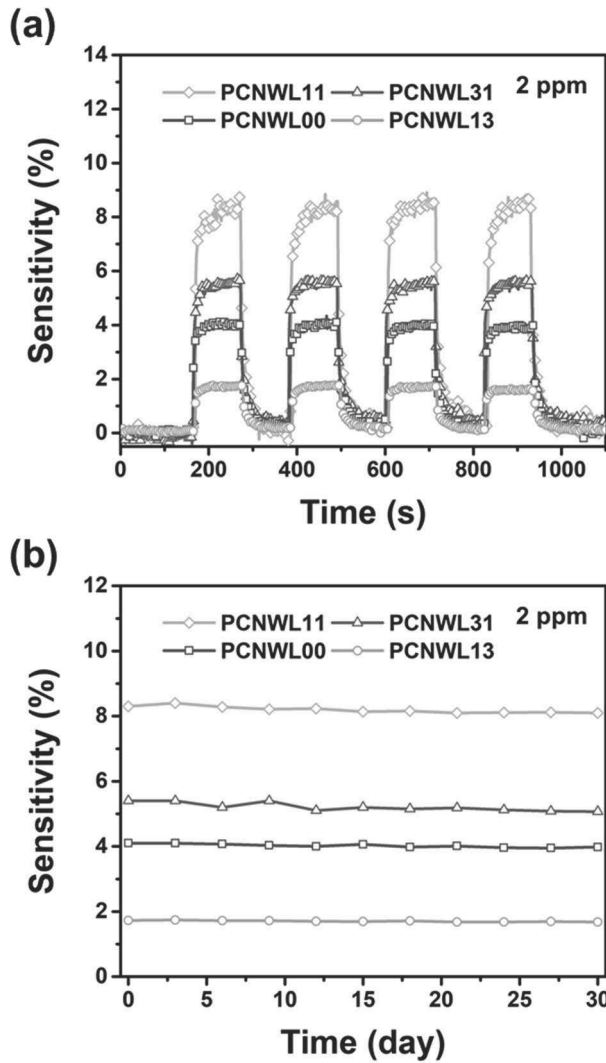
Figure 26. (a) Normalized resistance changes of ethanol gas sensors based on PCNWLs (PCNWL13, PCNWL00, PCNWL31, and PCNWL11) with 4 repeated exposure toward 2 ppm of ethanol gas. (b) Cycle stability test of PCNWL-based gas sensors with periodic exposure to 2 ppm of ethanol gas for a month.
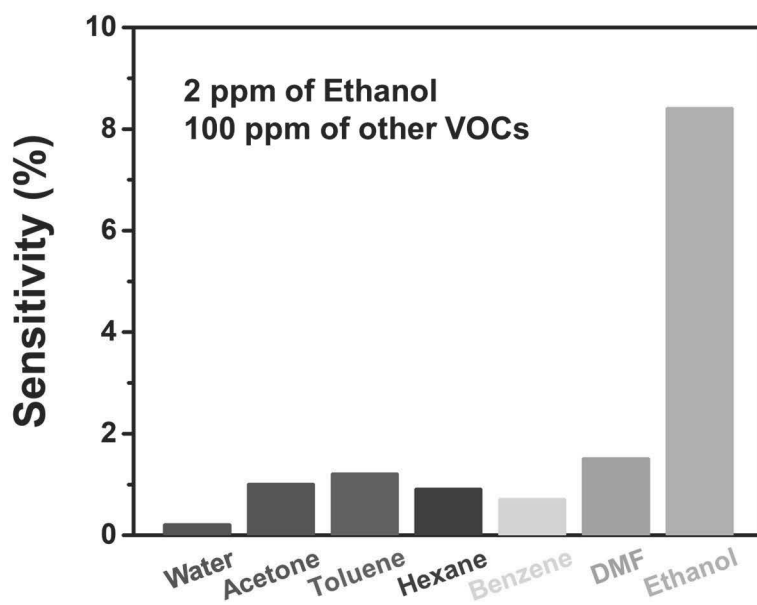
Figure 27. Selectivity test of PCWNL11-based gas sensor toward ethanol gas with various VOC gases (acetone, toluene, hexane, benzene, and DMF) and water.

3.2. Fluorination of porous carbon nanoweb layer for ammonia gas sensor: Heteroatom doping

3.2.1. Construction of fluorinated porous carbon nanoweb layers (FPCNWLs)

Fluorination of PCNWLs were improved *via* vacuum plasma treatment of fluorine-containing gas. The used PCNWL was the condition which 1:1 mixing ratio of PAN and PS, PCNWL11. The fluorination of PCNWL proceeded by 100 W of RF controller with octafluorocyclobutane (C_4F_8) gas at a flow rate of 15 sccm. In this experiment, the amount of loaded fluorine atom was controlled by treating time of plasma from 2 min to 80 min. During the plasma treatment under vacuum, cyclic structure of C_4F_8 gas molecules was broken into ionic species (CF^+, CF_2^+, CF_3^+, $C_2F_4^+$, and $C_3F_5^+$), as well as C–C and C=C bondings of PCNWL were broken making lots of defects [60,145]. Then, these ionic fragments were deposited on the defects of PCNWLs, forming various C–F bondings. Therefore, as the plasma treated time increases, the fluorine atoms in the carbon structure of PCNWL increased whereas the defects of carbon structure increased.

The FE-SEM image of FPCNWL that plasma treated during 20 min

(FPCNWL20) was displayed in **Figure 28**. There were no physical transformation or collapse after vacuum plasma treating of C_4F_8 gas.

To provide the fluorine atom doping in PCNWLs, EDS mapping of FPCNWL20 was carried out. As presented in **Figure 29**, the results revealed that the fluorine atoms were doped to the carbon structure clearly.
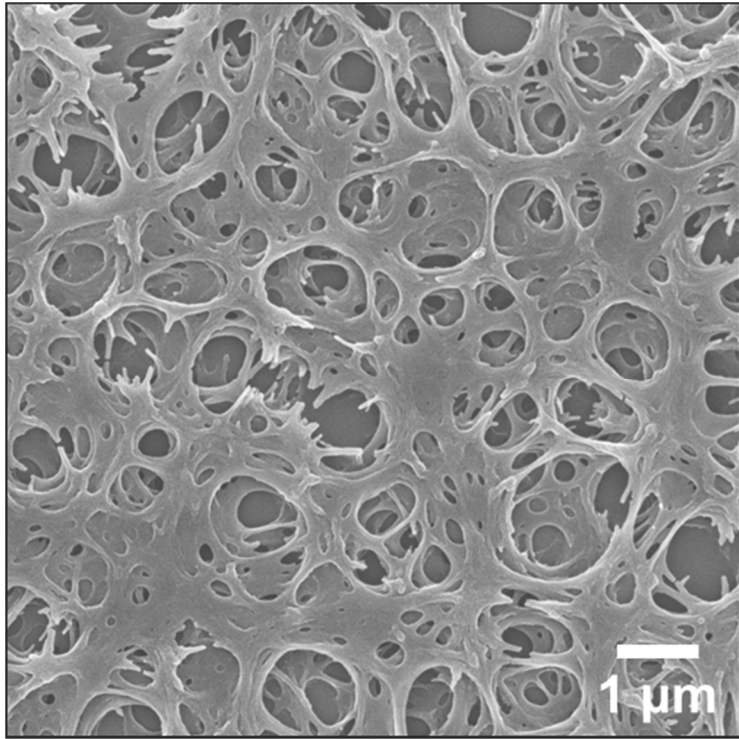
Figure 28. FE-SEM image of FPCNWL that plasma treated during 20 min (FPCNWL20).
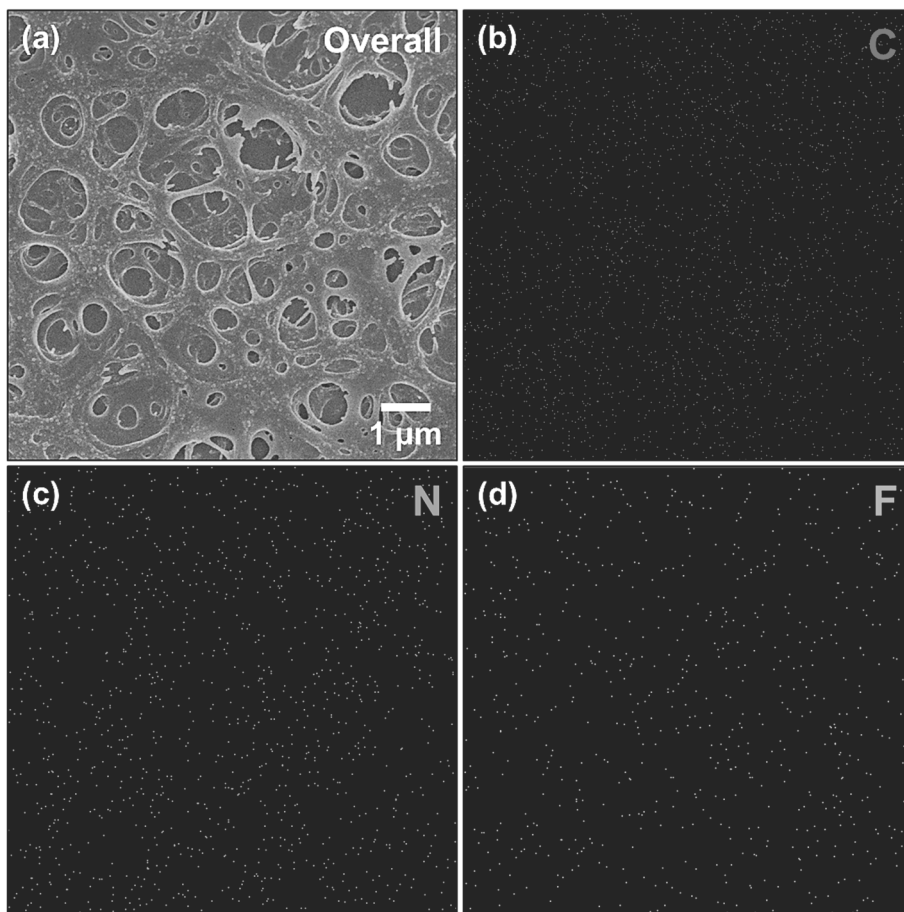
Figure 29. EDS elemental mapping images of FPCNWL20. (a) Overall image of all elements, (b) carbon, (c) nitrogen, and (d) fluorine atom mapping images.

3.2.2. Characterization of FPCNWLs

FT-IR analysis was achieved for the detailed study of chemical bonding changes during plasma treatment, as depicted in **Figure 30**. Compared with PCNWL11, FPCNWLs showed definite strong peaks of C–F, CF_2, and CF_3 stretching at 1067, 1227, and 1251 cm^{-1}, respectively. On the contrary, the carbon peaks of C=C bending, aromatic C=C stretching, C=C, and C=O stretching at 900–1000, 1400–1600, and 1650–1950 cm^{-1}, respectively, decreased or disappeared after plasma treatment. As a result of above, the plasma treatment generates the C–F ionic and covalent bondings as well as the defects of carbon based framework [146–147].

To further study of structural defects formed during vacuum plasma treatment, Raman spectra of each condition of FPCNWLs were obtained, as demonstrated in **Figure 31**. The I_D/I_G ratio of each samples was 1.39, 1.41, 1.42, 1.44, 1.46, 1.40, 1.41, and 1.43 for FPCNWL00, FPCNWL02, FPCNWL05, FPCNWL10, FPCNWL20, FPCNWL40, FPCNWL60, and FPCNWL80, respectively, as noted in **Table 3**. The I_D/I_G ratio increased as plasma treated time increased until 20 min, and then, the I_D/I_G ratio decreased rapidly and increased again. As the fluorine plasma treated onto the PCNWLs, the defects of carbon structure increased due

82

to the high plasma energy and the fluorine atoms were doped concurrently. The F atoms, ionic CF_x, ionic C_2F_4 and C_3F_5, and covalent C–F bonding species are doped into the defects of carbon structure during plasma treatment, filling up the defects. Meanwhile, during filling up the defects, divisional ionic C_2F_4 and C_3F_5 formed additional hexagonal-like structure with other carbon defects. After 40 min of plasma treating time, this effect became stronger, therefore, the I_D/I_G ratio decreased rapidly. Then, plasma treated continuously for a long time, the structures formed in such a way also collapsed to be defects.

For the examination for elemental study and chemical combinations of FPCNWLs, XPS analysis was investigated. **Figure 32** portrayed the high-resolution spectra of C 1s of FPCNWLs. Before the plasma treatment, FPCNWL00, only C=C, C–N, and C=O peaks were found in the result. (**Figure 32a**) Progressing the F plasma doping, **Figure 32b–h**, fluorine-related CF_x peaks of –CF, $-CF_2$, $-CF_3$, and C–CF_x peak at 287–294 eV increased gradually [148]. Moreover, the intensity of main carbon peak C=C at 284.6 eV progressively decreased compared to FPCNWL00. Even after 40 min, the intensity of C=C peak was similar with other C–N, C=O, and F-related peaks. The atomic ratios of C, N, F were noted at **Table 4** as 80.0, 7.57, 12.43% for FPCNWL02, 70.01, 7.26,

22.73% for FPCNWL05, 63.73, 6.99, 29.28% for FPCNWL10, 54.7, 6.78, 38.52% for FPCNWL20, 48.34, 6.23, 45.42% for FPCNWL40, 45.44, 6.59, 47.97% for FPCNWL60, and 45.18, 6.86, 47.96% for FPCNWL80, respectively. Actually, the elemental ratio of carbon was diminished steadily, while the proportion of fluorine was enhanced as the plasma treated time went by until 60 min. After that, the distribution ratio of FPCNWL hardly changed.
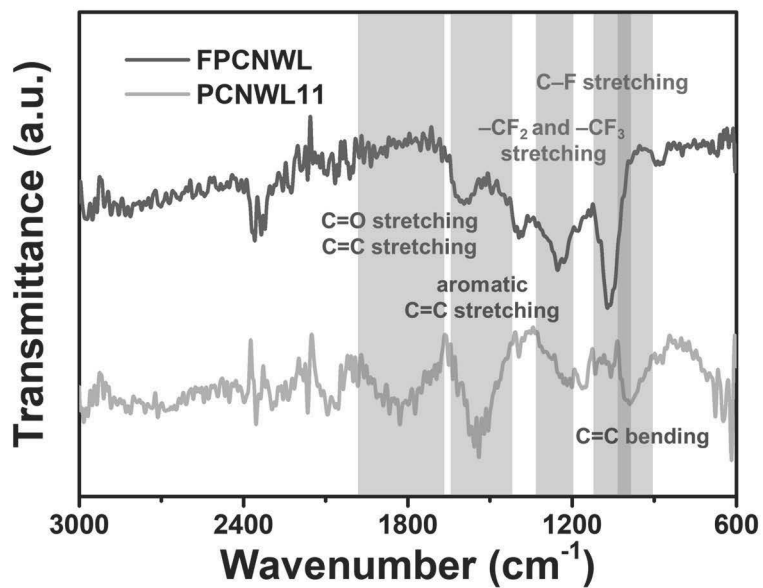
Figure 30. FT-IR spectra of PCNWL11 and FPCNWLs.
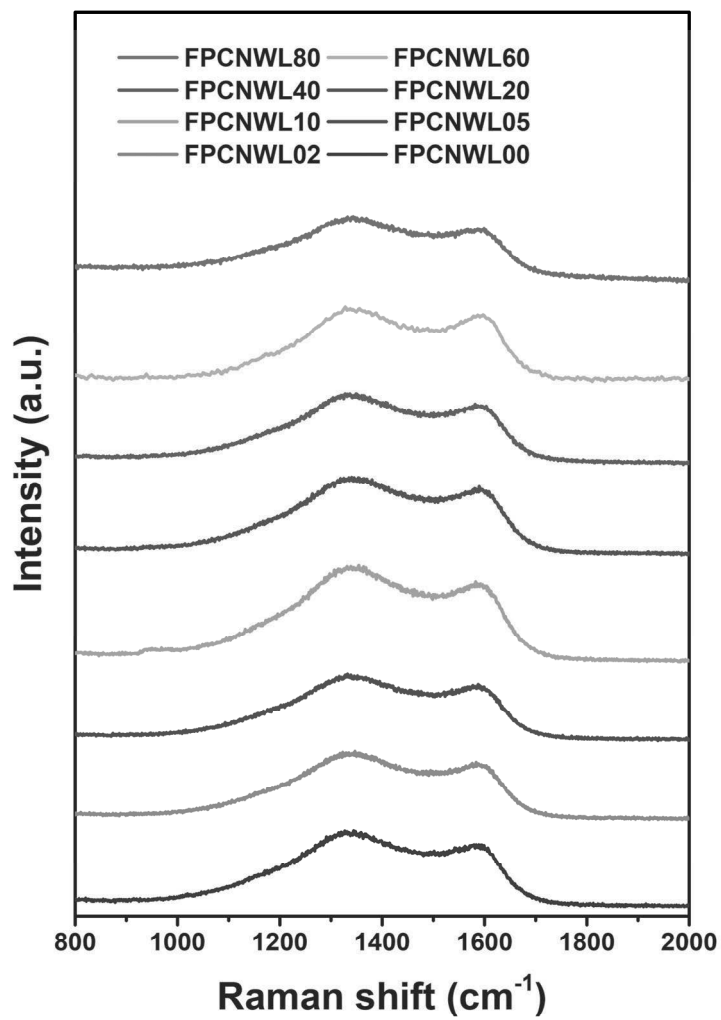
Figure 31. Raman spectra of FPCNWLs (FPCNWL00, FPCNWL02, FPCNWL05, FPCNWL10, FPCNWL20, FPCNWL40, FPCNWL60, and FPCNWL80).

Table 3. The I_D/I_G ratio of FPCNWLs calculated from Raman spectra.

Sample	I_D/I_G
FPCNWL00	1.39
FPCNWL02	1.41
FPCNWL05	1.42
FPCNWL10	1.44
FPCNWL20	1.46
FPCNWL40	1.40
FPCNWL60	1.41
FPCNWL80	1.43
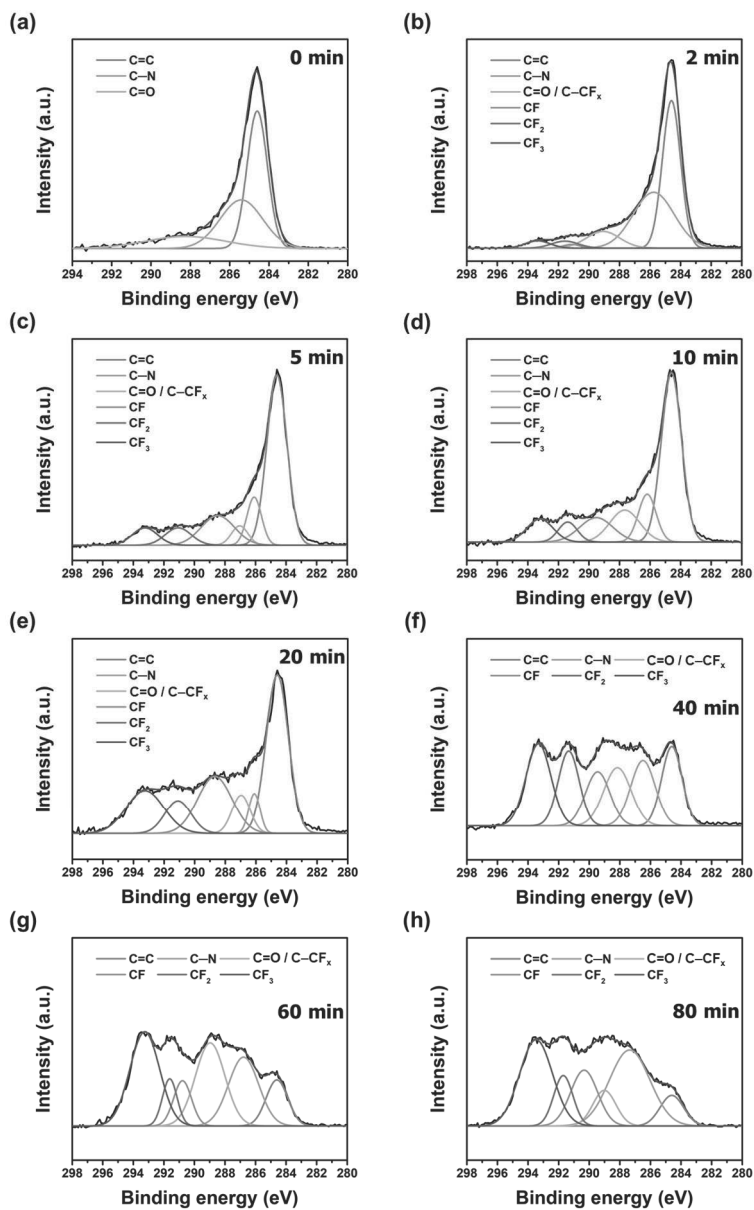
Figure 32. XPS analysis of FPCNWLs with different plasma treating time for (a) 0 min, (b) 2 min, (c) 5 min, (d) 10 min, (e) 20 min, (f) 40 min, (g) 60 min, and (h) 80 min.

Table 4. Elemental composition ratio of FPCNWLs obtained by XPS analysis.

Sample	C (At%)	N (At%)	F (At%)
FPCNWL02	80.0	7.57	12.43
FPCNWL05	70.01	7.26	22.73
FPCNWL10	63.73	6.99	29.28
FPCNWL20	54.7	6.78	38.52
FPCNWL40	48.34	6.23	45.42
FPCNWL60	45.44	6.59	47.97
FPCNWL80	45.18	6.86	47.96

3.2.3. Electrical properties of ammonia gas sensor electrode based on FPCNWLs

The electrical conductivity of FPCNWLs was appraised using 4-point probe method. As shown in **Figure 33**, the electrical conductivity was calculated of 6.918 S cm^{-1} for FPCNWL00, 6.32 S cm^{-1} for FPCNWL02, 4.68 S cm^{-1} for FPCNWL05, 4.57 S cm^{-1} for FPCNWL10, 4.13 S cm^{-1} for FPCNWL20, 3.12 S cm^{-1} for FPCNWL40, 3.01 S cm^{-1} for FPCNWL60, and 2.24 S cm^{-1} for FPCNWL80, respectively. The conductivity was reduced as the plasma treated time was prolonged increasing defects. Moreover, the electrical conductivity was dropped relatively sharply as the plasma treatment time goes from 2 to 5 minutes, from 20 to 40 minutes, and from 60 to 80 minutes. Although, in Raman spectra, the I_D/I_G ratio increased after 40 min of plasma treatment, the conductivity of FPCNWLs were declined steadily. The graphitic structure generated with C–CF$_x$ ionic and covalent bonding do not affect increasing conductivity.

The FPCNWL-based ammonia gas sensor electrodes were constructed with thermal deposition of gold pattern array. **Figure 34a** displays a digital image of the FPCNWL-based ammonia gas sensor electrode. The gold pattern array was clearly deposited on the center of FPCNWL. The

current–voltage (*I–V*) curves were obtained to estimate the electrical contact of the FPCNWLs and the gold electrode array, as depicted in **Figure 34b**. The curves showed linear shapes for the voltage range from −1.0 V to 1.0 V, indicating that the FPCNWLs have an Ohmic contact with the gold array. The contact resistance (*dV/dI*, a reciprocal of the slope) increased with the F plasma treated time increased because the decreased conductivity of FPCNWLs affected the contact resistance between FPCNWLs and gold pattern array.
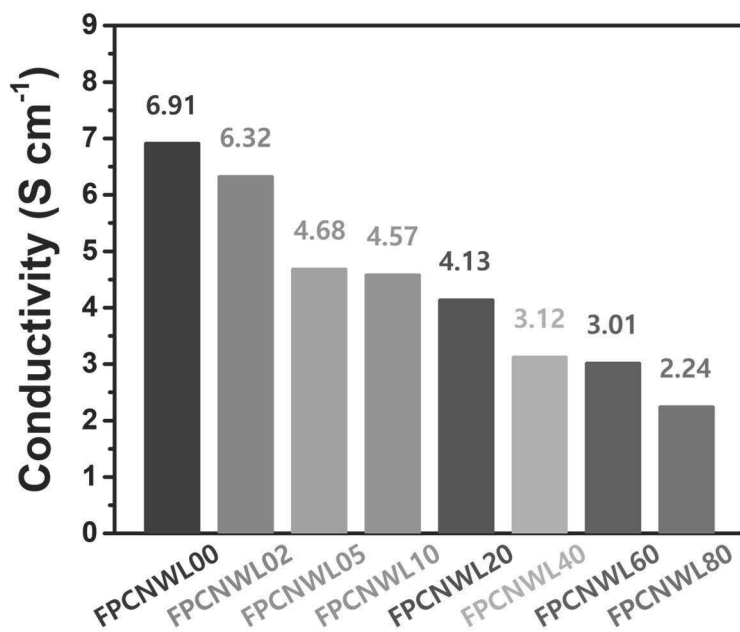
Figure 33. Electrical conductivities of each conditions of FPCNWLs.
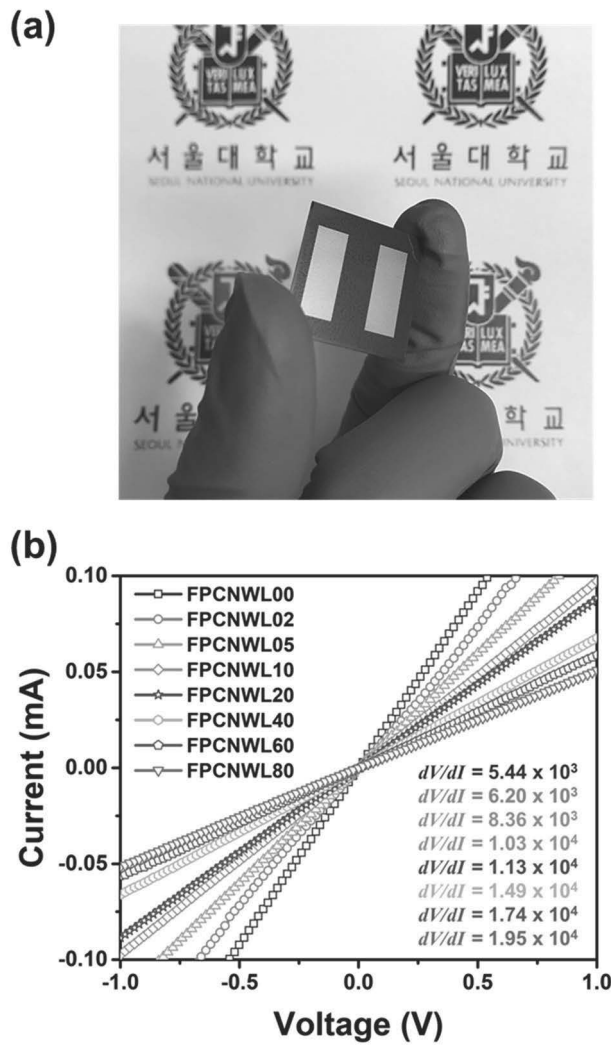
Figure 34. (a) Digital image of the FPCNWL-based gas sensor electrode.
(b) *I–V* curves of each conditions of FPCNWLs at the voltage range from
–1.0 V to 1.0 V.

3.2.4. Real-time sensing performance of FPCNWL-based ammonia gas sensor

Commonly, gas molecules are adsorbed on the defects of hexagonal structure, end of functional groups, and heteroatoms that are doped at carbon materials. In this FPCNWL-based sensor system, ammonia gas is physisorbed on the defects, the nitrogen, and fluorine atoms in the carbon structure due to van der Waals interaction and hydrogen bond. When the ammonia molecules are exposed to sensing material and are adsorbed, they donate the electrons to the conduction band of FPCNWLs causing charge carrier (hole) reduction by recombination since the FPCNWLs are *p*-type material, which lead to the resistance increase. In addition to these basic mechanisms, the fluorine doping provoked the supplementary effect of ammonia gas sensing, as delineated in **Figure 35a and b**. Basically, fluorine is one of *p*-type dopant extracting the electrons from the carbon materials due to its high electronegativity, therefore, causing decrease of electrons in the carbon materials. Hence, fluorine doping brings about strong *p*-type doping effect in carbon material. Furthermore, fluorine doping also brings about enhancement of the physisorption ability toward ammonia gas because of lone pair of fluorine atoms. When the ammonia molecules are adsorbed onto the

FPCNWLs, the *p*-type doping effect decrease, as well as the delocalization of the electrons is broken due to the lone pairs of nitrogen atoms in ammonia molecules. Then, the distinct electron cloud due to broken delocalization of FPCNWLs after ammonia gas adsorption causes increasing the resistance [149].

Real-time sensing of FPCNWL-based gas sensor device was examined with different concentration of ammonia gas at ambient condition, as presented in **Figure 36a**. The sensing proceeded with five different conditions (FPCNWL00, FPCNWL05, FPCNWL20, FPCNWL40, and FPCNWL80). Being exposed the ammonia gas, the FPCNWL-based sensor electrode performed an increase of resistance rapidly and reached to a saturated value. As the electrode was shut off from the ammonia gas, the resistance of electrodes return to primary value before exposure. **Figure 36b** shows the change of the normalized resistance change, sensitivity, with the varying ammonia gas concentration for different condition of FPCNWL-based sensor electrode. The sensitivity value is determined of the point when the normalized resistance change reached to saturation after 20 s. The FPCNWL-based sensor device revealed the linear behavior over a wide range of ammonia concentration in log scale, which means the reversible

and reproducible properties. The sensitivity of FPCNWL-based ammonia gas sensor depended on both conductivity and fluorination rate. The sensor electrode with FPCNWL05, FPCNWL20, and FPCNWL40 demonstrated more sensitive detection toward ammonia gas than FPCNWL00 because of their fluorination. Fluorine and nitrogen doped carbon lattice has more charge carriers and more intimacy with NH_3 gas, as mentioned previously. The FPCNWL20 performed the highest sensitivity, which the MDL of FPCNWL20-based ethanol gas sensor is 9 ppb. The plasma treatment for 20 minutes disclosed the most appropriate condition between the conductivity drop and fluorination effect (charge carrier increment, breaking the delocalization, and ammonia intimacy). Meanwhile, FPCNWL80 was appeared lower sensitivity than other samples even FPCNWL00, which is no plasma treated. The effect of conductivity drop becomes more stronger than that of fluorination of FPCNWL80, therefore the sensitivity of FPCNWL80 has the poorest performance.

For accurate study of sensing performance, response and recovery time were measured, as exhibited in **Figure 37a and b**. Typically, response time is calculated as the time spent reaching 90% of saturated value and recovery time is evaluated as the time spent arriving 10% of

existing value before gas exposure. The response time of FPCNWL-based sensor devices at 0.9 ppm toward ammonia gas was calculated with 11, 18, 21, 21, 26 s for FPCNWL20, FPCNWL05, FPCNWL40, FPCNWL00, and FPCNWL80, respectively. The fluorination rate and conductivity directly affect the response time. The result of recovery time evinced similar tendency with the response time. The recovery time of FPCNWL-based sensor devices at 2 ppm to ammonia gas was computed with 51, 62, 67, 70, 74 s for FPCNWL20, FPCNWL05, FPCNWL40, FPCNWL00, and FPCNWL80, respectively. Compared to response time, recovery time took longer to return before the exposure of ammonia molecules because detaching molecules needs external energy to break chemical bonding (hydrogen bond).

To apply for sensor electrode material, superior cycle stability as well as reversible and reproducible ability is required. The resistive changes of different condition of FPCNWLs against periodic exposure to 0.9 ppm of ammonia gas were noticed in **Figure 38a**. The sensitivity of all condition of sensor electrodes was sustained for similar value with proceeding 4 times repetitively at ambient condition. In addition, FPCNWL-based NH_3 gas sensor electrode preserved their sensing ability toward 0.9 ppm of ammonia gas during a month (>95%), as manifested

97

in **Figure 38b**. The FPCNWLs were structurally stable during adsorption and desorption of NH_3 gas, therefore the FPCNWL-based ammonia gas sensor devices demonstrate outstanding stability for repetitive sensing.

The selectivity test also progressed to proof the applicability to actual industry. **Figure 39** discloses the sensitivity changes of FPCNWL20-based sensor device toward diverse VOCs (DMF, benzene, hexane, toluene, and acetone) at the concentration of 100 ppm and 0.9 ppm of ammonia gas. Even though lower concentration than other gases, NH_3 gas performed *ca.* 9 times higher sensitivity. Therefore, FPCNWL-based NH_3 gas sensor devices has outstanding selectivity among the various gases in nature.
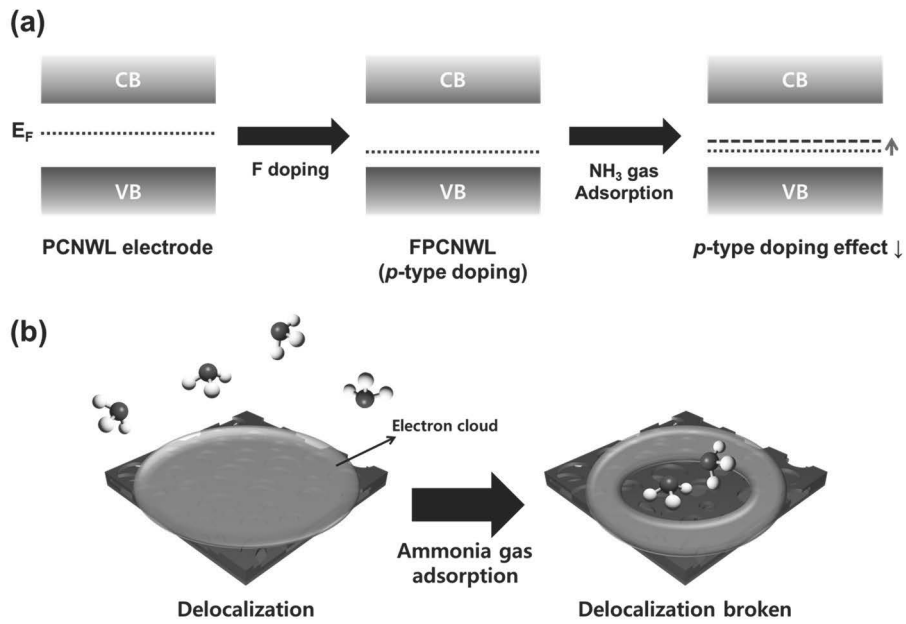
Figure 35. Schematic diagram of sensing mechanism of FPCNWL-based ammonia gas sensor.
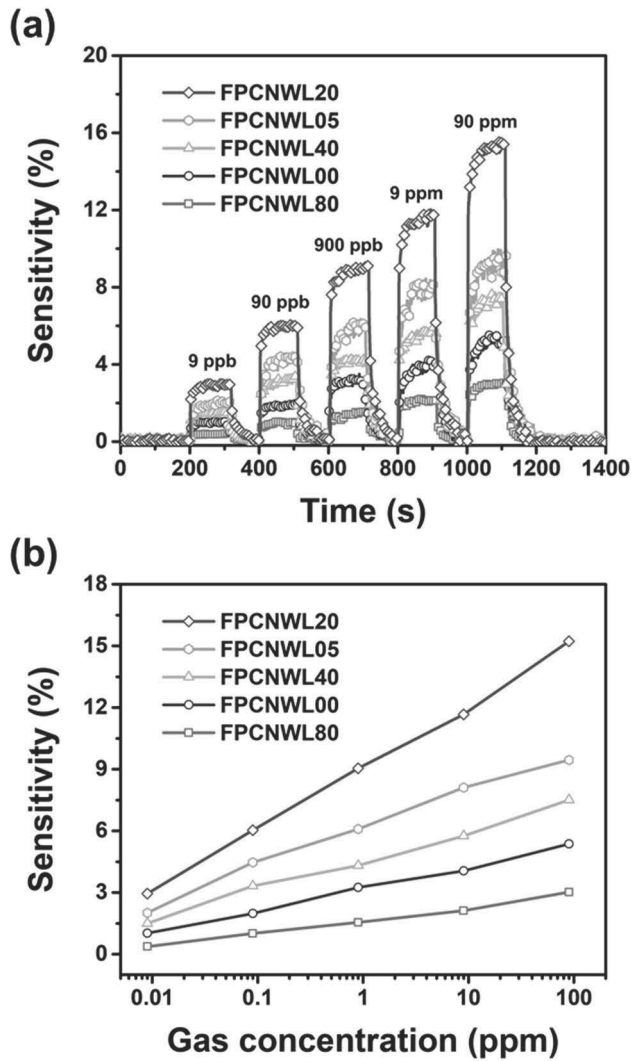
Figure 36. (a) Normalized resistance changes of NH_3 gas sensors based on FPCNWLs (FPCNWL00, FPCNWL05, FPCNWL20, FPCNWL40, and FPCNWL80) with sequential exposure to various concentrations of ammonia gas. (b) Calibration curves as function of ammonia gas concentrations.
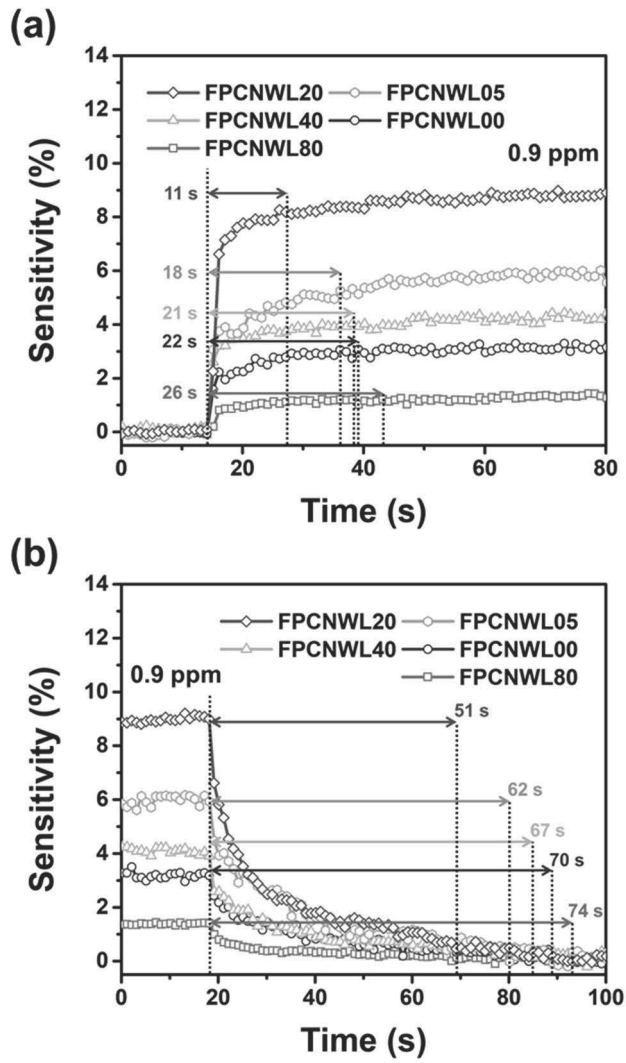
Figure 37. (a) Response and (b) recovery times of FPCNWL-based ammonia gas sensors (using FPCNWL 00, FPCNWL05, FPCNWL20, FPCNWL40, and FPCNWL80) toward 0.9 ppm of ammonia gas.
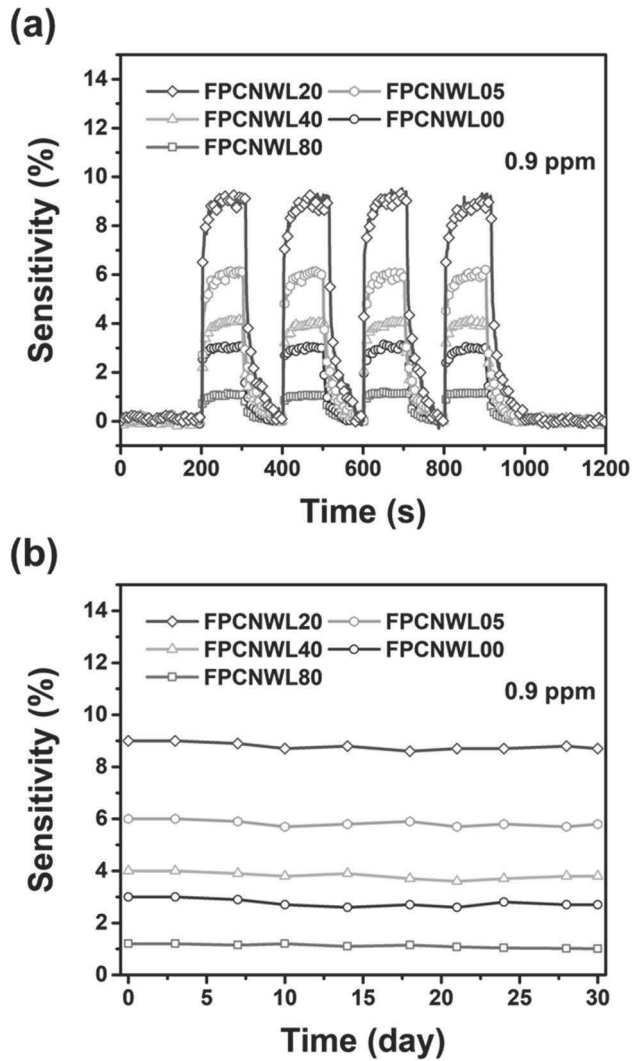
Figure 38. (a) Normalized resistance changes of NH₃ gas sensors based on FPCNWLs (FPCNWL 00, FPCNWL05, FPCNWL20, FPCNWL40, and FPCNWL80) with 4 repeated exposure toward 0.9 ppm of ammonia gas. (b) Cycle stability test of FPCNWL-based gas sensors with periodic exposure to 0.9 ppm of ammonia gas for a month.
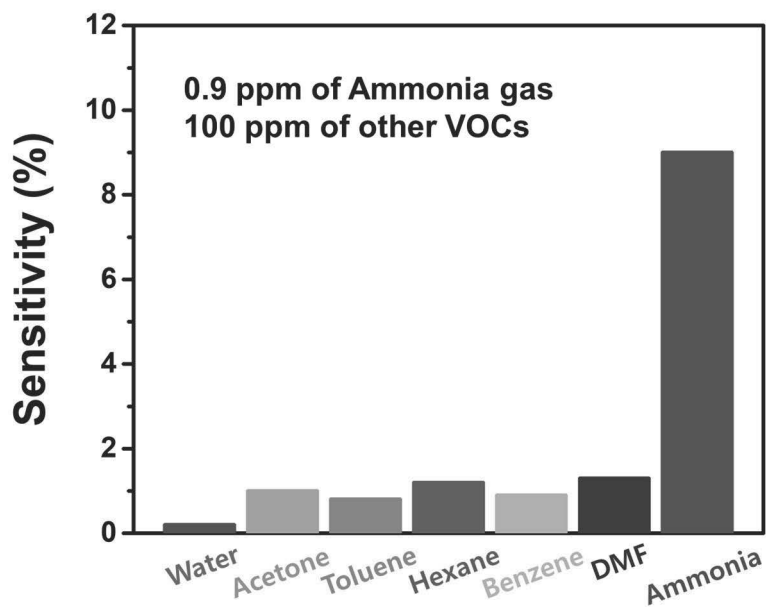
Figure 39. Selectivity test of FPCWNL20-based gas sensor toward ammonia gas with various VOC gases (acetone, toluene, hexane, benzene, and DMF) and water.

3.3. Platinum villus overlaid porous carbon nanoweb layer for hydrogen gas sensor: Metal introduction

3.3.1. Construction of platinum villus overlaid porous carbon nanoweb layers (PtPCNWLs)

PtPCNWLs were manufactured *via* electrochemical deposition of platinum nanostructure on the PCNWLs, as illustrated in **Figure 40**. Platinum villus nanostructure was fabricated with the electrochemical deposition under acidic aqueous solution containing Pt precursor with Ag/AgCl reference electrode, Pt counter electrode, and PCNWL11, which condition is 1:1 mixing ratio of PAN and PS, for working electrode.

The shape of Pt structure was controlled with varying the deposition voltage and the platinum precursor concentration. **Figure 41** displays the FE-SEM images for the shape distinction of Pt nanostructure on PtPCNWLs fabricated by different deposition voltage from –0.5 to –2.0 V with 1 mM of Pt precursor. As the absolute value of voltage increased, the size of Pt villus increased. Actually, at the low voltage, platinum nanostructure formed like particle shape in small size (*ca.* 20–30 nm). As the voltage increased negatively, the Pt structure changed from particle shape to elliptical villus shape (*ca.* 80 nm long). At the

negatively high voltage, the Pt particle grows only in one direction causing elongated shape.

The growth mechanism of Pt villus structure is schematically illustrated in **Figure 42**. Initially, platinum ions are attached on the surface of PCNWL11, generating Pt seeds by the nucleation process. The reduction reaction advanced continuously nearby the existing Pt seeds. During the reduction reaction, the seeds normally tend to grow in the radial direction. However, when applied at negatively high voltage, the platinum seeds are not radial, but tend to grow in either direction. The negatively high voltage induces the Pt ions to easily incorporate into the existing large cluster contributing to growth, like Ostwald ripening phenomenon. The larger particles tend to grow at the expense of the smaller ones because of their desire to minimize the surface free energy. As a result, elongated villus shape Pt structures were deposited on the carbon layer surface [150–153].

The FE-SEM images of PtPCNWLs electrochemically deposited at the voltage of –2.0 V with different platinum precursor concentration from 0.1 to 5 mM of $PtCl_4$ was exhibited in **Figure 43**. Compared to the condition of 1 mM $PtCl_4$, at lower precursor concentration of 0.1 mM, Pt villus structures were electrochemically deposited on the PCNWL11

with very small size (*ca.* 10–20 nm) due to lack of Pt source. Whereas, at high concentration of precursor of 5 mM, Pt villus structure grew irregularly and excessively (*ca.* 50–130 nm) because of too high concentration of platinum ion. According to the above two experiments varying conditions, the Pt villus structure prepared at –2.0 V at the concentration of 1 mM platinum precursor was considered to be the best condition of fabricating uniform size of villus shape.

To further study for existing elements of PtPCNWLs, EDS elemental mapping were carried out, as depicted in **Figure 44**. According to the images, the platinum villus structures were obviously deposited on N doped carbon nanoweb layer.
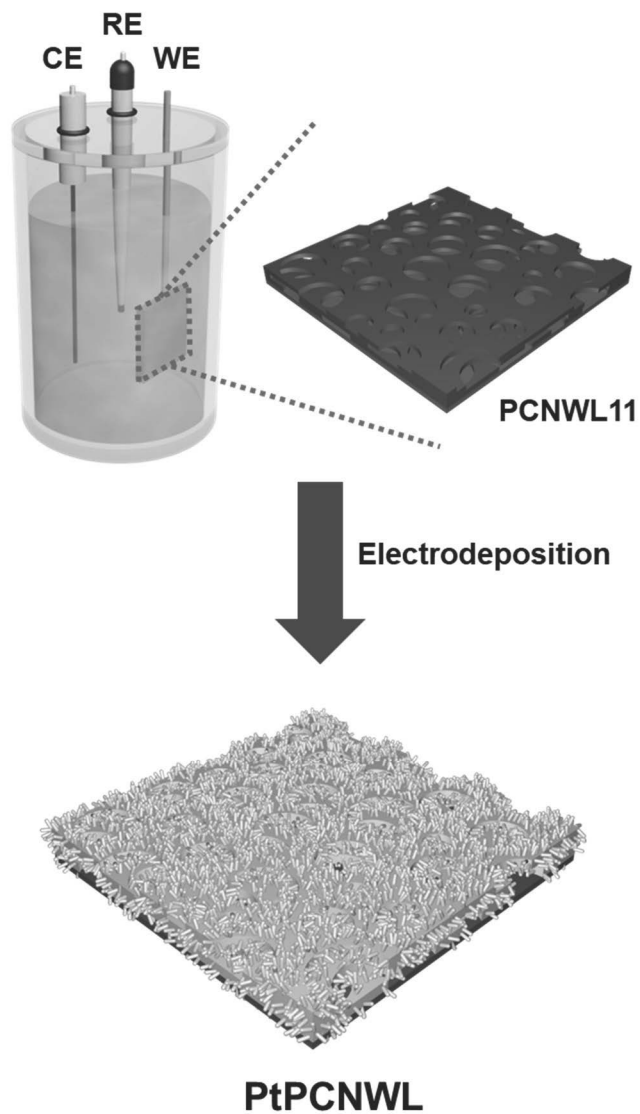
Figure 40. Schematic representation of overall procedure of fabricating PtPCNWLs
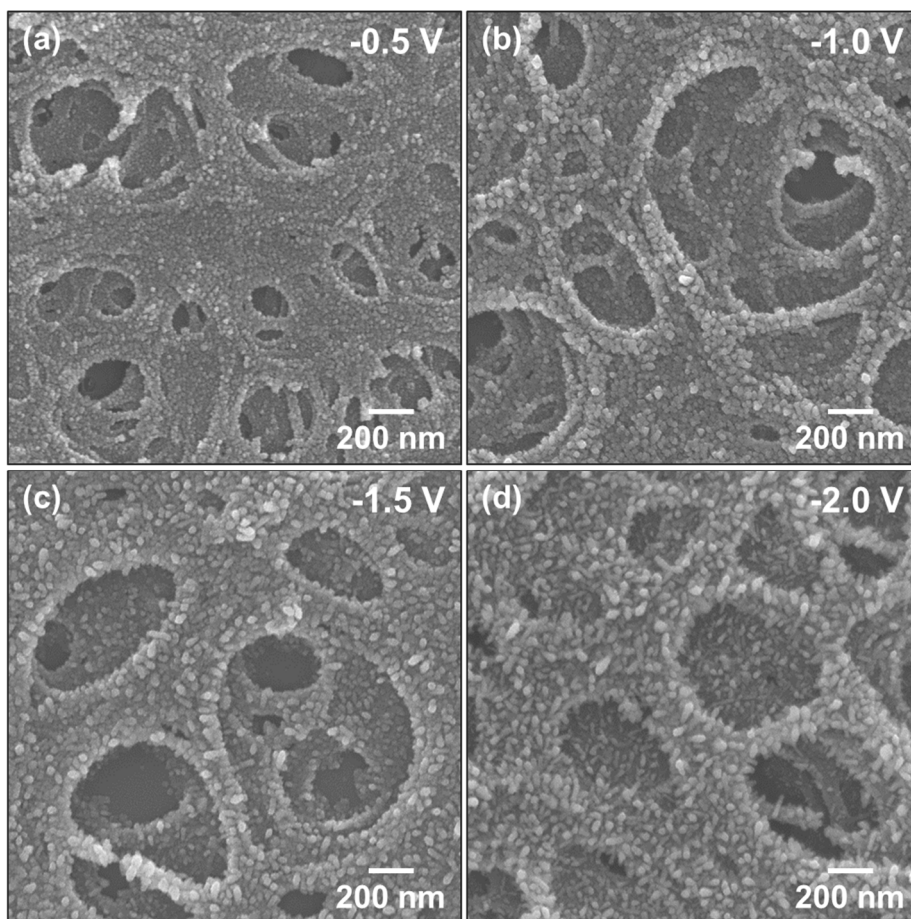
Figure 41. FE-SEM images of PtPCNWLs with varying deposition voltage from –0.5 to –2.0 V using 1 mM of Pt precursor (PtCl$_4$).
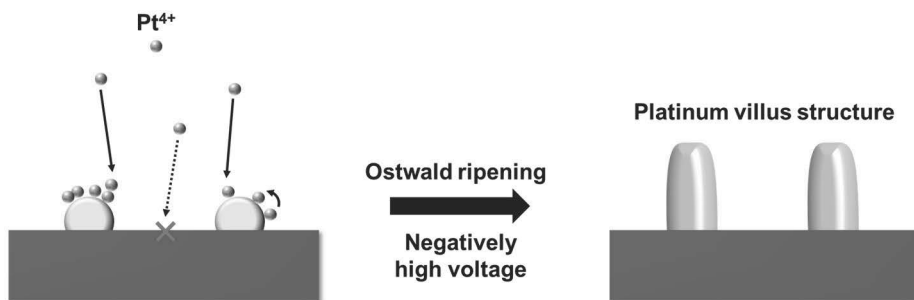
Figure 42. Schematic illustration of the growth mechanism of Pt villus structure.
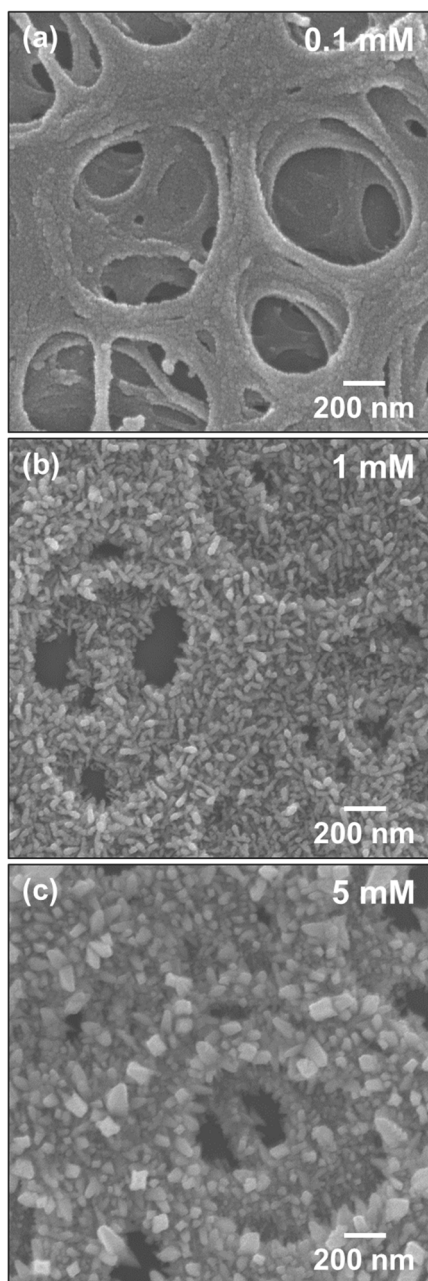
Figure 43. FE-SEM images of PtPCNWLs with different concentrations of Pt precursor from 0.1 to 5 mM deposited at –2.0 V.
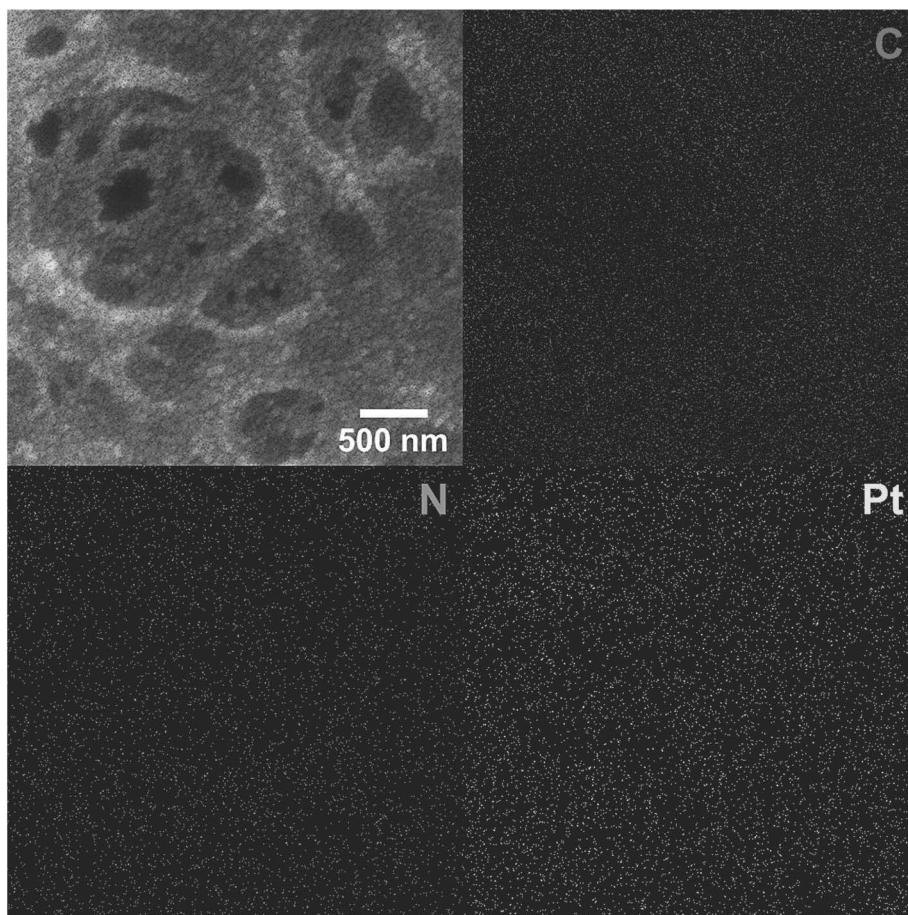
Figure 44. EDS elemental mapping images of PtPCNWLs. (a) Overall image of all elements, (b) carbon (red), (c) nitrogen (green), and (d) platinum (yellow).

3.3.2. Characterization of PtPCNWLs

For the investigation for elemental analysis and chemical combinations of PtPCNWLs, XPS analysis was carried out. **Figure 45** delineateed the high-resolution spectra of C 1s and Pt 4f of PtPCNWLs. The elemental ratio of C, N, Pt were 91.61, 5.17, 3.24% for PtPCNWL0.1, 73.77, 6.37, 19.87% for PtPCNWL1, and 64.01, 8.67, 27.32% for PtPCNWL5, respectively, as noted in **Table 5**. Explicitly, the Pt portion in PtPCNWLs increased as the concentration of platinum precursor increased. In **Figure 45b, d, and f**, Pt peaks were deconvoluted into 6 different peaks of $4f_{5/2}$ and $4f_{7/2}$ for Pt^0, Pt^{2+}, and Pt^{4+}, respectively. As the concentration of platinum precursor increased, the intensity of Pt peaks increased. Furthermore, all Pt peaks, especially the Pt^{4+} peaks of $4f_{5/2}$ and $4f_{7/2}$, were shifted to left (toward high binding energy), as the concentration of Pt precursor decreased, which means the partial oxidation of platinum atoms. Furthermore, the spin-orbit component of $4f_{7/2}$ and $4f_{5/2}$ were observed at around 70.9 and 74.2 eV, respectively, indicating the valence state of Pt is metallic Pt (0) [154–156].

To examine the crystallinity of platinum structure and the chain packing of the carbon lattice, X-ray diffraction (XRD) analysis was investigated, as presented in **Figure 46**. The broad peak in the region

15º<2θ<35º is the typical amorphous peak of carbon lattice, which can likely be attributed to the π–π interaction of the carbon chains. Compared to PCNWL11, PtPCNWLs revealed diffraction peaks at 2θ= 39.9, 46.5, 81.6, and 86.1º correspond to (111), (200), (311), and (222) planes of face-centered-cubic (fcc) crystalline phase of Pt (JCPDS 00-004-08002), respectively. As expected, the XRD peak intensities of Pt planes increased with the used platinum precursor increased from 0.1 to 5 mM because of enhancement in Pt villus structure size and density [97].
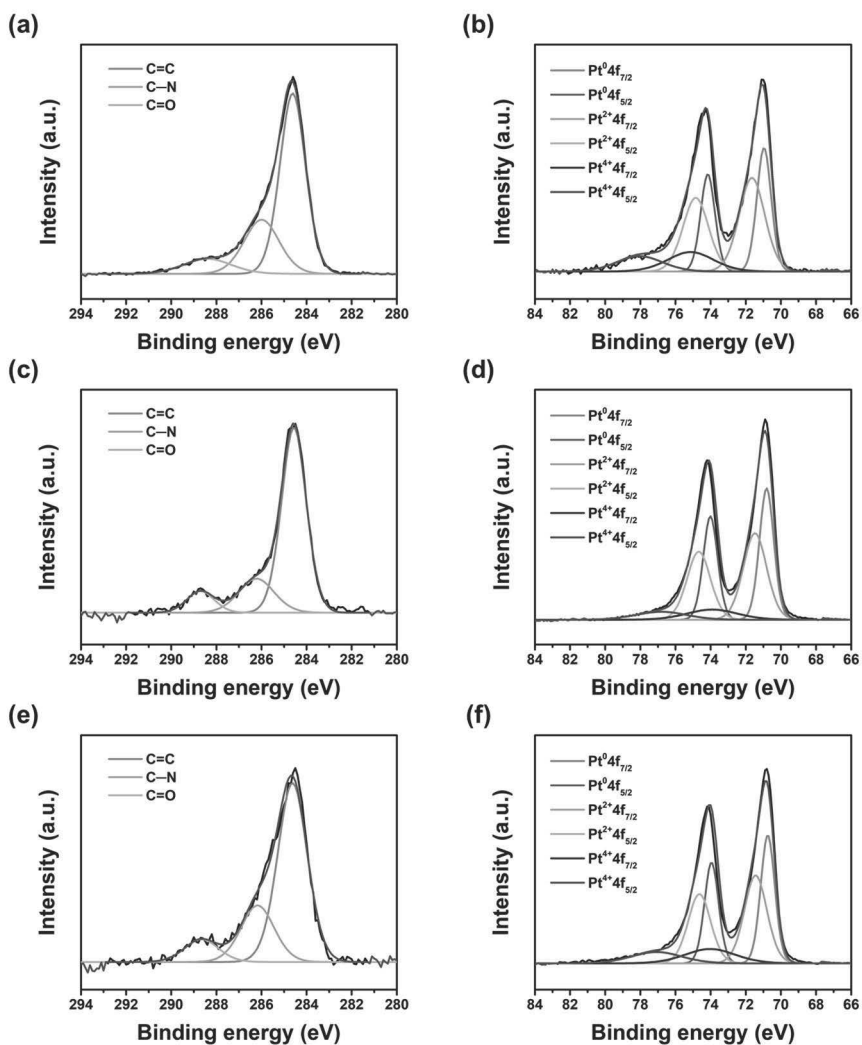
Figure 45. High-resolution C 1s ((a),(c), and (e)) and Pt 4f ((b), (d), and (f)) XPS spectra of PtPCNWLs with different concentrations of Pt precursor 0.1 mM for (a) and (b), 1 mM for (c) and (d), 5 mM for (e) and (f).

Table 5. Elemental composition ratio of PtPCNWLs obtained by XPS analysis.

Sample	C (At%)	N (At%)	Pt (At%)
PtPCNWL0.1	91.61	5.17	3.24
PtPCNWL1	73.77	6.37	19.89
PtPCNWL5	64.01	8.67	27.32
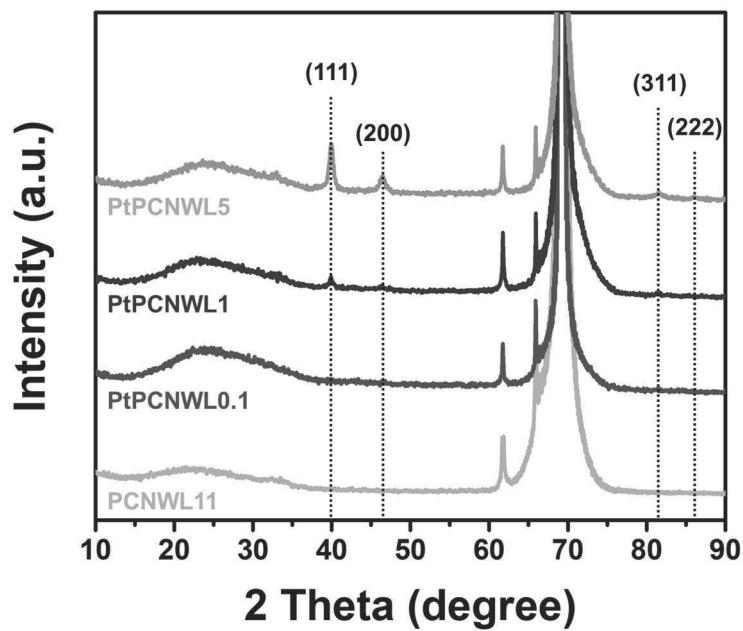
Figure 46. XRD spectra of PCNWL11 and PtPCNWLs (PtPCNWL0.1, PtPCNWL1, and PtPCNWL5).

3.3.3. Electrical properties of hydrogen gas sensor electrode based on PtPCNWLs

The electrical conductivity of PtPCNWLs was measured using 4-point probe method. As revealed in **Figure 47**, the electrical conductivity was evaluated of 11.54 S cm^{-1} for PtPCNWL0.1, 92.71 S cm^{-1} for PtPCNWL1, and 332.63 S cm^{-1} for PtPCNWL5, respectively. The absolute quantity of electrochemically deposited platinum structure increased as the concentration of Pt precursor increased, which made the conductivity increased.

The PtPCNWL-based hydrogen gas sensor electrodes were fabricated with thermal deposition of gold pattern array. **Figure 48a** shows a digital image of the PtPCNWL-based hydrogen gas sensor electrode. The gold pattern array was definitely deposited on the center of PtPCNWL.

The current–voltage (*I–V*) curves were appraised to estimate the electrical contact between the PtPCNWLs and the gold pattern array, as displayed in **Figure 48b**. The curves expressed linear shapes for the voltage range from −0.1 to 0.1 V, indicating that the PtPCNWLs have an Ohmic contact with the gold pattern array. The contact resistance (*dV/dI*, a reciprocal of the slope) decreased with the concentration of used Pt precursor increased because of their own conductivity.
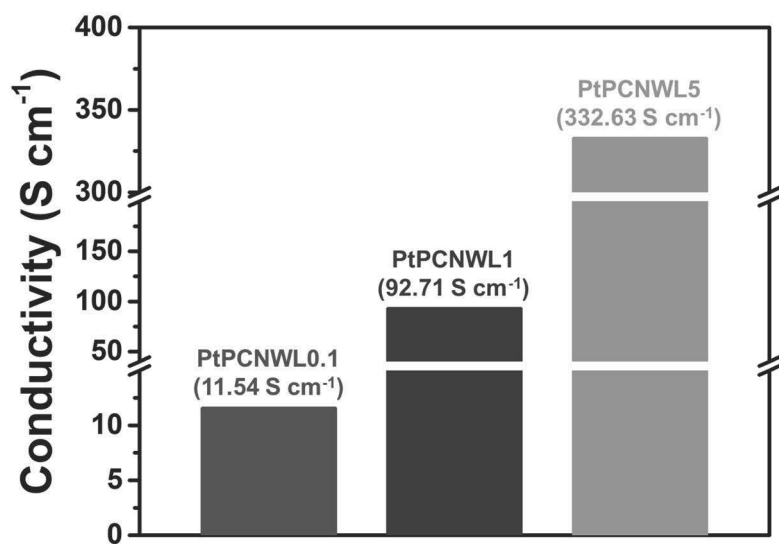
Figure 47. Electrical conductivities of each conditions of PtPCNWLs.
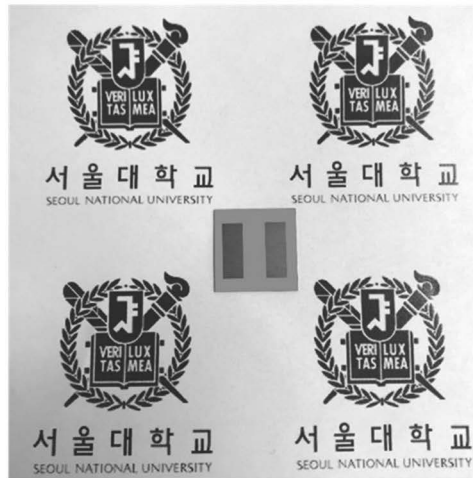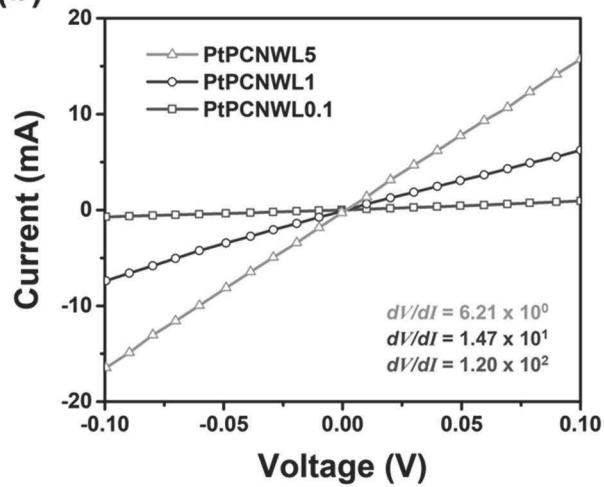
Figure 48. (a) Digital image of the PtPCNWL-based gas sensor electrode. (b) *I–V* curves of each conditions of PtPCNWLs at the voltage range from –0.1 V to 0.1 V.

3.3.4. Real-time sensing performance of PtPCNWL-based hydrogen gas sensor

The sensing mechanism of PtPCNWL-based H_2 gas sensor is schematically illustrated in **Figure 49**. The basical principle of hydrogen gas sensing is a catalytic reaction between H_2 molecules and Pt villus structure. When the active material of the gas sensor, PtPCNWL, is exposed to hydrogen gas, the H_2 molecules are adsorbed onto the PCNWL surface. Then, after the exposure of hydrogen gas stopped, the H_2 molecule is dissociated to two H atoms through the catalytic property of the platinum. The separated H atoms react with the Pt atoms forming the hybrid complex of PtH_x. Simultaneously, after the hydrogen gas chemisorbed, the generated electrons transfer to carbon layer, causing decreasing the number of holes in carbon layer. During the phase transition of platinum villus structure from Pt to PtH_x, the resistance of the sensor electrode increase. Then, PtHx is transformed to the original Pt structure by exposure to atmosphere, reacting with O_2 to generate H_2O. For this reason, as the active sites of Pt villus structure increase, the sensitivity of the PtPCNWL-based hydrogen gas sensor increase [97,103].

Real-time sensing of PtPCNWL-based gas sensor device progressed

with different concentration of hydrogen gas at ambient condition, as proved in **Figure 50a**. The range of hydrogen gas was differed from 10 to 200 ppm, which is lower than the guidelines of US Department of Energy for the flammable limit at 4% in air. Being exposed to the hydrogen gas, the PtPCNWL-based sensor electrode executed an increase of resistance. Meanwhile, as the electrode was blocked off from the hydrogen gas, the resistance of electrodes tended to return to its previous state before exposure. Unusually, the PtPCNWL-based hydrogen gas sensor exhibited lasting response after being exposed to the H_2 gas, no saturation point, and recovered partially, not to the incipient state. Because of the hydrogen sensing mechanism is basically catalytic reaction, assuming that there is sufficient Pt, the reaction is endless as long as there is a constant supply of hydrogen. In addition, to balance air pressure during gas sensing, inert gas (N_2 gas in here) was used when the electrode was shut off from the hydrogen and throughout the recovery time. At the time, the sensor electrode was difficult to contact oxygen to recover to original Pt structure, therefore the recovery in the sensing performance demonstrated insignificantly.

Figure 50b manifests the changes of the normalized resistance change, sensitivity, with the varying hydrogen gas concentration for different

condition of PtPCNWL-based sensor electrode. The sensitivity value was estimated a point of the normalized resistance after being exposed hydrogen gas during 200 s. The PtPCNWL-based sensor device exhibited the linear behavior over a wide range of hydrogen gas concentration in log scale, indicating the reversible and reproducible properties. The sensitivity of PtPCNWL-based hydrogen gas sensor depended on both conductivity and specific surface area. The sensor electrode with PtPCNWL1 and PtPCNWL5 indicated 10 times more sensitive detection toward H_2 gas than PtPCNWL0.1 because of their amount of deposited Pt villus structure and conductivity. Furthermore, the PtPCNWL1 and PtPCNWL5 demonstrated almost similar sensing performance, which the minimum detection level (MDL) toward H_2 gas is 10 ppm, each. Although the conductivity of PtPCNWL5 was substantiated 4 times higher than that of PtPCNWL1, the sensitivity disparity was showed only 1.4 times higher, because of their surface morphology difference, which is directly connected to specific surface area.

For application to sensor electrode materials, superior cycle stability as well as reversible and reproducible ability is required. The resistance changes for different condition of PtPCNWLs against periodic exposure

to 200 ppm of H_2 gas were proved in **Figure 51a**. The sensitivity of all condition for sensor electrodes was upheld for similar value with progressing 4 times repetitively at the ambient condition. Moreover, PtPCNWL-based hydrogen gas sensor electrode preserved their sensing ability toward 200 ppm of H_2 gas during a month (>95%), as noticed in **Figure 51b**. The PtPCNWLs were structurally stable during adsorption and desorption of H_2 gas, demonstrating superb stability for repetitive sensing in the PtPCNWL-based H_2 gas sensor devices.
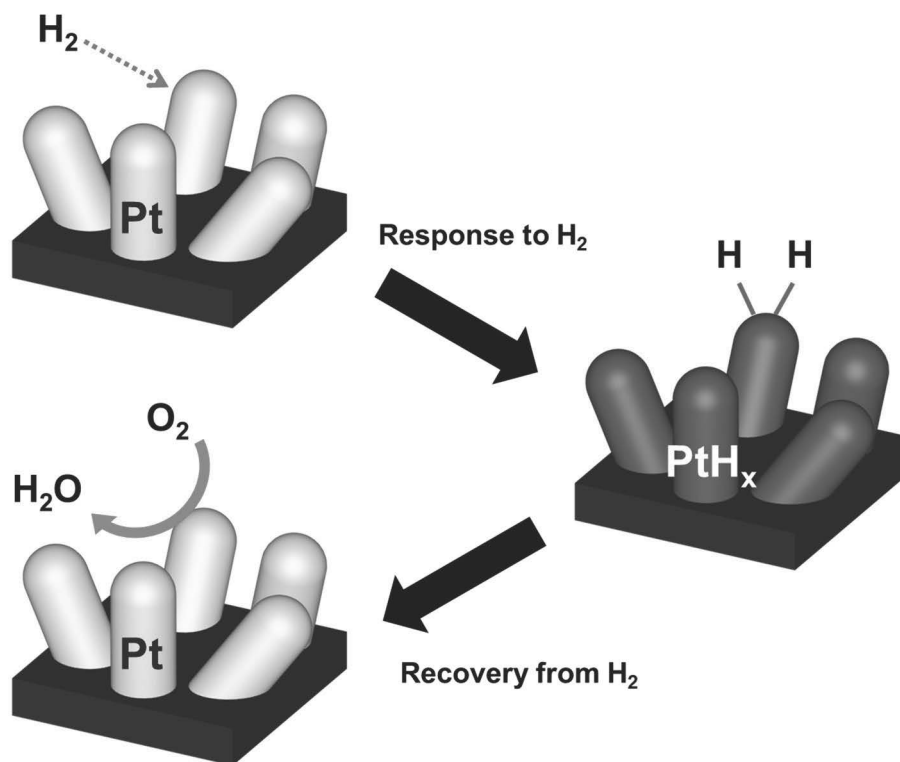
Figure 49. Schematic representation of sensing mechanism of PtPCNWL-based hydrogen gas sensor.
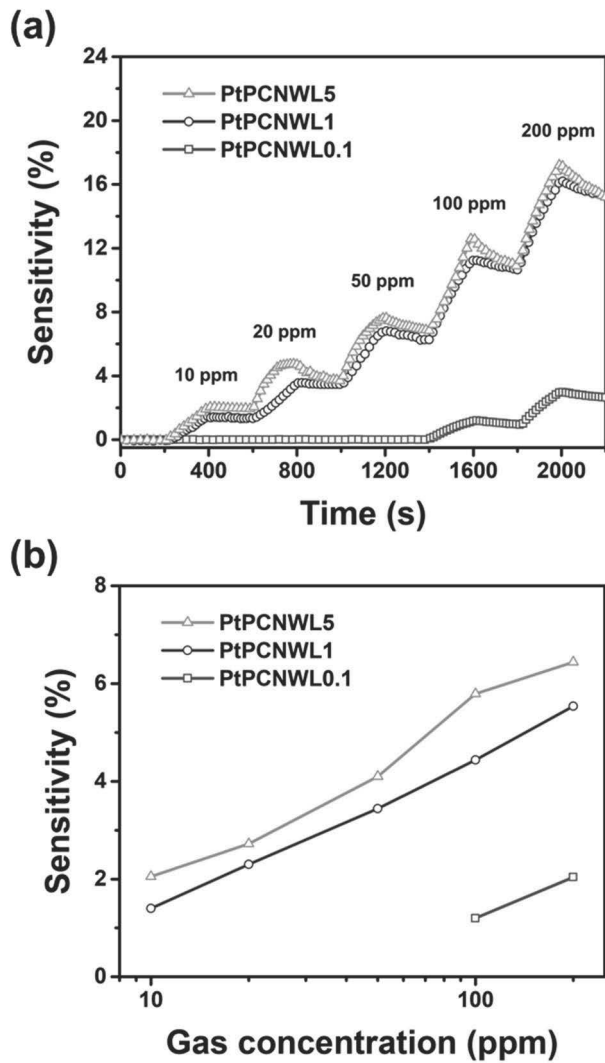
Figure 50. (a) Normalized resistance changes of hydrogen gas sensors based on PtPCNWLs (PtPCNWL0.1, PtPCNWL1, and PtPCNWL5) with sequential exposure to various concentrations of hydrogen gas. (b) Calibration curves as function of H_2 gas concentrations.
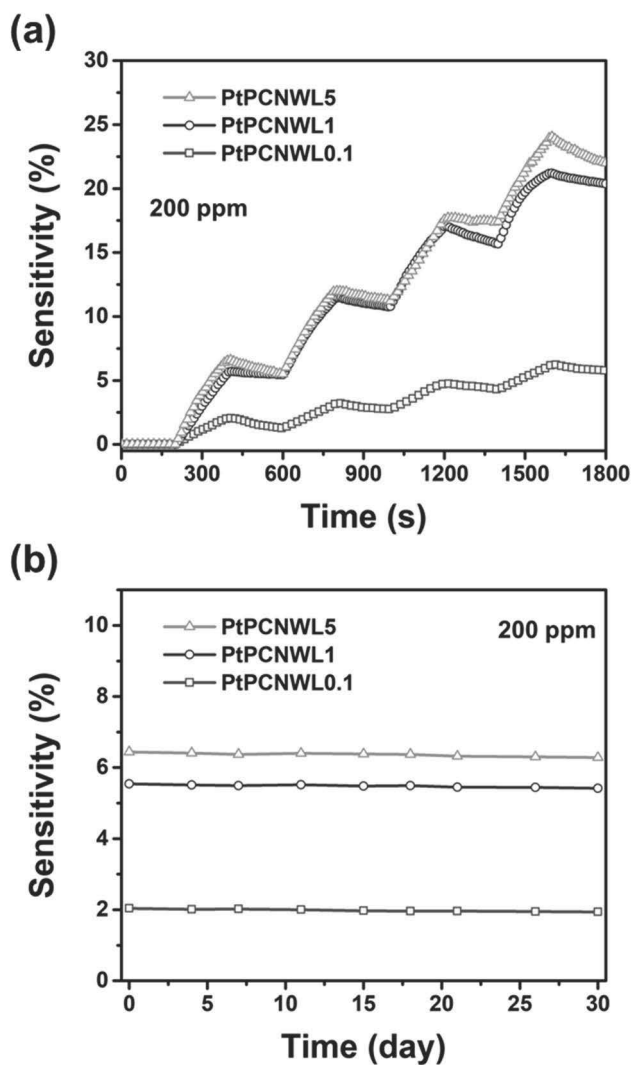
Figure 51. (a) Normalized resistance changes of H_2 gas sensors based on PtPCNWLs (PtPCNWL0.1, PtPCNWL1, and PtPCNWL5) with 4 repeated exposure toward 200 ppm of H_2 gas. (b) Cycle stability test of PtPCNWL-based gas sensors with periodic exposure to 200 ppm of hydrogen gas for a month.

126

4. Conclusion

Ultimately, morphological and chemical modified PCNWLs with shape morphology control, fluorination, and platinum villus structure deposition were fabricated and successfully applied to gas sensor devices. PCNWLs were fabricated for improving specific surface area and used as sensor transducer into the PCNWLs-based gas sensor electrodes. The PCNWLs-based gas sensor devices were measured superb real-time sensing performance toward ethanol gas. Furthermore, the PCNWLs were modified by fluorination (FPCNWLs) and platinum villus structure deposition (PtPCNWLs) using vacuum plasma treatment and electrochemical deposition method to enhance the sensing abilities toward ammonia and hydrogen gas, respectively. The FPCNWLs and PtPCNWLs-based gas sensor devices were also estimated outstanding real-time sensing performance toward NH_3 and H_2 gas. The subtopics are concluded in the viewpoint of each subtopic as follows:

1. PCNWLs were facilely fabricated with spin coating of different polymer mixing ratio and stepwise thermal treatments for improved specific surface area. The different surface tension, polarity, and molecular weight of PAN and PS caused immiscible solution, therefore,

the macro and mesopores on the carbon structure were constructed during the sequential heat treatment. The shape morphology and porosity of PCNWLs, representing specific surface area, were easily controlled by varying the polymer mixing ratio. PCNWL11 exhibited the largest specific surface area of 1256.8 $m^2 g^{-1}$. Furthermore, the PCNWLs-based ethanol gas sensor electrodes demonstrated superb ethanol sensing performances by the different specific surface areas and conductivities because of ethanol sensing mechanism as gas adsorption. MDL of PCNWLs-based ethanol gas sensor was 20 ppb using PCNWL11 and displayed linear range from 20 ppb to 200 ppm. In principle, the increament of specific surface area of PCNWLs leads to shorter response and recovery time due to their different gas adsorption abilities. Lastly, the PCNWL11-based ethanol gas sensor showed excellent reusability, cyclic stability, durability, and selectivity.

2. Fluorination progressed *via* vacuum plasma treatment to dope the fluorine into the carbon lattice of PCNWL11. The fluorine doping ratio was easily controlled with varying plasma handling time. The fluorination caused both increasing charge carriers by *p*-type doping and breaking the C=C bondings, therefore, the conductivity decreased with

the plasma treating time increased. On the other hand, fluorination was of help to affinity toward ammonia gas. The FPCNWLs-based ammonia gas sensor devices demonstrated outstanding NH_3 gas sensing performances by the different fluorination and conductivities because of ammonia gas sensing mechanism as gas adsorption. MDL of FPCNWLs-based ammonia gas sensor was 9 ppb using FPCNWL20 and displayed linear range from 9 ppb to 90 ppm. In principle, the close to equilibrium between the fluorination rate and C=C breaking ratio leads to shorter response and recovery time due to their different gas adsorption abilities. In closing, the FPCNWL20-based ammonia gas sensor demonstrated excellent cyclic stability, reusability, durability, and selectivity.

3. Platinum villus structure was introduced on the PCNWL11 by electrochemical deposition in acidic condition. The Pt structure grew from particle to villus shape with the deposition voltage increased negatively. Moreover, the size of Pt villus pieces increased, by extension, overgrown as the concentration of Pt precursor increased from 0.1 to 5 mM.

The PtPCNWLs-based hydrogen gas sensor electrodes demonstrated excellent H_2 gas sensing performances by the different amount of

deposited Pt and conductivities because of catalytic hydrogen gas sensing mechanism. MDL of PtPCNWLs-based hydrogen gas sensor was 10 ppm using PtPCNWL5 and exhibited linear range from 10 to 200 ppm. Although the amount of deposited Pt and the conductivity are lower, the PtPCNWL1-based H_2 gas sensor showed similar sensitivity with PtPCNWL5 due to the disparity of specific surface area by uniformly grown villus structure. At the end, the PtPCNWLs-based hydrogen gas sensor demonstrated excellent cyclic stability, reusability, and durability.

References

[1] R. Rauti, M. Musto, S. Bosi, M. Prato, L. Ballerini, *Carbon* **2019**, *143*, 430–446.

[2] C. Tan, X. Cao, X. J. Wu, Q. He, J. Yang, X. Zhang, J. Chen, W. Zhao, S. Han, G. H. Nam, M. Sindoro, H. Zhang, *Chem. Rev.* **2017**, *117*, 6225–6331.

[3] M. Xu, T. Liang, M. Shi, H. Chen, *Chem. Rev.* **2013**, *113*, 3766–3798.

[4] P. Chen, Y. Xu, S. He, X. Sun, S. Pan, J. Deng, D. Chen, H. Peng, *Nat. Nanotechnol.* **2015**, *10*, 1077–1083.

[5] J. Deng, M. Li, Y. Wang, *Green Chem.* **2016**, *18*, 4824–4854.

[6] Q. Luo, H. Ma, Q. Hou, Y. Li, J. Ren, X. Dai, Z. Yao, Y. Zhou, L. Xiang, H. Du, H. He, N. Wang, K. Jiang, H. Lin, H. Zhang, Z. Guo, *Adv. Funct. Mater.* **2018**, *28*.

[7] J. Ren, Y. Zhang, W. Bai, X. Chen, Z. Zhang, X. Fang, W. Weng, Y. Wang, H. Peng, *Angew. Chem. Int. Ed.* **2014**, *53*, 7864–7869.

[8] J. Shen, Y. Zhu, X. Yang, C. Li, *Chem. Commun.* **2012**, *48*, 3686–3699.

[9] Y. Wang, H. Xu, G. Drozdov, T. Dumitrică, *Carbon* **2018**, *139*, 94–104.

[10] Q. Fan, J. M. Gottfried, J. Zhu, *Acc. Chem. Res.* **2015**, *48*, 2484–2494.

[11] W. Gao, S. Emaminejad, H. Y. Y. Nyein, S. Challa, K. Chen, A. Peck, H. M. Fahad, H. Ota, H. Shiraki, D. Kiriya, D. H. Lien, G. A. Brooks, R. W. Davis, A. Javey, *Nature* **2016**, *529*, 509–514.

[12] C. Lee, X. Wei, J. W. Kysar, J. Hone, *Science* **2008**, *321*, 385–388.

[13] S. Lee, A. Reuveny, J. Reeder, S. Lee, H. Jin, Q. Liu, T. Yokota, T. Sekitani, T. Isoyama, Y. Abe, Z. Suo, T. Someya, *Nat. Nanotechnol.* **2016**, *11*, 472–478.

[14] Y. Liu, X. Dong, P. Chen, *Chem. Soc. Rev.* **2012**, *41*, 2283–2307.

[15] D. Pech, M. Brunet, H. Durou, P. Huang, V. Mochalin, Y. Gogotsi, P. L. Taberna, P. Simon, *Nat. Nanotechnol.* **2010**, *5*, 651–654.

[16] T. Q. Trung, N. E. Lee, *Adv. Mater.* **2016**, *28*, 4338–4372.

[17] W. Yang, K. R. Ratinac, S. P. Ringer, P. Thordarson, J. J. Gooding, F. Braet, *Angew. Chem. Int. Ed.* **2010**, *49*, 2114–2138.

[18] Z. Yang, J. Ren, Z. Zhang, X. Chen, G. Guan, L. Qiu, Y. Zhang, H. Peng, *Chem. Rev.* **2015**, *115*, 5159–5223.

[19] D. Yu, K. Goh, H. Wang, L. Wei, W. Jiang, Q. Zhang, L. Dai, Y. Chen, *Nat. Nanotechnol.* **2014**, *9*, 555–562.

[20] R. Paul, F. Du, L. Dai, Y. Ding, Z. L. Wang, F. Wei, A. Roy, *Adv. Mater.* **2019**, *31*, 1805598.

[21] H. Chen, S. You, Y. Ma, C. Zhang, B. Jing, Z. Cai, B. Tang, N. Ren, J. Zou, *Chem. Mater.* **2018**, *30*, 6014–6025.

[22] S. Wuttke, D. D. Medina, J. M. Rotter, S. Begum, T. Stassin, R.

Ameloot, M. Oschatz, M. Tsotsalas, *Adv. Funct. Mater.* **2018**, *28*, 1801545.

[23]   P. Xue, C. Chen, D. Diao, *Carbon* **2019**, *147*, 227-235.

[24]   P. Yi, D. Zhang, L. Peng, X. Lai, *ACS Appl. Mater. Interfaces* **2018**, *10*, 34561–34572.

[25]   C.-H. Jung, W.-J. Kim, C.-H. Jung, I.-T. Hwang, D. Khim, D.-Y. Kim, J.-S. Lee, B.-C. Ku, J.-H. Choi, *Carbon* **2015**, *87*, 257–268.

[26]   Z. Zhou, G. Liu, *Small* **2017**, *13*, 1603107.

[27]   K. Xie, Q. Fu, G. G. Qiao, P. A. Webley, *J. Membr. Sci.* **2019**, *572*, 38–60.

[28]   M. V. Kelso, N. K. Mahenderkar, Q. Chen, J. Z. Tubbesing, J. A. Switzer, *Science*, **2019**, *364*, 166–169.

[29]   M. D. Tyona, *Adv. Mater. Res.*, **2013**, *2*, 195–208.

[30]   J. Y. Na, B. Kang, D. H. Sin, K. Cho, Y. D. Park, *Sci. Rep.*, **2015**, *5*, 13288.

[31]   T.-H. Ko, C.-C. Yang, W.-T. Chang, *Carbon* **1993**, *31*, 583–590.

[32]   M. Kopeć, M. Lamson, R. Yuan, C. Tang, M. Kruk, M. Zhong, K. Matyjaszewski, T. Kowalewski, *Prog. Polym. Sci.* **2019**, *92*, 89–134.

[33]   Y. Peng, R. Burtovyy, Y. Yang, M. W. Urban, M. S. Kennedy, K. G. Kornev, R. Bordia, I. Luzinov, *Carbon* **2016**, *96*, 184–195.

[34]   Y. Zhang, N. Tajaddod, K. Song, M. L. Minus, *Carbon* **2015**, *91*, 479–493.

[35]   E. Cipriani, M. Zanetti, P. Bracco, V. Brunella, M. P. Luda, L. Costa, *Polym. Degrad. Stab.* **2016**, *123*, 178–188.

[36]   M. Darányi, I. Sarusi, A. Sápi, Á. Kukovecz, Z. Kónya, A. Erdőhelyi, *Thin Solid Films* **2011**, *520*, 57–63.

[37]   T.-H. Le, H. Yoon, *Carbon* **2019**, *152*, 796–817.

[38]   J. Luo, H. Chang, P.-H. Wang, R. J. Moon, S. Kumar, *Carbon* **2018**, *134*, 92–102.

[39]   J. Ryu, W. Kim, J. Yun, K. Lee, J. Lee, H. Yu, J. H. Kim, J. J. Kim, J. Jang, *ACS Appl. Mater. Interfaces* **2018**, *10*, 11843–11851.

[40]   N. Yousefi, X. Lu, M. Elimelech, N. Tufenkji, *Nat. Nanotechnol.* **2019**, *14*, 107–119.

[41]   L. Espinal, *Charact. Mater.* **2012**, 1–4.

[42]   P. Leclaire, O. Umnova, K. V. Horoshenkov, L. Maillet, *Rev. Sci. Instrum.* **2003**, *74*, 1366–1370.

[43]   J. A. Slotwinski, E. J. Garboczi, K. M. Hebenstreit, *J. Res. Natl. Inst. Stand. Technol.* **2014**, *119*, 494–528.

[44]   M. Ternan, *Can. J. Chem. Eng.* **1979**, *57*, 750–757.

[45]   H. Jin, X. Liu, S. Chen, A. Vasileff, L. Li, Y. Jiao, L. Song, Y. Zheng, S.-Z. Qiao, *ACS Energy Lett.* **2019**, *4*, 805–810.

[46]   J. Ortiz-Medina, Z. Wang, R. Cruz-Silva, A. Morelos-Gomez, F. Wang, X. Yao, M. Terrones, M. Endo, *Adv. Mater.* **2019**, *31*, 1805717.

[47]   X. Wang, G. Sun, P. Routh, D. H. Kim, W. Huang, P. Chen, *Chem.*

Soc. Rev. **2014**, *43*, 7067–7098.

[48]   X. Chen, X.-R. Chen, T.-Z. Hou, B.-Q. Li, X.-B. Cheng, R. Zhang, Q. Zhang, *Sci. Adv.* **2019**, *5*, eaau7728.

[49]   K. Gao, B. Wang, L. Tao, B. V. Cunning, Z. Zhang, S. Wang, R. S. Ruoff, L. Qu, *Adv Mater* **2019**, *31*, 1805121.

[50]   C. Hu, D. Liu, Y. Xiao, L. Dai, *Prog. Mat. Sci.-Mater.* **2018**, *28*, 121–132.

[51]   X. Wang, A. Vasileff, Y. Jiao, Y. Zheng, S. Z. Qiao, *Adv. Mater.* **2019**, *31*, 1803625.

[52]   K. C. Wasalathilake, G. A. Ayoko, C. Yan, *Carbon* **2018**, *140*, 276–285.

[53]   Y. I. Jhon, Y. Kim, J. Park, J. H. Kim, T. Lee, M. Seo, Y. M. Jhon, *Adv. Funct. Mater.* **2016**, *26*, 7551–7559.

[54]   C.-H. Lai, W.-S. Lai, H.-C. Chiue, H.-J. Chen, S.-Y. Chang, S.-J. Lin, *Thin Solid Films* **2006**, *510,* 125–133.

[55]   G. P. Papari, B. Silvestri, G. Vitiello, L. De Stefano, I. Rea, G. Luciani, A. Aronne, A. Andreone, *J. Phys. Chem. C* **2017**, *121*, 16012–16020.

[56]   J. G. Um, J. Jang, *Appl. Phys. Lett.* **2018**, *112*, 162104.

[57]   M. Chen, H. Zhou, C. Qiu, H. Yang, F. Yu, L. Sun, *Nanotechnology* **2012**, *23*, 115706.

[58]   G. Panomsuwan, N. Saito, T. Ishizaki, *J. Mater. Chem. A* **2015**, *3*, 9972–9981.

[59]   Y. Zhu, J. Xu, H. Jiang, D. Niu, X. Zhang, S. Hu, *Cryst. Eng. Comm.* **2018**, *20*, 6430–6437.

[60]   C. Lee, Y.-J. Han, Y. D. Seo, K. Nakabayashi, J. Miyawaki, R. Santamaría, R. Menéndez, S.-H. Yoon, J. Jang, *Carbon* **2016**, *103*, 28–35.

[61]   Y. Wang, Y. Chen, X. Song, Z. Zhang, J. She, S. Deng, N. Xu, J. Chen, *Physica E* **2018**, *99*, 254–260.

[62]   J. Wu, L. Xie, Y. Li, H. Wang, Y. Ouyang, J. Guo, H. Dai, *J. Am. Chem. Soc.* **2011**, *133*, 19668–19671.

[63]   H. Yu, H. I. Yeom, J. W. Lee, K. Lee, D. Hwang, J. Yun, J. Ryu, J. Lee, S. Bae, S. K. Kim, J. Jang, *Adv. Mater.* **2018**, *30*, 1704825.

[64]   C. G. Jin, Y. Yang, H. Y. Zhang, T. Y. Huang, M. Z. Wu, L. J. Zhuge, X. M. Wu, C. Ye, *J. Phys. D: Appl. Phys.* **2013**, *46*, 485206.

[65]   M. Hara, M. Lee, C.-H. Liu, B.-H. Chen, Y. Yamashita, M. Uchida, H. Uchida, M. Watanabe, *Electrochim. Acta* **2012**, *70*, 171–181.

[66]   Y. F. Huang, P. J. Kooyman, M. T. Koper, *Nat. Commun.* **2016**, *7*, 12440.

[67]   M. Iqbal, Y. V. Kaneti, J. Kim, B. Yuliarto, Y. M. Kang, Y. Bando, Y. Sugahara, Y. Yamauchi, *Small* **2019**, *15*, 1804378.

[68]   A. Ney, C. Pampuch, R. Koch, K. H. Ploog, *Nature* **2003**, *425*, 485–487.

[69] A. Tittl, P. Mai, R. Taubert, D. Dregely, N. Liu, H. Giessen, *Nano Lett.* **2011**, *11*, 4366–4369.

[70] J. S. Lee, O. S. Kwon, S. J. Park, E. Y. Park, S. A. You, H. Yoon, J. Jang, *ACS Nano* **2011**, *5*, 7992–8001.

[71] P. Li, Y. Yang, E. Shi, Q. Shen, Y. Shang, S. Wu, J. Wei, K. Wang, H. Zhu, Q. Yuan, A. Cao, D. Wu, *ACS Appl. Mater. Interfaces* **2014**, *6*, 5228–5234.

[72] G. A. Shaw, J. S. Trethewey, A. D. Johnson, W. J. Drugan, W. C. Crone, *Adv. Mater.* **2005**, *17*, 1123–1127.

[73] L. Wang, L. Chen, B. Yan, C. Wang, F. Zhu, X. Jiang, Y. Chao, G. Yang, *J. Mater. Chem. A* **2014**, *2*, 8334–8341.

[74] G. Yu, X. Xie, L. Pan, Z. Bao, Y. Cui, *Nano Energy* **2013**, *2*, 213–234.

[75] V. A. Zinovyeva, M. A. Vorotyntsev, I. Bezverkhyy, D. Chaumont, J.-C. Hierso, *Adv. Funct. Mater.* **2011**, *21*, 1064–1075.

[76] S. Porel, S. Singh, S. S. Harsha, D. N. Rao, T. P. Radhakrishnan, *Chem. Mater.* **2015**, *17*, 9–12.

[77] P. Prins, L. P. Candeias, A. J. J. M. van Breemen, J. Sweelssen, P. T. Herwig, H. F. M. Schoo, L. D. A. Siebbeles, *Adv. Mater.* **2005**, *17*, 718–723.

[78] I. M. Dharmadasa, J. Haigh, *J. Electrochem. Soc.* **2006**, *153*, G47–G52.

[79] G. Sabouraud, S. Sadki, N. Brodie, *Chem. Soc. Rev.* **2000**, *29*,

283–293.

[80]   B. M. Mundotiya, W. Ullah, in *Novel Metal Electrodeposition and the Recent Application* (Eds.: M. Sone, K. Masu), IntechOpen, **2019**.

[81]   L. Santos, J. P. Neto, A. Crespo, P. Baião, P. Barquinha, L. Pereira, R. Martins, E. Fortunato, in *Electroplating of Nanostructures* (Ed.: M. Aliofkhazraei), IntechOpen, **2015**.

[82]   I. Zhitomirsky, *Adv. Colloid Interface Sci.* **2002**, *97*, 279–317.

[83]   D. Sobha Jayakrishnan, in *Corrosion Protection and Control Using Nanomaterials*, Woodhead Publishing, **2012**, pp. 86–125.

[84]   C. Choi, M. K. Choi, S. Liu, M. S. Kim, O. K. Park, C. Im, J. Kim, X. Qin, G. J. Lee, K. W. Cho, M. Kim, E. Joh, J. Lee, D. Son, S. H. Kwon, N. L. Jeon, Y. M. Song, N. Lu, D. H. Kim, *Nat. Commun.* **2017**, *8*, 1664.

[85]   C. Choi, Y. Lee, K. W. Cho, J. H. Koo, D. H. Kim, *Acc. Chem. Res.* **2019**, *52*, 73–81.

[86]   S. Choi, S. I. Han, D. Jung, H. J. Hwang, C. Lim, S. Bae, O. K. Park, C. M. Tschabrunn, M. Lee, S. Y. Bae, J. W. Yu, J. H. Ryu, S. W. Lee, K. Park, P. M. Kang, W. B. Lee, R. Nezafat, T. Hyeon, D. H. Kim, *Nat. Nanotechnol.* **2018**, *13*, 1048–1056.

[87]   S. Choi, S. I. Han, D. Kim, T. Hyeon, D. H. Kim, *Chem. Soc. Rev.* **2019**, *48*, 1566–1595.

[88]   D. C. Kim, H. J. Shim, W. Lee, J. H. Koo, D. H. Kim, *Adv. Mater.*

2019, 1902743.

[89] O. S. Kwon, H. S. Song, T. H. Park, J. Jang, *Chem. Rev.* **2019**, *119*, 36–93.

[90] S. R. Ahn, J. H. An, I. H. Jang, W. Na, H. Yang, K. H. Cho, S. H. Lee, H. S. Song, J. Jang, T. H. Park, *Biosens. Bioelectron.* **2018**, *117*, 628–636.

[91] K. H. Cho, D. H. Shin, J. Oh, J. H. An, J. S. Lee, J. Jang, *ACS Appl. Mater. Interfaces* **2018**, *10*, 28412–28419.

[92] J. Jun, J. S. Lee, D. H. Shin, J. Oh, W. Kim, W. Na, J. Jang, *J. Mater. Chem. A* **2017**, *5*, 17335–17340.

[93] S. G. Kim, J. Jun, J. S. Lee, J. Jang, *J. Mater. Chem. A* **2019**, *7*, 8451–8459.

[94] W. Kim, J. S. Lee, D. H. Shin, J. Jang, *J. Mater. Chem. B* **2018**, *6*, 1272–1278.

[95] O. S. Kwon, S. H. Lee, S. J. Park, J. H. An, H. S. Song, T. Kim, J. H. Oh, J. Bae, H. Yoon, T. H. Park, J. Jang, *Adv. Mater.* **2013**, *25*, 4177–4185.

[96] O. S. Kwon, S. J. Park, J. S. Lee, E. Park, T. Kim, H. W. Park, S. A. You, H. Yoon, J. Jang, *Nano Lett.* **2012**, *12*, 2797–2802.

[97] J. S. Lee, J. Oh, J. Jun, J. Jang, *ACS Nano* **2015**, *9*, 7783–7790.

[98] W. Na, J. Lee, J. Jun, W. Kim, Y. K. Kim, J. Jang, *J. Ind. Eng. Chem.* **2019**, *69*, 358–363.

[99] W. Na, J. W. Park, J. H. An, J. Jang, *J. Mater. Chem. B* **2016**, *4*,

5025–5034.

[100] J. Oh, J. S. Lee, J. Jun, S. G. Kim, J. Jang, *ACS Appl. Mater. Interfaces* **2017**, *9*, 39526–39533.

[101] J. W. Park, W. Na, J. Jang, *RSC Adv.* **2016**, *6*, 14335–14343.

[102] S. J. Park, O. S. Kwon, S. H. Lee, H. S. Song, T. H. Park, J. Jang, *Nano Lett.* **2012**, *12*, 5082–5090.

[103] D. H. Shin, J. S. Lee, J. Jun, J. H. An, S. G. Kim, K. H. Cho, J. Jang, *Sci. Rep.* **2015**, *5*, 12294.

[104] S. Y. Cho, H. Yu, J. Choi, H. Kang, S. Park, J. S. Jang, H. J. Hong, I. D. Kim, S. K. Lee, H. S. Jeong, H. T. Jung, *ACS Nano* **2019**, *13*, 9332–9341.

[105] S. J. Choi, H. Yu, J. S. Jang, M. H. Kim, S. J. Kim, H. S. Jeong, I. D. Kim, *Small* **2018**, *14*, 1703934.

[106] D. H. Kim, J. S. Jang, W. T. Koo, S. J. Choi, H. J. Cho, M. H. Kim, S. J. Kim, I. D. Kim, *ACS Sens.* **2018**, *3*, 1164–1173.

[107] R. Kim, J. S. Jang, D. H. Kim, J. Y. Kang, H. J. Cho, Y. J. Jeong, I. D. Kim, *Adv. Funct. Mater.* **2019**, *29*, 1903128.

[108] W.-T. Koo, J.-H. Cha, J.-W. Jung, S.-J. Choi, J.-S. Jang, D.-H. Kim, I.-D. Kim, *Adv. Funct. Mater.* **2018**, *28*, 1802575.

[109] A. A. Abokifa, K. Haddad, J. Fortner, C. S. Lo, P. Biswas, *J. Mater. Chem. A* **2018**, *6*, 2053–2066.

[110] A. K. Elger, J. Baranyai, K. Hofmann, C. Hess, *ACS Sens.* **2019**, *4*, 1497–1501.

[111] A. Henning, N. Swaminathan, Y. Vaknin, T. Jurca, K. Shimanovich, G. Shalev, Y. Rosenwaks, *ACS Sens.* **2018**, *3*, 128–134.

[112] R. Malik, V. K. Tomer, T. Dankwort, Y. K. Mishra, L. Kienle, *J. Mater. Chem. A* **2018**, *6*, 10718–10730.

[113] H. Y. Li, C. S. Lee, D. H. Kim, J. H. Lee, *ACS Appl. Mater. Interfaces* **2018**, *10*, 27858–27867.

[114] S. Sasmal, A. Sinha, B. Donnadieu, R. G. S. Pala, S. Sivakumar, S. Valiyaveettil, *ACS Appl. Mater. Interfaces* **2018**, *10*, 6711–6718.

[115] A. S. Sizov, A. A. Trul, V. Chekusova, O. V. Borshchev, A. A. Vasiliev, E. V. Agina, S. A. Ponomarenko, *ACS Appl. Mater. Interfaces* **2018**, *10*, 43831–43841.

[116] D. Maity, R. T. R. Kumar, *ACS Sens.* **2018**, *3*, 1822–1830.

[117] S. Nufer, M. J. Large, A. A. K. King, S. P. Ogilvie, A. Brunton, A. B. Dalton, *ACS Appl. Mater. Interfaces* **2018**, *10*, 21740–21745.

[118] L. A. Panes-Ruiz, M. Shaygan, Y. Fu, Y. Liu, V. Khavrus, S. Oswald, T. Gemming, L. Baraban, V. Bezugly, G. Cuniberti, *ACS Sens.* **2018**, *3*, 79–86.

[119] R. Ab Kadir, W. Zhang, Y. Wang, J. Z. Ou, W. Wlodarski, A. P. O'Mullane, G. Bryant, M. Taylor, K. Kalantar-zadeh, *J. Mater. Chem. A* **2015**, *3*, 7994–8001.

[120] S. Amrehn, X. Wu, T. Wagner, *ACS Sens.* **2018**, *3*, 191–199.

[121] A. Katoch, J. H. Kim, Y. J. Kwon, H. W. Kim, S. S. Kim, *ACS Appl. Mater. Interfaces* **2015**, *7*, 11351–11358.

[122] A. Lee, J. Park, K. S. Choi, J. Lee, I. Yoo, I. S. Cho, B. Ahn, H. Seo, J.-Y. Choi, H. K. Yu, *Carbon* **2017**, *125*, 221–226.

[123] I. Oueslati, A. Ghrairi, E. S. Ribeiro, L. A. E. Batista de Carvalho, J. M. Gil, J. A. Paixao, *J. Mater. Chem. A* **2018**, *6*, 10649–10654.

[124] J. D. Fowler, S. Virji, R. B. Kaner, B. H. Weiller, *J. Phy. Chem. C* **2009**, *113*, 6444–6449.

[125] D. Jung, M. Han, G. S. Lee, *ACS Appl. Mater. Interfaces* **2015**, *7*, 3050–3057.

[126] D. H. Kim, S. J. Kim, H. Shin, W. T. Koo, J. S. Jang, J. Y. Kang, Y. J. Jeong, I. D. Kim, *ACS Nano* **2019**, *13*, 6071–6082.

[127] R. M. Penner, *Acc. Chem. Res.* **2017**, *50*, 1902–1910.

[128] J. Wang, S. Rathi, B. Singh, I. Lee, H. I. Joh, G. H. Kim, *ACS Appl. Mater. Interfaces* **2015**, *7*, 13768–13775.

[129] A. U. Itodo, H. U. Itodo, M. K. Gafar, *J. Appl. Sci. Environ. Manage.* **2010**, *14*, 141–145.

[130] C. Kaewprasit, E. Hequet, N. Abidi, J. P. Gourlot, *J. Cotton Sci.* **1998**, *2*, 164–173.

[131] J. O. Amode, J. H. Santos, Z. Md. Alam, A. H. Mirza, C. C. Mei, *Int. J. Ind. Chem.* **2016**, *7*, 333–345.

[132] Y. Li, Q. Du, T. Liu, X. Peng, J. Wang, J. Sun, Y. Wang, S. Wu,

Z. Wang, Y. Xia, L. Xia, *Chem. Eng. Res. Des.* **2013**, *91*, 361–368.

[133]   H. Yu, J. W. Lee, J. Yun, K. Lee, J. Ryu, J. Lee, D. Hwang, S. K. Kim, J. Jang, *Adv. Energy Mater.* **2017**, *7*, 1700749.

[134]   J. Cenens, R. A. Schoonheydt, *Clay. Clay Miner.* **1988**, *36*, 214–224.

[135]   F. A. Ozdemir, B. Demirata, R. Apak, *J. Appl. Polym. Sci.* **2009**, *112*, 3442–3448.

[136]   E. Fitzer, W. Frohs, M. Heine, *Carbon* **1986**, *24*, 387–395.

[137]   M. Eslamian, *Nanomicro Lett.* **2017**, *9*, 3.

[138]   D. B. Hall, P. Underhill, J. M. Torkelson, *Polym. Eng. Sci.* **1998**, *38*, 2039–2045.

[139]   K. Xie, Q. Fu, G. G. Qiao, P. A. Webley, *J. Membrane Sci.* **2019**, *572*, 38–60.

[140]   Z. Li, J. T. Zhang, Y. M. Chen, J. Li, X. W. Lou, *Nat. Commun.* **2015**, *6*, 8850.

[141]   P. Ramakrishnan, S. Shanmugam, *ACS Sustain. Chem. Eng.* **2016**, *4*, 2439–2448.

[142]   H. Zhang, W. Zhou, T. Chen, B. Y. Guan, Z. Li, X. W. Lou, *Energy Environ. Sci.* **2018**, *11*, 1980–1984.

[143]   J. Zhang, Z. Li, X. W. D. Lou, *Angew. Chem. Int. Ed.* **2017**, *56*, 14107–14112.

[144]   I. V. Anoshkin, A. G. Nasibulin, P. R. Mudimela, M. He, V.

Ermolov, E. I. Kauppinen, *Nano Res.* **2012**, *6*, 77–86.

[145]   I. T. Martin, E. R. Fisher, *J. Vac. Sci. Technol. A* **2004**, *22*, 2168–2176.

[146]   M. Álvarez-Paino, A. Muñoz-Bonilla, G. Marcelo, J. Rodríguez-Hernández, M. F.-García, *Polym. Chem.* **2012**, *3*, 3282–3288.

[147]   B. Zhang, G. Zhang, Q. Wang, C. Li, J. He, Z. An, *AIP Adv.* **2015**, *5*, 127207.

[148]   W. Na, J. Jun, J. W. Park, G. Lee, J. Jang, *J. Mater. Chem. A* **2017**, *5*, 17379–17387.

[149]   H. Zhang, L. Fan, H. Dong, P. Zhang, K. Nie, J. Zhong, Y. Li, J. Guo, X. Sun, *ACS Appl. Mater. Interfaces* **2016**, *8*, 8652–8661.

[150]   V. Agarwal, I. Aruna, V. Banerjee, B. R. Mehta, *Phys. Rev. B* **2006**, *74*, 035412.

[151]   M. E. Hyde, R. G. Compton, *J. Electroanal. Chem.* **2003**, *549*, 1–12.

[152]   R. M. Penner, *J. Phys. Chem. B* **2002**, *106*, 3339–3353.

[153]   J. Ustarroz, X. Ke, A. Hubin, S. Bals, H. Terryn, *J. Phys. Chem. C* **2012**, *116*, 2322–2329.

[154]   M. A. Matin, E. Lee, H. Kim, W.-S. Yoon, Y.-U. Kwon, *J. Mater. Chem. A* **2015**, *3*, 17154–17164.

[155]   Q. Shi, C. Zhu, M. H. Engelhard, D. Du, Y. Lin, *RSC Adv.* **2017**, *7*, 6303–6308.

[156]   B. P. Vinayan, S. Ramaprabhu, *Nanoscale* **2013**, *5*, 5109–5118.

국문 초록

센서는 사물 인터넷 시대를 맞이하여 인간의 실생활과 밀접하게 관련되어 있기 때문에 매우 중요시 되고 있다. 그중에서도, 고성능의 가스센서는 의료 진단, 헬스 케어 시스템, 환경 감시, 식료품 품질 관리, 그리고 가연성, 폭발성, 유해성, 독성 가스들에 대한 산업 안전을 위해 요구된다. 가스 센서의 성능은 트랜스듀서의 감지 능력에 달려있다. 트랜스듀서는 타겟 물질을 감지하고 감지 결과를 전기 신호로 변환하는 센서 장치의 구성 요소 중 하나이다. 트랜스듀서의 센싱 능력을 개선하기 위해 비표면적 증대를 위한 나노 재료가 활발히 연구되고 있다. 나노 재료들 중에서도 특히 폴리아크릴로니트릴 기반의 탄소 나노 재료는 생체 적합성, 취급 용이성, 환경 안정성 및 높은 전기 전도성 때문에 일반적으로 그리고 널리 연구되고 있다. 비록 탄소 나노 재료의 소형화가 비표면적을 증가시키는 대표적인 방법이지만, 표면 개질 또한 활물질의 감지 능력을 향상시키는 효율적인 방법 중 하나이다.

본 박사학위 논문은 폴리아크릴로니트릴을 기반으로 하는 탄소 나노그물막 표면 형태와 화학 특성을 효과적으로 개질하

고 이를 가스 감지를 위한 센서 트랜스듀서에 응용하는 방법을 제시한다. 먼저, 폴리스티렌과 폴리아크릴로니트릴의 혼합비를 조절하고 순차적인 열처리를 거쳐 다공성 탄소 나노그물막의 표면 형태 조절을 진행 하였다. 다공성 탄소 나노그물막은 순수 폴리아크릴로니트릴 기반 탄소 층과 비교하여 높은 비표면적을 나타내어 에탄올 검출을 위한 고감도 가스 센서를 구성한다. 둘째로는, 플라즈마 처리 시간을 다르게 하여 진공 플라즈마 처리를 통해 다공성 탄소 나노그물막에 플루오린 원자를 도핑하였고 이를 암모니아 가스 센서에 적용 하였다. 마지막으로, 백금 전구체의 농도와 전압을 조절하여 다공성 탄소 나노그물막 위에 백금 융모 구조를 전기 화학적으로 증착하여 귀금속 도입을 진행하였다. 백금 융모 구조가 도입된 다공성 탄소 나노 나노그물막은 매우 뛰어난 수소 가스 센서 성능을 보여주었다.

정리하면, 본 박사학위 논문은 비표면적을 증가시키고, 화학적, 기계적 및 전기적 특성을 향상시키고, 가스 감지 능력 향상을 위해 폴리아크릴로니트릴을 기반으로 하는 다공성 탄소 나노그물막의 용이한 형태적 및 화학적 개질 방법을 제시한다. 또한, 제시된 다공성 탄소 나노그물막, 플루오르가 도핑된 다공성 탄소 나노그물막 및 백금 융모 구조가 도입된 다공성 탄

146

소 나노그물막을 센서 트랜스듀서로 이용한 고감도 가스 센서 응용에 대한 접근법을 제시한다. 더 나아가 본 학위논문은 트랜스듀서의 활물질을 개질하고 가스 센서 시스템을 구성하는 혁신적인 방법론적 통찰을 제안한다.

주요어: 형태적 개질; 화학적 개질; 표면 형태 조절; 이종원소 도핑; 플루오린 도핑; 금속 도입; 귀금속; 백금; 전기화학적 도금; 탄소 나노그물막; 가스 센서; 에탄올; 암모니아; 수소

학 번: 2015-21017

감사의 글

먼저, 제 삶의 주인 되시는 하나님께 모든 영광을 드립니다. 이 모든 것이 다 주님이 하셨습니다. 감사합니다. 기대 반 걱정 반의 마음가짐으로 신촌을 떠나 관악에 처음 발을 디뎠을 때가 엊그제 같은데, 어느덧 짧다면 짧고 길다면 길다고 할 수 있는 5년의 시간이 흘렀습니다. 학위 기간을 되돌아보니 여러 우여곡절도 있었지만, 그래도 서울대학교 고분자 재료 연구실에서의 대학원 생활은 정말 값졌다고 생각합니다. 저의 20대 후반과 30대 초반을 온전히 보낸 박사과정 동안 저는 부족함과 한계를 느끼기도 했지만, 한편으로는 그 시간이 저에겐 다방면으로 배움과 성장의 시간이기도 하였습니다. 학위 기간 동안 지도교수님을 포함하여 제 주위의 많은 분들의 응원과 도움 그리고 기도를 통해 제가 무사히 박사 학위를 받을 수 있었습니다. 이에 글로나마 짧게 감사의 인사를 전하려 합니다.

부족한 저를 이끌어 주시고 연구에 대한 열정으로 지도해주신 장정식 교수님께 진심으로 감사드립니다. 학문적으로 뿐만 아니라 인격적으로도 한 사람으로서 지녀야 할 성품과 태도를

일러주셨고, 올바른 연구자의 자세를 가르쳐 주셨습니다. 이러한 교수님의 가르침을 항상 기억하고 앞으로 사회에 나가서도 교수님과 고분자 재료 연구실의 명성에 누가 되지 않도록 열심히 정진하겠습니다. 또한 바쁘신 와중에도 저의 학위논문을 심사해 주시고 조언을 아끼지 않으셨던 조재영 교수님, 이종찬 교수님, 오준학 교수님, 그리고 KIST 임순호 박사님께 이 글을 빌어 깊은 감사를 드립니다.

연구실 생활 5년 간 함께 고생한 선·후배 동료들을 통하여 많은 것을 배웠고 또한 좋은 추억을 쌓은 것 같습니다. 그 중에서도 특별히 많은 도움을 주시고 재미있는 추억을 함께한 선배들 특히 사수인 진욱이형을 비롯하여 동훈이형, 재문이형, 재훈이형, 주영이형, 정섭이, 영덕이형, 해준이형, 경섭이, 정균이, 기수, 그리고 입학 동기였던 정철이에게 감사의 인사를 드립니다. 또한 졸업 동기인 우영이와 윤기, 그리고 예리에게도 고마운 마음을 전하며 우리들의 졸업 후의 발걸음이 한층 가볍길 바랍니다. 마지막으로, 성근이형과 중원이형에게도 고마운 마음과 함께 PML의 마지막을 부탁드립니다. 지면상 미처 언급하지 못한 여러 고분자 재료 연구실 선배님들에게도 감사의 인사를 드립니다. 함께 했던 모든 날들이 좋았습니다. 앞으로도 잘 부탁드립니다.

149

다음으로 연구적인 측면 이외에도 같이 추억을 만들기도 하고 저를 응원해준 주코 친구들과 광남중·고 친구들, 연이 동문회 동기들 및 선·후배분들, 연세대학교 동기들 및 선·후배님들, 동아리 몽상가들 친구들, 제가 활동했던 모든 학내·외 모임 친구들, 오륜교회 여러 목사님들과 청년부 사람들, 그 외에도 저와 인연이 닿아 연락하며 지내던 모든 분들에게도 감사의 말을 전하고 싶습니다.

마지막으로 기쁠 때나 슬플 때나 항상 함께했던 사랑하는 우리가족에게 무한한 감사의 마음을 전하고 싶습니다. 존재만으로도 든든함과 의지할 곳이 되어주신 아버지와 언제나 기도로 품어주시고 저에게 정신적인 위로가 되어주신 어머니, 언제나 변함없이 아무 조건 없는 크고 아름다운 사랑을 베풀어주셔서 감사합니다. 두 분의 갚을 길 없는 무한한 사랑으로 제가 여기까지 왔습니다. 앞으로 더욱 더 듬직하고 믿음직스러운 아들이 되도록 하겠습니다. 아버지, 어머니 사랑합니다. 그리고 묵묵히 자리를 지켜준 하나뿐인 대견한 동생 용주에게도 정말 고맙다는 말을 전하고 싶습니다. 앞으로도 우리가족이 화목하게 서로 의지하며 건강하게 지내길 기도합니다. 또한 항상 저를 응원해 마지않는 이모와, 저를 이렇게 키워주신 외할머니 그리고 할아버지, 할머니를 포함한 친지 가

족 모두에게도 감사의 인사를 드립니다. 항상 오래오래 건강하시길 기도합니다.

공학박사라는 학위를 받기까지 학부 포함 9년의 시간 동안 참 다양한 경험을 한 것 같습니다. 더불어 항상 자만하지 않고 겸손해야 하며, 배움에는 끝이 없다는 것을 알 수 있었습니다. 학교를 떠나 사회로 나가서도 그동안 받았던 고마움을 잊지 않고 겸손한 자세로 더욱더 지식과 능력을 갈고 닦아 성숙한 한 명의 박사 연구원으로서 부끄럽지 않도록 노력하겠습니다.

마지막으로 주변 모든 분들이 예수님의 평안 안에서 행복과 건강하기를 진심으로 기도하겠습니다. 감사합니다.

2019년 12월
관악을 내려가며
나원주 드림